THE IONIZATION DYNAMICS OF ATOMS AND MOLECULES EXPOSED TO SHORT PULSES

Stian Astad Sørngård

Dissertation for the degree of Philosophiae Doctor (PhD)

Department of Physics and Technology
University of Bergen

May 2013

Scientific environment

This thesis has been supervised by Professor Morten Førre, University of Bergen, and co-supervised by Professor Jan Petter Hansen, University of Bergen. The work is part of the project Super Intense Laser-Molecule Interactions (SILMI) led by Morten Førre in the research group of Optics and Atomic Physics at the Department of Physics and Technology. The project is founded by the Bergen Research Foundation (Bergens Forskningsstiftelse) and the Department of Physics and Technology, University of Bergen.

ACKNOWLEDGEMENTS

Let me start by expressing my gratitude to my supervisor over the past four years, Professor Morten Førre – a person who I really have enjoyed working with and whose commitment to the field I admire. My co-supervisor Professor Jan Petter Hansen also deserves thanks. His ideas and contributions have been most helpful.

Next in line are my dear friends and colleagues through many years:
Ingjald, thank you for your involvement and enthusiasm.
Sigurd, thank you for good discussions and bright ideas.
Sigrid, thank you for a collaboration I will not forget.

I am also grateful to the rest of my former and present colleagues in the group of Optics and Atomic Physics. Professor Ladislav Kocbach I would like to thank in particular for all our late afternoon discussions from which I have learned a lot, and Arne for all his pranks. I appreciate the work and effort of Raymond and Aleksander on our common publications. The same goes for Associate Professor Esa Räsänen, Tampere University, who made a significant contribution to one of the quantum dot publications. I would like to acknowledge the Bergen Research Foundation, the NordForsk network, Nordita, the grant EU PF7(IRSES) DWBQS, and the Department for Physics and Technology at UiB from which I have received financial support for research and travels. I would like to thank Professor Pablo Fainstein for facilitating a one month stay at Centro Atómico Bariloche, and Daniel, Juan, Jan Petter and Sigrid *et al.* for making it a memorable experience.

Finally, I would like to thank my parents, Åse and Egil, and my sister Maria for their invaluable support.

Stian

ABSTRACT

The electrons ejected in an ionization event initiated by an incident laser pulse carry detailed information about the structure and the correlation intrinsic to atoms and molecules. This information is essential for our fundamental understanding of such systems.

This thesis is a contribution to the study of the ionization dynamics of atoms and molecules exposed to short laser pulses within the field of atomic, molecular and optical sciences. It consists of five papers published in the period 2011-2013, and covers four topics: the ionization dynamics of Rydberg wave packets, high-order harmonic generation, atomic stabilization and two-photon double ionization of the hydrogen molecule.

Rydberg atoms are atoms where at least one of the electrons are found in a highly excited state. As the Rydberg electrons are weakly bound, they are easily affected by external electric and magnetic fields. They exhibit exceptionally long lifetimes and may under certain circumstances behave almost like classical particles. In this work we study the ionization dynamics of a Rydberg wave packet formed within a single Stark-split n-shell in hydrogen. The wave packet is resonantly driven between different substates in the shell governed by the action of a rotating microwave field. Superimposed on this process the wave packet is hit by a series of short femtosecond pulses. We study how the number of pulses in the pulse-train and the time-separation between them affect the total and the angular resolved ionization probability of the system.

Ionization is also essential in the generation of high-order harmonics. In this process the ionized electron is accelerated before it recombines with the atom, and photons of frequencies that are multiples of the laser frequency are emitted. The present thesis presents a study of high-order harmonics generated when a graphene sheet is exposed to few-cycle femtosecond pulses. Graphene is a single layer of graphite, and was experimentally realized for the first time less than a decade ago. Our study shows that the extended nature of graphene sheets allows for strong harmonic signals as well as maximum harmonics beyond what is observed for atoms and simpler molecules.

The third topic to be studied is atomic stabilization. In the limit where the laser intensity is so strong that the force between the nucleus and the electrons is negligible in comparison to the applied forces of the laser, calculations yield an interesting result. Instead of monotonically increasing as a function of the laser intensity, as expected, the ionization probability tends to stabilize below 100% or even start to decline. Although the phenomenon has been extensively studied for more than 20 years, the experimental verifications are scarce and disputed, mainly due to the lack of the laser technology required. Two of the papers included in this work present *ab initio* calculations on atomic stabilization solving the time-dependent Schrödinger equation from first principles. Firstly, the phenomenon is studied in helium subjected to superintense pulses.

In this paper we especially focus on the correlation between the two electrons, and investigate how it influences the stabilization effect. Secondly, we conduct a similar study but in a different atomic system: low-lying circular Rydberg states of hydrogen. In many respects a circular state behaves like a classical particle orbiting the nucleus either clockwise or counter-clockwise. Motivated by this fact, we study how the ionization probability is affected by a circularly polarized electric field which is either co- or counter-rotating with respect to the electronic motion.

Lastly, the numerical framework, used in the stabilization calculations, is extended to model the hydrogen molecule. We calculate the direct two-photon double ionization resulting from a linearly polarized laser pulse. Both parallel and perpendicular orientation of the laser polarization vector with respect to the internuclear axis is considered. This is a research domain where the results are few, and different approaches are argued for. Our results are shown to be in good agreement with previous studies, and show for the first time the generalized cross section for the two-photon double ionization process beyond 30 eV.

LIST OF PUBLICATIONS

This thesis is based on the following publications:

I S. A. Sørngård, S. Askeland, R. Nepstad and M. Førre, *Multiphoton ionization and stabilization of helium in superintense xuv fields*, Physical Review A **83**, 033414, 2011.

II S. Askeland, S. A. Sørngård, I. Pilskog, R. Nepstad and M. Førre, *Stabilization of circular Rydberg atoms by circularly polarized infrared laser fields*, Physical Review A **84**, 033423, 2011.

III A. S. Simonsen, S. A. Sørngård, R. Nepstad and M. Førre, *Direct two-photon double ionization of* H_2, Physical Review A **85**, 063404, 2012.

IV S. I. Simonsen, S. A. Sørngård, M. Førre and J. P. Hansen, *Femtosecond-pulse-train ionization of Rydberg wave packets*, Physical Review A **86**, 043423, 2012.

V S. A. Sørngård, S. I. Simonsen and J. P. Hansen, *High-order harmonic generation from graphene: Strong attosecond pulses with arbitrary polarization*, Physical Review A **87**, 053803, 2013.

Additional publications not included in the thesis:

VI S. A. Sørngård, M. Førre and J. P. Hansen, *Angular resolved phonon emission from excited quantum dots*, New Journal of Physics **14**, 013035, 2012.

VII J. P. Hansen, S. A. Sørngård, M. Førre and E. Räsänen, *Quantitative modeling of spin relaxation in quantum dots*, Physical Review B **85**, 035326, 2012.

List of Abbreviations

ATI	Above threshold ionization
CTMC	Classical trajectory Monte Carlo
DATI	Double electron above threshold ionization
GTO	Gaussian-type orbital
HHG	High-order harmonic generation
IE	Independent electron
Laser	Light amplification by stimulated emission of radiation
LOPT	Lowest-order perturbation theory
SAE	Single active electron
SFA	Strong-field approximation
TDSE	Time-dependent Schrödinger equation
TPDI	Two-photon double ionization

CONTENTS

LIST OF FIGURES

CHAPTER 1

INTRODUCTION

The blink of an eye, lasting about the tenth of a second, is the epitome of a fast process in a human perspective. Seen from an electron's point of view, orbiting the hydrogen atom approximately 10^{17} times a second, this infinitesimal time period of a human life is an eternity. If they could, the electrons would blink their eyes in attoseconds[1], and it is on this time scale, the time scale of the electrons, the processes discussed in this thesis take place.

In this microscopic world of tiny structures and swift processes everything is governed by the laws of quantum mechanics, one of the pillars of modern physics. Quantum mechanics is often traced back to Max Planck. In 1900 he was the first to introduce the concept of quantized energy when deriving a new formula for the blackbody radiation [1], and thereby solving one of the puzzles of his time – the ultraviolet catastrophe. Another milestone in the development of quantum mechanics was reached when Albert Einstein in 1905 published a paper explaining the photoelectric effect [2]. It had been known since the experiments of Heinrich Hertz in the late 1880s that charged objects may become discharged when subjected to ultraviolet light [3]. What Einstein realized, in accordance with Planck's theory, was that the change in charge was caused by the material absorbing quanta of light and subsequently ejecting electrons.

In the years to follow the light quanta, or *photons* as we know them today, kept appearing in the physicists' equations. When Niels Bohr formulated his atomic model of stationary orbitals in 1913 [4–6] it was with the photon in the lead role. This pioneering model, despite some erroneous assumptions, was the first to provide an expression for the energy levels in the hydrogen atom. In many respects Bohr's model forms the basis for our understanding of the atom, comprising the conceptual idea of how the electrons can only occupy certain energy levels, and is as such a useful tool even today. Nevertheless, it was not until the emergence of the true quantum mechanics in the mid 1920s that a comprehensive description of the atom, and in principle any quantum system, came about.

The doctoral thesis of Louis de Broglie of 1924 was based on a groundbreaking hypothesis which paved the way for the development of the "modern" quantum mechanics. In short, it stated that all matter may be described in terms of waves in analogy with the particle-wave duality already established for light. In the ensuing years no less than two formulations of quantum mechanics were presented. In contrast to the previ-

---

[1] An attosecond is 0.000 000 000 000 000 001 seconds.

ous quantum theories that had been put forward by Niels Bohr and others, one were at this point able to provide a logically consistent formulation. The two mathematically equivalent representations, the matrix mechanics by Werner Heisenberg, Max Born and Pascual Jordan [7, 8], and the wave mechanics by Erwin Schrödinger [9–11], were published in 1925 and 1926, respectively. In the immediate time after the publications most physicists seemed to embrace Schrödinger's formulation and its resemblance to familiar concepts in classical physics. It introduced the much celebrated Schrödinger equation which can be perceived as the quantum mechanical analogue to the Newton's second law, and is perhaps the most prominent symbol of quantum mechanics. The Schrödinger equation is a partial differential equation in the three spatial coordinates in addition to the time, and its solution is known as the wavefunction. Heisenberg's formulation, on the other hand, appeared to be on a higher level of abstraction representing all observables as matrices, the measured values as eigenvalues, and the corresponding quantum states as eigenvectors. Although it received a lukewarm reception at first, Heisenberg's theory is a prerequisite for today's large scale calculations in the field of computational quantum mechanics.

Alongside the mathematical formulations came the interpretations. There are several approaches to the subject, but the most widespread is the one coined the *Copenhagen interpretation*. As the name suggests the basic ideas of this way of thinking were conceived in Copenhagen by Bohr and his, by then, research assistant, Heisenberg. The essence of the interpretation is the conception of the wavefunction as nothing but a theoretical tool, of which the absolute square is the probability density distribution of all possible outcomes. A measurement can, however, only result in a single value occurring according to this distribution. The process in which the measurement forces the quantum system to assume a single value is somewhat philosophically referred to as the *collapse of the wavefunction*. Two principles often associated with the Copenhagen interpretation is Heisenberg's *uncertainty principle* [12] and Bohr's *correspondence principle* [13]. The first one, the uncertainty principle, states that certain physical quantities cannot be simultaneously determined. For instance, a precise measurement of a particle's position prohibits a precise measurement of the corresponding momentum. The second, the correspondence principle, is an attempt to relate the quantum mechanics to what is observed in classical physics. More precisely, it asserts that in the limit of large structures and high energies the two perceptions must, to some approximation, coincide. Though of merely philosophical importance, it prevents contradictions between quantum mechanics and classical physics in the case of macroscopic objects.

By the end of the 1920s the work of the aforementioned persons together with other significant contributors, like Paul Dirac, Wolfgang Pauli, Enrico Fermi and Satyendra Nath Bose, had created a new framework in which the physics of even the smallest objects in nature can be described. The new physics challenged many of the established perceptions and ideas of those days, and could be rather confusing and unsatisfactory even for those directly involved. The latter is expressed in the quote by Schrödinger [14]:

> *"I don't like it, and I'm sorry I ever had anything to do with it."*

Or as Richard Feynman put it in one of his famous lectures from the 1960s [15]:

> *"I think I can safely say that nobody understands quantum mechanics."*

But in any regards, the quantum theory represented a paradigm shift in physics, and turned out to be decisive for the development in science and ultimately for the everyday life of people.

As already mentioned, the first system to be subject to a quantum mechanical treatment was the hydrogen atom. In a quantum mechanical context the hydrogen atom is unique in that it is one of the few systems where the solution to the Schrödinger equation is expressed in terms of analytical functions. This is true as long as there is a single electron in the atom and it is totally isolated from its surroundings. Once these requirements are violated, for instance by introducing a second electron or an electric field, this elegant analyticity disappears. Consequently, the mathematical complexity of the solution increases making the process of finding it a challenging affair. This fact either calls for a numerical solution, clever approximations or both of them combined. The increase in complexity is related to one of the profound principles of the quantum theory; all possible scenarios must be taken into account. Accordingly, the wavefunction of a two-electron atom contains all the information there is to know about both particles at once, and it is actually impossible to completely distinguish between what is related to each of them. In general, the Schrödinger equation can be solved exactly for one single or for two interacting electrons exposed to external fields. As the workload scales badly with the number of interacting particles, to include three of them is, unfortunately, far beyond reach even with the most powerful supercomputers.

In this thesis several atomic and molecular systems are discussed, i.e., the hydrogen atom (Paper II and IV), the helium atom (Paper I), the diatomic hydrogen molecule (Paper III), and the carbon allotrope of graphene (Paper V). Since the early days of quantum mechanics one has been aware that the energy of electromagnetic waves can be transferred to matter. In response, the electron will either go from one energy level to another or completely escape the nuclear attraction ending up as a free particle. The latter is termed photoionization and will occur if the energy of the light somehow exceeds the binding energy of the electron. The overall motivation for all the studies included is to scrutinize the process of photoionization in these systems when they are exposed to short laser pulses of varying intensity. The rest of this introduction will be devoted to what happens when an atomic or molecular system interacts with the coherent light of a laser.

The laser, or more precisely, the phenomenon of *Light Amplification by Stimulated Emission of Radiation*[2] was postulated by Albert Einstein already in 1916 in his theoretical work on absorption and emission of light quanta in atoms [17]. From the very beginning and until the first functional solid state laser was realized by Theodore H. Maiman at the Hughes Research Laboratories [18], it took more than forty years. The lasers of the early 1960s delivered focused peak intensities on the order of 10^9 W cm^{-2}, but since then there has been a tremendous development in laser technology. The state of the art laser technology is capable of delivering pulses of ultrahigh intensity ($\sim 10^{21}$ W cm^{-2} [19]) and down to attosecond duration, though not in one laser setup. A laser can be tuned to generate pulses within a narrow band of frequencies matching the energies of the electrons in atoms and molecules. This has resulted in lasers being

---

[2] The term was first used by R. Gordon Gould in 1959 [16].

one of the most important research tools in the investigation of light-matter interactions.

For the weakest laser fields there is a one-to-one correspondence between the number of photons with sufficient energy absorbed and the number of ejected electrons, in accordance with Einstein's photoelectric effect. In other words, each photon knocks free one electron. Although single-photon ionization has been extensively studied for almost a century, there are still unexplored exotic atomic systems where new insight may be gained from these processes.

Regarding exotic atomic systems, a perfect example of such is the Rydberg atom[3]. Rydberg atoms are atoms where the "outermost" electron is found in a highly excited state, i.e., a state having an energy far larger than the ground state, the lowest energy configuration. In general, being in a highly excited state is synonymous with being on average far away from the nucleus. Moreover, as the "innermost" electrons will effectively shield most of the nuclear charge, the attractive Coulomb force, as seen from the Rydberg electron, is to a good approximation that of hydrogen. The Rydberg atoms are therefore often characterized by large values of the *principal quantum number* n, the energy quantum number of the hydrogen atom. This fact implies that the Rydberg atom has some unique properties like long lifetime and exaggerated response to electric and magnetic fields. In addition, the wavefunction of such a system will in some sense behave like a classical orbital concordant with Bohr's atomic model, and might as well be seen as a manifestation of the correspondence principle.

Increasing laser intensity allows for sophisticated laser-matter interactions of higher order than the above-mentioned single-photon ionization process. The first one to predict this phenomenon was Maria Göppert-Mayer who in 1929 showed theoretically that an electron may absorb two photons to gain enough energy for it to escape the nucleus [20]. This clearly violates Einsteins photoelectric effect, but to his defense, these transitions were not experimentally feasible until the invention of the laser in the 1960s. In general, Göppert-Mayer's idea extends to n photons implying that photons of energy far less than the binding energy of the electron are collectively able to ionize the atom. The process is known as *multiphoton ionization*, and for it to take place in laser-atom interactions a minimum intensity of $10^8\,\mathrm{W\,cm^{-2}}$ is required [21].

So far we have mentioned that one or more photons may trigger a *single* ionization event. But there is more to it; one or more photons can in principle multiple ionize an atom or molecule. An important subclass is the case where N electrons are ejected from an N electron system. These processes are special in the sense that they result in a complete breakup of the system leaving behind the electrons and the bare nucleus/nuclei as free particles. An example of such a process is the one-photon double ionization of helium, a process that have been thoroughly studied since the discussion was initiated by F. W. Byron and C. J. Joachain in the mid 1960s [22]. Advancing in complexity, the next level is the more intricate process of two-photon double ionization. What adds an extra aspect to this two-photon process is the fact that it either happens sequentially or directly (non-sequentially), depending on the photon energy. In the first case, the electrons are ionized one at a time by one photon each, whereas in the second case, both electrons are ejected simultaneously. The two-photon double ionization of helium has been extensively examined since the end of the 1990s [23–32], and recently the studies have also been extended to the hydrogen molecule [33–36].

---

[3] Named after the Swedish physicist Johannes Rydberg.

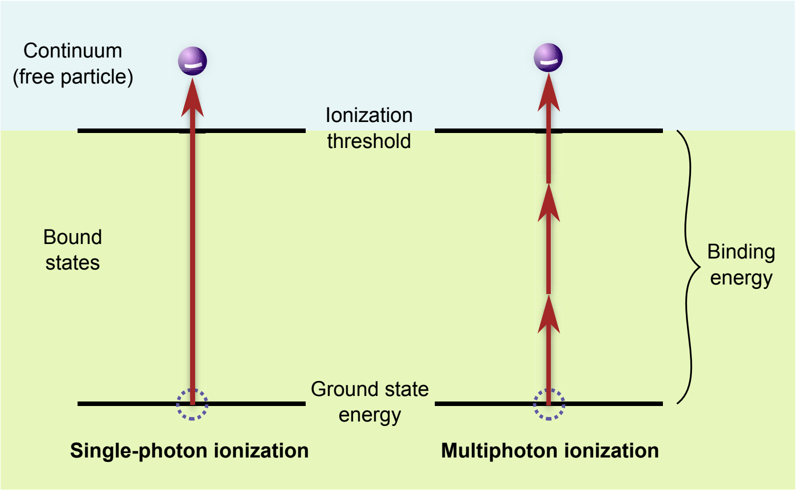

Figure 1.1: An illustration of the single-photon and multiphoton ionization processes. The electrons (blue balls) are initially in the ground state level, and are supplied with a sufficient amount of energy, by one or more photons (red arrows), for them to exceed the ionization threshold. The energy is increasing in the vertical direction.

In atomic and molecular physics one separates between weak and strong fields. As a rule of thumb the boundary is drawn where the intensity of the laser exceeds $10^{13}\,\mathrm{W\,cm^{-2}}$ [37]. Whereas weak field processes can be examined using so-called perturbation theory, being low-order approximations to the solution of the Schrödinger equation, the strong field regime calls for methods of higher order. One obvious approach is to solve the Schrödinger equation "brute-force", but as mentioned this is challenging and is only doable for the simplest systems. Another method which is extensively used in the study of non-perturbative processes is the strong-field approximation developed by L. V. Keldysh, F. H. M. Faisal and H. R. Reiss [38–40]. In this approximation it is assumed that the force of the laser is so strong that it completely dominates that of the Coulomb potential, which is consequently disregarded.

One strong field phenomenon discussed in this thesis is the high-order harmonic generation. Harmonic generation, in general, refers to the process where an atom interacting with a laser field emits radiation at frequencies being multiples of the initial frequency of the laser. The appearance of these augmented frequencies is attributed to the energy the electron gains from the driving electric field. Following in the wake of the invention of the laser, the third harmonics was observed by G. H. C. New and J. F. Ward back in 1967 [41]. Since then harmonics of ever increasing order have been reported in line with the development in laser power. The first experimental evidence of *high-order* harmonic generation appeared in the late 1980s [42, 43]. It has since been a hot topic as it is in itself a source of coherent extreme-ultraviolet laser pulses of attosecond duration [44–46].

Roughly two decades ago, about the time the first high-order harmonic spectra were presented, another strong field phenomenon was discovered, but this time in calculations. Studies of the ionization probability of an atom as a function of the laser intensity, revealed an unexpected result in the regime where the applied laser forces dominate the Coulomb attraction [47–54]. Instead of monotonically increasing until reaching 100% probability of ionization, as foreseen by perturbation theory, the ionization probability stabilized at a lower level or even started to subside. The phenomenon, given the descriptive name *atomic stabilization*, has since its discovery been subject of intense debate and controversy as to whether it really represents a physical process. Much of the discussion can be ascribed to the lack of experimental verification. For instance, for stabilization to be observed in atomic hydrogen, photon energies exceeding the binding energy of 13.6 eV, and intensities of at least $10^{16}\,\mathrm{W\,cm^{-2}}$ are required. This was not within reach of the laser technology of the early 1990s, and to the present, the only experimental evidence of stabilization comes from studies of low-lying Rydberg states in neon and barium [55–57]. As for the intensity the laser technology is advancing towards the regime where atomic stabilization in ground state atoms can be observed, but to the misfortune of stabilization studies, the increase in intensity is accompanied by an increase in laser frequency. One example is the free-electron laser technology capable of delivering pulses of extremely high peak intensities and wavelengths ranging from vacuum ultraviolet to soft x-rays.

In the following chapters the theory and the physics behind the five papers that are included is outlined. In addition to these five, two more papers have been published during the PhD-study. They are not included as they concern spontaneous phonon emission in quantum dots rather than photoionization, and thus fall beyond the scope of the dissertation.

Atomic units, where the electron mass m_e, the Planck's constant $\hbar$ and the elementary charge e are scaled to unity, are used throughout unless stated otherwise. A detailed description of these units is found in Appendix A.

CHAPTER 2

ATOMS IN EXTERNAL FIELDS

2.1 Basic concepts

As for theory, atomic and molecular physics can be reduced to solving, either exactly or approximately, one central partial differential equation, the Schrödinger equation, here presented in its time-dependent form,

$$\mathrm{i}\frac{\partial}{\partial t}\Psi(\mathbf{r},t) = H\Psi(\mathbf{r},t). \tag{2.1}$$

Its solution, the wavefunction $\Psi(\mathbf{r},t)$, contains all the information there is to know about the quantum system at a given time t. The physics of the system itself is incorporated in the operator H called the Hamiltonian. For instance, for the simplest atomic system in nature, the hydrogen atom, it reads

$$H_0 = \frac{\mathbf{p}^2}{2} - \frac{1}{r}. \tag{2.2}$$

In this expression the first term is the kinetic energy operator comprising the square of the momentum operator $\mathbf{p}$, and the second term is the Coulomb potential modeling the interaction between the electron and the nucleus. The complexity of the Hamiltonian is in general increasing with the intricacy of the system, and may include the electron-electron interaction, the electron-nucleus interaction, the light-matter interaction, spin interactions and so on. One notices that the Schrödinger equation is of first order in the time derivative. It means that once the wavefunction is known at a time t_0 it can in principle be obtained for an arbitrary time t thereafter. This feature is frequently exploited in this work when dealing with the time-dependent interaction between lasers and matter, and the wavefunction is to be propagated in time.

Given a particle of charge q and mass m, the Hamiltonian which embodies the interaction with an electromagnetic field, at the most fundamental level, is given by

$$H = \frac{1}{2m}\left[\mathbf{p} - q\mathbf{A}(\mathbf{r},t)\right]^2 + q\phi(\mathbf{r},t), \tag{2.3}$$

where $\phi(\mathbf{r},t)$ and $\mathbf{A}(\mathbf{r},t)$ are the scalar and vector potentials which model the laser field. From classical electrodynamics it is known that the general solution to Maxwell's equations, i.e., the electric and magnetic field, can be expressed in terms of $\mathbf{A}$ and ϕ,

$$\begin{aligned}\mathbf{E}(\mathbf{r},t) &= -\frac{\partial}{\partial t}\mathbf{A}(\mathbf{r},t)-\nabla\phi(\mathbf{r},t) &(2.4)\\ \mathbf{B}(\mathbf{r},t) &= \nabla\times\mathbf{A}(\mathbf{r},t). &(2.5)\end{aligned}$$

However, there is a degree of freedom in the choice of $\mathbf{A}$ and ϕ, that is, $\mathbf{A}'(\mathbf{r},t) = \mathbf{A}(\mathbf{r},t)+\nabla\lambda(\mathbf{r},t)$ and $\phi'(\mathbf{r},t)=\phi(\mathbf{r},t)-\partial\lambda(\mathbf{r},t)/\partial t$ result in the same physical fields $\mathbf{E}$ and $\mathbf{B}$. The different options are called *gauges*, and though the classical fields are not influenced, the wavefunction is left with an additional phase factor,

$$\Psi'(\mathbf{r},t)=\Psi(\mathbf{r},t)e^{iq\lambda(\mathbf{r},t)}. \tag{2.6}$$

Throughout the thesis two such gauges are employed, the *length gauge*[1], and the *velocity gauge*, given by the two Hamiltonians

$$H^{\mathrm{lg}}=\frac{\mathbf{p}^2}{2m}-q\mathbf{r}\cdot\mathbf{E}(t), \tag{2.7}$$

and

$$H^{\mathrm{vg}}=\frac{\mathbf{p}^2}{2m}-\frac{q}{m}\mathbf{A}(t)\cdot\mathbf{p}+\frac{q^2}{2m}\mathbf{A}^2(t), \tag{2.8}$$

respectively. Note that in the Eqs. (2.7) and (2.8) the electric field and the vector potential are assumed to be space-independent. This is the result of a commonly used approximation called the *dipole approximation*. The wavelength of the laser light is typically much larger than the extent of the atomic system, and the spatial variation of the fields is consequently disregarded, i.e., it is expanded to zeroth order,

$$\mathbf{A}(\mathbf{r},t)=\hat{\boldsymbol{\varepsilon}}\int_0^\infty A_0(\omega)\exp[i(\omega t-\mathbf{k}\cdot\mathbf{r})]d\omega\approx\hat{\boldsymbol{\varepsilon}}\int_0^\infty A_0(\omega)\exp(i\omega t)d\omega. \tag{2.9}$$

As a result, it is seen from Eq. (2.5) that within the dipole approximation the magnetic field is zero as it solely depends on the spatial variation of the vector potential. Furthermore, as the last term in Eq. (2.8) is purely time-dependent, it will give rise to a phase factor in the solution of the Schrödinger equation. As this phase is of no physical importance the term is often transformed away by a unitary transformation.

The unitarity of the gauge transformation [Eq. (2.6)] ensures all measurable quantities, like expectation values and probabilities, to be gauge invariant given that $\Psi(\mathbf{r},t)$ is the exact solution of the Schrödinger equation. Therefore the choice of gauge is merely a computational issue considering convergence of the calculations, and not of fundamental physical significance. Nonetheless, when the solution is found using approximate methods the gauge invariance is not necessarily guaranteed, and the choice of gauge may be of crucial importance for the validity of the approximation. Such an example is briefly discussed in Sec. 3.2 in connection with high-order harmonic generation. In addition to the length gauge and the velocity gauge, there is a third option, the *Kramers-Henneberger frame* [58, 59]. When applying this transformation the inertial frame of the system follows the motion of a free classical particle in the field. Though it is often referred to as the *acceleration gauge*, it is strictly speaking not a gauge since it cannot be obtained through a gauge transformation [60]. The Kramers-Henneberger frame is well suited in the strong-field limit, and is in this work used when explaining the phenomenon of atomic stabilization in helium.

---

[1] The length gauge is also often referred to as the Göppert-Mayer gauge.

2.2 Hydrogen Rydberg wave packets in a Stark manifold

2.2.1 The hydrogen atom

Insertion of the hydrogen Hamiltonian [Eq. (2.2)] into the time-dependent Schrödinger equation [Eq. (2.1)] results in the emergence of the time-independent Schrödinger equation

$$H_0\psi_{nlm}(\mathbf{r}) = E_n\psi_{nlm}(\mathbf{r}), \tag{2.10}$$

where the time dimension is factored out. In this expression E_n is the energy of the eigenstates ψ_{nlm} having the same principal quantum number $n = 1, 2, \ldots$. The solution to Eq. (2.10) is known analytically and separates into a radial part and an angular part,

$$\psi_{nlm}(\mathbf{r}) = R_{nl}(r)Y_{lm}(\theta,\phi). \tag{2.11}$$

The radial part is essentially given by $r^l \mathrm{e}^{-r/n}L_{n+1}^{2n+1}(2r/n)$ with the latter function being an associated Laguerre polynomial. The angular part is expressed in terms of functions known as spherical harmonics. In addition to n there are two quantum numbers l and m related to the orbital angular momentum and the projection of this quantity along one of the axes (usually the z-axis), respectively. What is unique about the hydrogen atom is that the energy depends only on the principal quantum number which defines the main shells. Within each such shell the other quantum numbers form energetic degenerate sub-shells conforming to the constrains $l \leq n-1$ and $|m| \leq l$. This implies that one n-shell consists of n^2 states.

If the energy is positive, the electron is no longer bound to the nucleus, and there is a continuum of possible states to occupy. As the principal quantum number is meaningless in the continuum, these states are instead characterized by their energy E_k or momentum k. The Coulomb waves as they are called, are defined by

$$\psi_{klm}(\mathbf{r}) = \mathrm{i}^l e^{-\mathrm{i}\sigma_l}Y_{lm}(\hat{\mathbf{r}})Y_{lm}^*(\hat{\mathbf{k}})R_{kl}(r), \tag{2.12}$$

where $\sigma_l = \arg\Gamma(l+1-\mathrm{i}/k)$ is the Coulomb phase shift. The radial part, when normalized in momentum space[2], reads [61],

$$R_{kl}(r) = \sqrt{\frac{2}{\pi}}\frac{e^{\pi/2k}|\Gamma(l+1-\mathrm{i}/k)|}{(2l+1)!}(2r)^l k^{l+1}e^{-\mathrm{i}kr}{}_1F_1(l+1+\mathrm{i}/k, 2l+2, 2\mathrm{i}kr). \tag{2.13}$$

2.2.2 The Stark and Zeeman effects

The energetic degeneracy within an n-shell is lifted if an electric or magnetic field is introduced. In the first case the phenomenon is called the Stark effect, and in the second, the Zeeman effect. A Hamiltonian where both of them are included is given by

$$H = H_0 + \mathbf{E}(t)\cdot\mathbf{r} + \frac{1}{2}\mathbf{B}(t)\cdot\mathbf{L}, \tag{2.14}$$

where H_0 is as defined in Eq. (2.10), the second term represents the Stark effect, and the third term represents the Zeeman effect. In the latter, $\mathbf{L}$ is the angular momentum operator.

---

[2] The corresponding energy normalized wavefunction is obtained through the scaling $R_{E_kl}(r) = k^{-1/2}R_{kl}(r)$.

Consider now an electron that is somehow initially excited to a non-degenerate Rydberg n-shell. Under the assumption that the electric and magnetic fields are weak and that they are slowly varying in time, inter-shell transitions are very unlikely as they require a large number of photons. This means that in practice the electron is trapped, and that the only allowed transitions are those within the shell (intra-shell transitions).

As long as the dynamics of the interaction pertains to a single n-shell, the spatial coordinate in the coupling $\mathbf{E} \cdot \mathbf{r}$ may be expressed in terms of the *Runge-Lenz operator* $\mathbf{a}$ through what is known as Pauli's operator replacement [62],

$$\mathbf{r} = \frac{3}{2} n \mathbf{a}. \tag{2.15}$$

In addition, if two pseudospin operators

$$\mathbf{J}_{\pm} = \frac{1}{2}(\mathbf{L} \pm \mathbf{a}) \tag{2.16}$$

are introduced together with the angular velocities

$$\boldsymbol{\omega}_{\pm} = \frac{1}{2}\mathbf{B} \pm \frac{3}{2} n \mathbf{E}, \tag{2.17}$$

the field-dependent part of the Hamiltonian in Eq. (2.14) simply reads

$$H' = \boldsymbol{\omega}_{+} \cdot \mathbf{J}_{+} + \boldsymbol{\omega}_{-} \cdot \mathbf{J}_{-}. \tag{2.18}$$

It can be shown [63] that the eigenvalues of H' becomes

$$E_{m_+,m_-} = m_+ |\boldsymbol{\omega}_+| + m_- |\boldsymbol{\omega}_-|, \tag{2.19}$$

with $m_{\pm} = -j, -j+1, \ldots, j-1, j$, where $j = (n-1)/2$. In the limit where the magnetic field dominates (Zeeman limit) the quantum numbers $m_{\pm}$ are related to the hydrogen quantum number m by $m = m_+ + m_-$. On the other hand, if the electric field dominates (Stark limit), they are connected to the Stark quantum numbers k and m via $k = m_+ + m_-$ and $m = m_+ - m_-$.

From now on we restrict our attention to the case where the magnetic field is zero, and the electric field ε_z is constant and oriented in the z-direction. This implies that the Stark quantum number m is identical to its counterpart in the hydrogen atom. There are as many Stark states ψ_{nkm} as there are field free hydrogen states ψ_{nlm} within an n-shell. An expression for the energies of the system is readily obtained from the Eqs. (2.17) and (2.19) combined with k and m in the Stark limit,

$$E_k = \frac{3}{2} k n \varepsilon_z. \tag{2.20}$$

The states having positive m are shown in the left panel of Fig. 2.1, with the energy increasing in the vertical direction. The rightmost and the leftmost (not shown) states in the Stark manifold are the so-called circular states with quantum numbers $(n,k,m) = (16,0,\pm 15)$. The term circular stems from the torus-shape of the electron "cloud" (wavefunction). These two are identical to the hydrogen eigenstates with quantum numbers $(n,l,m) = (16,15,\pm 15)$. Furthermore, the uppermost and the lowermost states, with quantum numbers $(n,k,m)=(16,\pm 15,0)$, are referred to as the linear Stark states. Given the electric field is pointing in the z-direction, the Stark states can be written as a linear combination of the hydrogen eigenstates having the same n and m [64]

$$\psi_{nkm}(\mathbf{r})=\sum_{l}(-1)^{l}\left\langle \frac{n-1}{2},\frac{m-k}{2},\frac{n-1}{2},\frac{m+k}{2}\middle| lm\right\rangle \psi_{nlm}(\mathbf{r}). \tag{2.21}$$

The expansion coefficients are called Clebsch-Gordan coefficients.

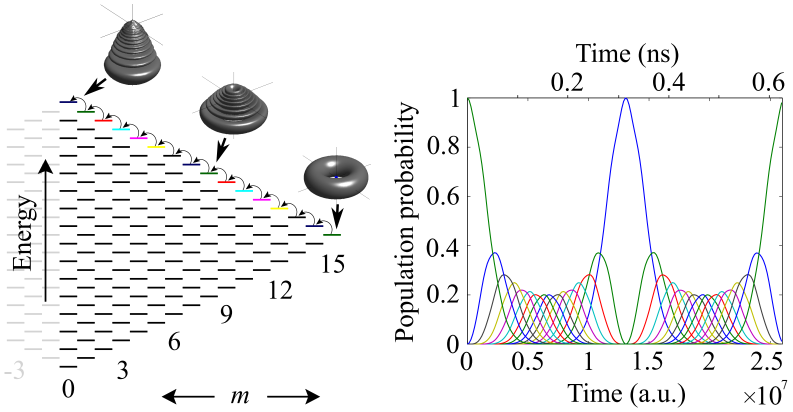

Figure 2.1: Left panel: Stark states ψ_{nkm} of the $n=16$ level due to the constant electric field ε_z. The states populated by the rotating microwave field in the xy-plane are shown in color. The wavefunctions of $|nkm\rangle = |16\ 15\ 0\rangle$, $|nkm\rangle = |16\ 7\ 8\rangle$ and $|nkm\rangle = |16\ 0\ 15\rangle$ are depicted. Right panel: The population of the Stark states as a function of time for one round trip in the Stark setup. The figure is taken from Paper IV.

2.2.3 Femtosecond-pulse-train ionization of a Rydberg wave packet

In Paper IV a weak time-dependent clockwise rotating microwave field,

$$\mathbf{E}_{\mu}(t)=\varepsilon_0 \cos\omega_{\mu} t\hat{\mathbf{x}}-\varepsilon_0 \sin\omega_{\mu} t\hat{\mathbf{y}}, \tag{2.22}$$

is used to drive a wave packet between the levels in the $n=16$ Stark manifold which in turn is split by the electric field $\varepsilon_z = 10^{-7}$ a.u. The frequency ω_{μ} is chosen to match the energy splitting ΔE, and the strength of the microwave field is $\varepsilon_0 = 10^{-8}$ a.u.

It is well known in quantum mechanics that a field in the x- or y-direction can only drive transitions between states fulfilling the relations $|\Delta l| = 1$ and $|\Delta m| = 1$. In this particular Stark setup an additional selection rule manifest itself, i.e., $|\Delta k| = 1$. The selection rules significantly reduce the number of allowed transitions in the Stark manifold. It can be shown that this number is even smaller by considering the rotation direction of the electric field. According to Eq. (2.21) the angular matrix element between the initial state ψ_{nkm} and the final state $\psi_{n'k'm'}$ is a linear combination of matrix elements of the kind

$$\left\langle Y_{l'm'}\middle|\mathbf{E}_{\mu}(t)\cdot\hat{\mathbf{r}}\middle|Y_{lm}\right\rangle=\left\langle Y_{l'm'}\middle|E_{\mu_x}(t)\sin\theta\cos\phi+E_{\mu_y}(t)\sin\theta\sin\phi\middle|Y_{lm}\right\rangle. \tag{2.23}$$

A trick of the trade is to rewrite the trigonometric functions in terms of the two spherical harmonics $Y_{1,\pm 1}(\theta,\phi) = \mp\sqrt{3/8\pi}\sin\theta\exp(\pm i\phi)$. Hence, Eq. (2.23) is proportional to

$$\left\langle Y_{l'm'} \middle| \left[-E_{\mu_x}(t) + \mathrm{i}E_{\mu_y}(t)\right] Y_{1,1} + \left[E_{\mu_x}(t) + \mathrm{i}E_{\mu_y}(t)\right] Y_{1,-1} \middle| Y_{lm} \right\rangle . \tag{2.24}$$

Upon substitution of the components of Eq. (2.22), Eq. (2.24) becomes,

$$\varepsilon_0 \langle Y_{l'm'} | Y_{1,-1} | Y_{lm} \rangle \, \mathrm{e}^{-\mathrm{i}\omega_\mu t} - \varepsilon_0 \langle Y_{l'm'} | Y_{1,1} | Y_{lm} \rangle \, \mathrm{e}^{\mathrm{i}\omega_\mu t}. \tag{2.25}$$

The orthonormality properties of the spherical harmonics [21] imply that the latter equation is proportional to

$$\varepsilon_0 \big(\delta_{m',m-1} \underbrace{\mathrm{e}^{-\mathrm{i}\omega_\mu t}}_{\text{absorption}} - \delta_{m',m+1} \underbrace{\mathrm{e}^{\mathrm{i}\omega_\mu t}}_{\text{emission}} \big) \delta_{l',l\pm 1}. \tag{2.26}$$

It is known from perturbation theory that the first operator in Eq. (2.26) corresponds to the system absorbing an energy ΔE, and that the second leads to emission of the same energy amount. From this we conclude that the angular momentum (the m quantum number) is decreasing when the energy of the electron is increasing, and the other way around. This conveys that if initially the circular state is fully populated, the population will gradually flow towards the linear state as indicated in the left panel of Fig. 2.1. Moreover, when the linear state is fully populated and the circular state is depleted, the process repeats itself but now in the opposite direction.

We now have a Rydberg wave packet that is slowly evolving in the Stark manifold, making one round trip between the circular state and the linear state in $\tau = 2.6 \times 10^7$ a.u. (corresponding to 0.6 ns). The population probability of the different Stark states as a function of time is displayed in the right panel of Fig. 2.1. The idea is to investigate the ionization dynamics of the wave packet using a train of femtosecond pulses. Apparently, the microwave field and the laser pulses act on different time-scales. Hence, from the femtosecond pulse's point of view the motion of the wave packet due to the microwave field seems frozen in time. The intra-shell dynamics of the wave packet is calculated by means of time propagation of the solution to the Schrödinger equation. By keeping the field strength sufficiently low ($E_0 = 2.0 \times 10^{-5}$ a.u.), only a small fraction of the wave packet is transferred to the continuum at each burst of the pulse-train. This, in combination with the wave packet being practically unaltered by the microwave field during the pulses, admits the action of each laser pulse to be treated within the frame of first-order perturbation theory, temporary neglecting the intra-shell dynamics. The jth transition amplitude between the (bound) wave packet $\Psi_{\mathrm{b}}(t)$ and one particular continuum state ψ_{qlm} of momentum q is then given by

$$a_{qlm}^{(j)} = -\mathrm{i} \int_{t_j}^{t_j+T} \left\langle \psi_{qlm} | \mathbf{E}(t) \cdot \mathbf{r} | \Psi_{\mathrm{b}}(t) \right\rangle \mathrm{e}^{\mathrm{i}(E_q - E_{\mathrm{b}})t} \mathrm{d}t. \tag{2.27}$$

In this expression the laser-matter interaction is formulated in the length gauge. E_{b} and E_q are the energies of the initial state and the final state, and T is the pulse duration. From Eq. (2.27) it follows that after the jth pulse the continuum part of the wavefunction becomes

$$\Psi_{\mathrm{c}}(t_j + T) = \sum_{q,l,m} \sum_{j=1}^{N} a_{qlm}^{(j)} | \psi_{qlm} \rangle e^{-\mathrm{i}E_q (N-j)\Delta t}, \tag{2.28}$$

where the transition amplitudes serve as expansion coefficients.

Figure 2.2 presents a plot of the ionization probability as a function of the number of pulses in the pulse-train and the time separation Δt between them. In general, the ionization probability is larger the closer the wave packet is to the linear state, resulting in the ridges and valleys of the figure. It is observed that the maximum is reached when $\Delta t = \tau/2$, that is, every second pulse hits the linear state. There are also two minima that stand out at $\Delta t = \tau/3$ and $\Delta t = 2\tau/3$, where the laser pulse always strikes when the wave packet is in the vicinity of but not sufficiently close to the linear state.

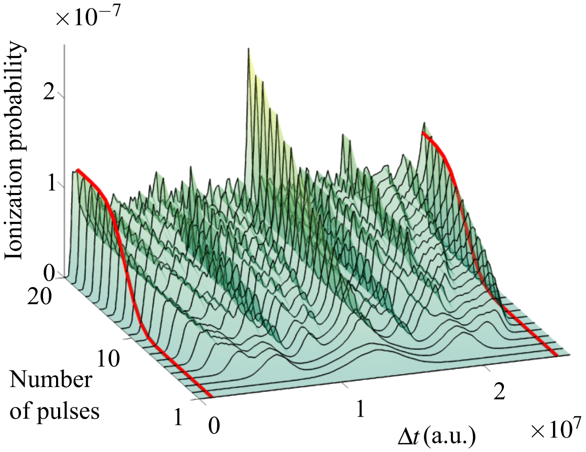

Figure 2.2: The ionization probability as a function of N succeeding pulses and time delay Δt. The initial state prior to the pulse-train is $|nkm\rangle = |16\ 0\ 15\rangle$. The figure is taken from Paper IV.

CHAPTER 3

THE STRONG-FIELD APPROXIMATION AND HIGH-ORDER HARMONIC GENERATION

As stated in the introductory chapter, one possible approach to solve the Schrödinger equation in the strong field regime is to apply the strong-field approximation. In this chapter the strong-field approximation is used in the derivation of an expression for the high-order harmonic spectrum of an extended molecule.

3.1 The strong-field approximation

3.1.1 The Volkov state

We start the discussion by introducing the main constituent of the strong-field approximation, the Volkov states. The behavior of a free electron only influenced by an electric field is fully described by the following time-dependent Schrödinger equation

$$[T + V_\mathrm{L}(\mathbf{r},t)]\,\psi(\mathbf{r},t) = \mathrm{i}\frac{\partial}{\partial t}\psi(\mathbf{r},t), \tag{3.1}$$

where T is the kinetic energy operator, and $V_\mathrm{L}(\mathbf{r},t)$ is $\mathbf{E}(t)\cdot\mathbf{r}$ and $\mathbf{A}(t)\cdot\mathbf{p}+\mathbf{A}^2(t)/2$ in length gauge and velocity gauge, respectively. In an atomic system where a strong laser field completely obscures the effect of the Coulomb potential, the solution to Eq. (3.1) may, under certain conditions, provide an adequate description of its continuum states. The solution to the TDSE is the Volkov state $\psi^\mathrm{V}_\mathbf{k}(\mathbf{r},t)$, which reads

$$\psi^\mathrm{V}_\mathbf{k}(\mathbf{r},t) = \frac{1}{(2\pi)^{3/2}}\exp\left[\mathrm{i}(\mathbf{k}+\mathbf{A}(t))\cdot\mathbf{r} - \mathrm{i}S(\mathbf{k},t,t_0)\right] \tag{3.2}$$

in the length gauge, and

$$\psi^\mathrm{V}_\mathbf{k}(\mathbf{r},t) = \frac{1}{(2\pi)^{3/2}}\exp\left[\mathrm{i}\mathbf{k}\cdot\mathbf{r} - \mathrm{i}S(\mathbf{k},t,t_0)\right] \tag{3.3}$$

in the velocity gauge. In both equations the space independent function S, called the classical action of the electric field, is given by the time integral of the kinematic momentum,

$$S(\mathbf{k},t,t_0) = \frac{1}{2}\int_{t_0}^{t}\mathrm{d}t'\,\left[\mathbf{k}+\mathbf{A}(t')\right]^2. \tag{3.4}$$

3.1.2 Derivation of the strong-field approximation

The time-dependent Schrödinger equation for an atom exposed to a laser field reads

$$[T+V(r)+V_{\mathrm{L}}(\mathbf{r},t)]\Psi(\mathbf{r},t)=\mathrm{i}\frac{\partial}{\partial t}\Psi(\mathbf{r},t), \tag{3.5}$$

where T is the kinetic operator, $V(r)$ is the Coulomb potential, and $V_{\mathrm{L}}(\mathbf{r},t)$ is the potential representing the laser-matter interaction. In what follows we will solve Eq. (3.5) using the strong-field approximation (SFA). The SFA method is based on three basic assumptions:

1. The initial state is not depleted when exposed to the electric field of the laser.
2. The atom can be approximated by one state only.
3. When the field is applied, the effect of the atomic core potential $V(r)$ on the continuum states is negligible. This approximation allows for the exact continuum states [cf. Eq. (2.12)] of the system to be replaced by the Volkov states [Eqs. (3.2) and (3.3)].

By the second and the third assumption an approximate solution to the TDSE in Eq. (3.5) may be written as the sum of the initial bound state and the continuum states

$$\Psi(\mathbf{r},t)=\psi_{\mathrm{b}}(\mathbf{r},t)+\int \mathrm{d}^3k\; c_{\mathbf{k}}(t)\,\psi_{\mathbf{k}}^{\mathrm{V}}(\mathbf{r},t), \tag{3.6}$$

where $\psi_{\mathbf{k}}^{\mathrm{V}}(\mathbf{r},t)$ represents the Volkov states. Moreover, it is assumed that the initial state $\psi_{\mathrm{b}}(\mathbf{r},t)=\phi_{\mathrm{b}}(\mathbf{r})\exp(-\mathrm{i}E_{\mathrm{b}}t)$ is the exact solution of the field free Schrödinger equation

$$[T+V(r)]\,\psi_{\mathrm{b}}(\mathbf{r},t)=\mathrm{i}\frac{\partial}{\partial t}\psi_{\mathrm{b}}(\mathbf{r},t). \tag{3.7}$$

Especially notice that the time dependence of the initial state in Eq. (3.6) is restricted to the trivial time-evolution in accordance with the first assumption. The Schrödinger equation [Eq. (3.5)] and the SFA-wavefunction [Eq. (3.6)], in combination with the Eqs. (3.4) and (3.7), lead to

$$\mathrm{i}\int \mathrm{d}^3k\; \dot{c}_{\mathbf{k}}(t)\,\psi_{\mathbf{k}}^{\mathrm{V}}(\mathbf{r},t)=V_{\mathrm{L}}(\mathbf{r},t)\,\psi_{\mathrm{b}}(\mathbf{r},t)+V(r)\int \mathrm{d}^3k\; c_{\mathbf{k}}(t)\,\psi_{\mathbf{k}}^{\mathrm{V}}(\mathbf{r},t). \tag{3.8}$$

By exploiting the orthogonality of the Volkov states, Eq. (3.8) may be rewritten

$$\mathrm{i}\dot{c}_{\mathbf{k}}(t)=\left\langle \psi_{\mathbf{k}'}^{\mathrm{V}}(\mathbf{r},t)\left|V_{\mathrm{L}}(\mathbf{r},t)\right|\psi_{\mathrm{b}}(\mathbf{r},t)\right\rangle+\int \mathrm{d}^3k\; c_{\mathbf{k}}(t)\left\langle \psi_{\mathbf{k}'}^{\mathrm{V}}(\mathbf{r},t)\left|V(r)\right|\psi_{\mathbf{k}}^{\mathrm{V}}(\mathbf{r},t)\right\rangle. \tag{3.9}$$

As it is assumed that the influence of the binding potential on the continuum states is negligible, the last term in Eq. (3.9) is consequently disregarded. A simple time integration yields the expansion coefficients of the continuum states

$$c_{\mathbf{k}}(t)=-\mathrm{i}\int_{-\infty}^{t}\mathrm{d}t'\;\left\langle \psi_{\mathbf{k}}^{\mathrm{V}}(\mathbf{r},t')\left|V_{\mathrm{L}}(\mathbf{r},t')\right|\psi_{\mathrm{b}}(\mathbf{r},t')\right\rangle. \tag{3.10}$$

3.2 High-order harmonic generation

3.2.1 The three-step model

The concept of high-order harmonic generation can be summed up in a simple semiclassical model commonly known as the *three-step model* or the *simple man's model*. The model was originally put forward by P. B. Corkum in 1993 [65] and explains, as the name suggests, the process of HHG in three steps. Consider an atom that is initially in a bound state of binding potential I_p, as shown in the first panel of Fig. 3.1. The time-dependent electric field of a laser perturbs the potential and the lowered potential barrier allows for the electron to tunnel out. This is the first step of the model. Second step: The electron is now assumed to be a free particle in the continuum with approximately zero kinetic energy. The electric field accelerates the liberated electron, which in this process gains energy. Third step: After half an optical cycle in the continuum the electron is again captured by the atomic potential, and the excess energy accumulated in the electric field is emitted as a photon of frequency ω. This frequency turns out to be odd multiples of the driving frequency ω_0 of the laser,

$$\omega = n\omega_0, \qquad n = 1,3,5,\dots \tag{3.11}$$

That there are only odd harmonics is the result of an interference effect owing to the half-cycle ionization-recombination pattern together with the assumption of a spatial symmetric atomic potential. Examples of media only producing odd harmonics are monatomic gases or gases of homonuclear molecules. Even harmonics, however, can be detected if this symmetry is broken, for instance by using a gas of heteronuclear molecules.

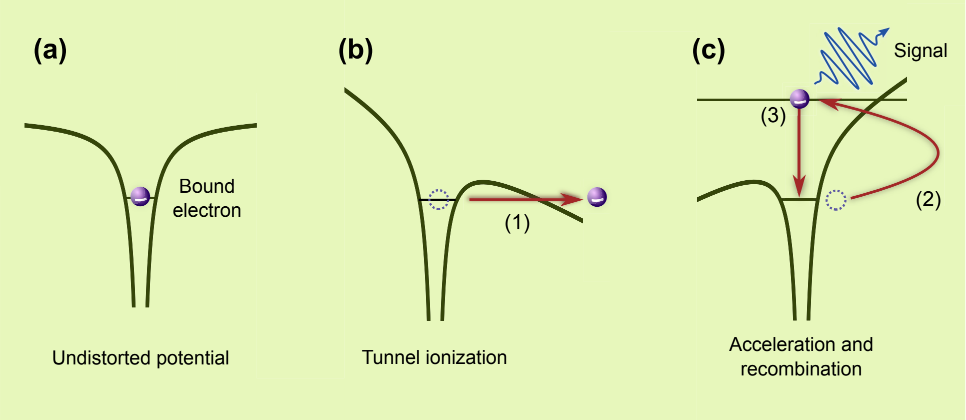

Figure 3.1: An illustration of the semiclassical three-step model. (a) An electron in a bound atomic state. (b) First step: the electron tunnels out of the potential which is perturbed by a laser field. (c) Second step: the liberated electron gains energy as it is accelerated by the laser field in the continuum. Third step: eventually the electron recombines with the ion, emitting a high-order harmonic signal.

3.2.2 Characteristics of the HHG spectrum

The frequency domain spectrum of the high-order harmonic signal is characterized by a large collection of amplitudes of comparable magnitude (on logarithmic scale), in HHG terminology referred to as the *plateau*. The plateau ends abruptly with the frequency components decreasing rapidly in magnitude, and the harmonic where this drastic change takes place is the so-called *cutoff*. The cutoff harmonic is associated with the maximum amount of energy the electron accumulates when propagating in the continuum. Assuming the electron recombines with the parent ion after a round-trip in the continuum, the maximum achievable cutoff harmonic is simply given by [65]

$$\omega_0 n_{\text{cutoff}} = I_{\text{p}} + 3.17 U_{\text{p}}, \tag{3.12}$$

where $U_{\text{p}} = E_0^2/4\omega_0^2$ is the ponderomotive energy of a free classical electron in the field, ω_0 is the central frequency of the laser pulse, and E_0 is the corresponding electric field amplitude. In a diatomic molecule, on the other hand, one can imagine that the electron ionizes at one atom and recombines at the other. If so is the case, the cutoff harmonic is found to be at maximum [66]

$$\omega_0 n_{\text{cutoff}} = I_{\text{p}} + 8 U_{\text{p}}. \tag{3.13}$$

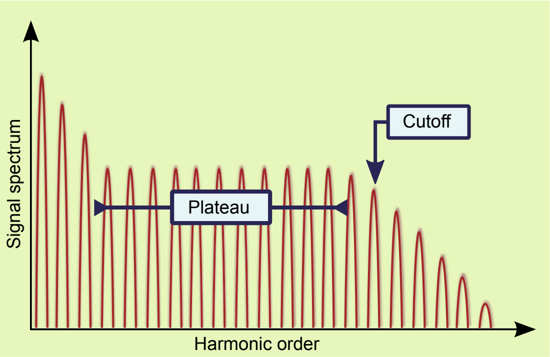

Figure 3.2: A simplified high-order harmonic spectrum.

3.2.3 High-order harmonic generation using the SFA

In calculations the high-order harmonic spectrum is calculated by taking the Fourier transform of either the dipole, the dipole velocity or the dipole acceleration. Take for instance the dipole velocity, the corresponding HHG spectrum is then found from the formula

$$S(\omega) = \left| \mathbf{n} \cdot \int_{-\infty}^{\infty} \mathrm{d}t \, \langle \Psi(\mathbf{r},t) \, | \mathbf{p} | \, \Psi(\mathbf{r},t) \rangle \, \mathrm{e}^{\mathrm{i}\omega t} \right|^2 . \tag{3.14}$$

The strong-field approximation, as described in Sec. 3.1.2, is commonly used in calculations of high-order harmonic generation. Assuming the laser-matter interaction is represented in the length gauge, the dipole velocity calculated using the SFA-wavefunction [Eq. (3.6)], with inserted the expansion coefficients [Eq. (3.10)], yields the expression known as the Lewenstein model

$$\begin{aligned}
&\langle\Psi(\mathbf{r},t)\,|\mathbf{p}|\,\Psi(\mathbf{r},t)\rangle \\
&\quad\approx\quad -\mathrm{i}\int_0^t \mathrm{d}t \int \mathrm{d}^3k\, \exp\left\{-\mathrm{i}\left[S(\mathbf{k},t,t')-E_\mathrm{b}(t-t')\right]\right\} \\
&\qquad\times \underbrace{\left[\int \mathrm{d}^3r\, \mathrm{e}^{-\mathrm{i}[\mathbf{k}+\mathbf{A}(t')]\cdot\mathbf{r}}\, V_\mathrm{L}^\mathrm{lg}(\mathbf{r},t')\,\psi_\mathrm{b}(\mathbf{r})\right]}_{\text{ionization}} \underbrace{\left[\int \mathrm{d}^3r\, \psi_\mathrm{b}(\mathbf{r})\mathbf{p}\, \mathrm{e}^{\mathrm{i}[\mathbf{k}+\mathbf{A}(t)]\cdot\mathbf{r}}\right]}_{\text{recombination}}. \\
&\qquad+\ \text{c.c.}
\end{aligned} \tag{3.15}$$

It is here assumed that the laser pulse has a finite duration, and that it is initiated at $t' = 0$. For symmetry reasons the direct term $\langle\psi_\mathrm{b}\,|\mathbf{p}|\,\psi_\mathrm{b}\rangle$, involving the bound state, is zero. The corresponding term involving the Volkov states is negligible given the continuum states are weakly interacting, hence the approximately equal sign. Equation (3.15) invites to a physical interpretation concordant with the semiclassical three-step model. Firstly, as indicated by braces, it is composed of one matrix element representing the ionization and one matrix element representing the recombination. Secondly, it is seen that the electron is transferred to the continuum at $0 < t' < t$ and that it recombines with the ion at time t. Notice that the limits of the classical action integral are different from those in Eq. (3.4)

If $\Psi(\mathbf{r},t)$ were the exact solution of Eq. (3.5) the high-order harmonic spectrum would have been independent of the choice of gauge. In contrast, for an approximate solution, like the one in Eq. (3.6), the result will, to a greater or lesser extent, be gauge dependent. An example of a situation where the gauge should be selected with care, is the case where the electron is ionized at one atom and recombines at another far away [67, 68]. Here, the length gauge may result in the unphysical situation of a cutoff harmonic increasing monotonically with the interatomic separation. This means that if the atoms are infinitely far apart, the electron may accumulate an infinitely amount of energy in the continuum, which of cause does not reflect reality. Therefore, we choose to employ the velocity gauge formulation of the SFA-formalism when we, in what follows, derive an expression for the HHG spectrum for extended molecules.

3.3 High-order harmonic generation in extended molecules

3.3.1 Multicenter wavefunction

From now on we let the initial state be a multicenter wavefunction distributed on a two-dimensional grid,

$$\psi_\mathrm{b}(\mathbf{r},t) = \frac{1}{\sqrt{N}}\sum_j \phi(\mathbf{r}_j)\mathrm{e}^{-\mathrm{i}\varepsilon_0 t}. \tag{3.16}$$

Here, the site specific functions are p_z Gaussian-type orbitals (GTOs) centered at $\mathbf{R}_j$, i.e., $\phi(\mathbf{r}_j) = z\ \mathrm{e}^{-\alpha(\mathbf{r}-\mathbf{R}_j)^2}$, N is the number of atoms in the molecule, and ε_0 is the binding energy. The choice of p_z-orbitals is motivated by the aim to model the carbon allotrope of graphene. Graphene, which is simply a single layer of graphite, was first experimentally realized in 2004 [69]. Its extraordinary physical properties, like superior strength and electronic conductivity, is related to the very strong bindings between the sp^2-orbitals of which it consists. Three of the valence orbitals of the carbon atoms ($2s$, $2p_x$ and $2p_y$) hybridizes into sp^2-orbitals providing the hexagonal structure of the molecule. The last electron, which is not taking part in the hybridization, accounts for the electronic properties of the material, and thus prompts the use of p_z-orbitals in the model. Fig. 3.3 shows a sketch of the p_z-orbitals distributed on the hexagonal "honeycomb" lattice.

Figure 3.3: Artist's impression of graphene exposed to a linearly polarized laser pulse. The graphene layer is modeled by p_z-orbitals distributed on a honeycomb lattice in the xy-plane, and the polarization vector of the laser pulse is tilted with respect to the z-axis. The trajectory illustrates the situation in which the ionized electron recombines with another atom in the lattice. The figure is taken from Paper V.

In the velocity gauge, assuming a multicenter wavefunction, the ionization matrix element of Eq. (3.15) reads

$$d^{\text{ion}}(\mathbf{k},t') = \int \mathrm{d}^3 r\, \mathrm{e}^{-\mathrm{i}\mathbf{k}\cdot\mathbf{r}} \left[-\mathrm{i}\mathbf{A}(t')\cdot\nabla + \frac{\mathbf{A}^2(t')}{2} \right] \frac{1}{\sqrt{N}} \sum_j \phi(\mathbf{r}_j). \tag{3.17}$$

If the laser field is linearly polarized in the xz-plane, Eq. (3.17) becomes, upon substitution of the p_z-GTO,

$$\begin{aligned} d^{\text{ion}}(\mathbf{k},t') \;=\; & \frac{1}{\sqrt{N}} \Big\{ \mathrm{i}2\alpha A_x(t')\, F_1^-(\alpha,k_x) F_0^-(\alpha,k_y) F_1^-(\alpha,k_z) \\ & -\mathrm{i}A_z(t')\, F_0^-(\alpha,k_x) F_0^-(\alpha,k_y) \left[F_0^-(\alpha,k_z) - 2\alpha F_2^-(\alpha,k_z) \right] \\ & + \frac{\mathbf{A}^2(t')}{2}\, F_0^-(\alpha,k_x) F_0^-(\alpha,k_y) F_1^-(\alpha,k_z) \Big\} \sum_j \exp\left(-\mathrm{i}\mathbf{k}\cdot\mathbf{R}_j\right), \end{aligned} \tag{3.18}$$

where the integrals over products of GTOs and plane waves are analytic functions [70] found from the formula,

$$\begin{aligned} F_n^{\pm}(a,u) &= \int_{-\infty}^{\infty} \mathrm{d}v \; v^n \mathrm{e}^{-av^2} \mathrm{e}^{\pm \mathrm{i}uv} \\ &= (\pm\mathrm{i})^n \sqrt{\frac{\pi}{a}} \frac{n!}{2^n a^{n/2}} \mathrm{e}^{-u^2/4a} \sum_{k=0}^{[n/2]} \frac{(-1)^k}{k!(n-2k)!} \left(\frac{u}{\sqrt{a}}\right)^{n-2k}. \end{aligned} \tag{3.19}$$

Similarly, the recombination matrix element becomes

$$\begin{aligned} \mathbf{v}^{\mathrm{rec}}(\mathbf{k},t) &= \frac{1}{\sqrt{N}} \int \mathrm{d}^3 r \sum_j \phi(\mathbf{r}_j) \nabla \mathrm{e}^{\mathrm{i}\mathbf{k}\cdot\mathbf{r}} \\ &= \frac{\mathrm{i}\mathbf{k}}{\sqrt{N}} F_0^{+}(\alpha,k_x) F_0^{+}(\alpha,k_y) F_1^{+}(\alpha,k_z) \sum_{j'} \exp\left(\mathrm{i}\mathbf{k}\cdot\mathbf{R}_{j'}\right). \end{aligned} \tag{3.20}$$

Although the ionization and recombination elements are very similar, it is worth noting that whereas the first one is a scalar, the second is a vector. Also notice that the nuclear coordinates come into play as extra phase factors at the end of the expressions.

3.3.2 Stationary-phase method

The stationary-phase method, also called the saddle-point method, is a well-suited approximation when solving highly oscillatory integrals like the one appearing in the momentum coordinate in Eq. (3.15). In this approximation the integrals are evaluated by means of the stationary points of the function in the complex exponent, which is assumed to oscillate rapidly,

$$\int_{-\infty}^{\infty} \mathrm{d}x \; f(x) \mathrm{e}^{\mathrm{i}g(x)} \approx \sum_s f(x_s) \sqrt{\frac{2\pi}{\mathrm{i}g''(x_s)}} \mathrm{e}^{\mathrm{i}g(x_s)}. \tag{3.21}$$

The x_s's are the roots of the equation $g'(x) = 0$. Lewenstein *et al.* [71] were the first to apply the stationary-phase method to the single-atom SFA-problem in Eq. (3.15), using the stationary points of the classical action, i.e., the roots of $\nabla_{\mathbf{k}} S(\mathbf{k},t,t') = 0$,

$$\mathbf{k}_s = -\frac{1}{t-t'} \int_{t'}^{t} \mathrm{d}t'' \; \mathbf{A}(t''). \tag{3.22}$$

On the basis of the kinematic momentum of the electron in the continuum, it can be shown that the stationary-phase approximation favors the classical trajectories described by the equation $\mathbf{x}(t'') = \mathbf{k}_s(t''-t') + \int_{t'}^{t''} \mathrm{d}t'' \mathbf{A}(t'')$, where t'' represents the time from when the electron is ejected at t' and until it recombines with the ion at t. Inserting the definition of $\mathbf{k}_s$ it is also straightforwardly shown that $x(t') = x(t) = 0$ as required by the classical three-step model. Interpreted within Feynman's path formulation of quantum mechanics, the selected trajectories are the paths that maximize the classical action.

In the molecular case, consisting of two or more atomic centers, the stationary points given by Eq. (3.22) do not apply. Here the spatial structure gives rise to additional phases depending on the momentum and nuclear coordinates. These phase factors have to be taken into consideration when evaluating the momentum integral in the stationary-phase approximation. As seen from the classical action together with the Eqs. (3.18) and (3.20) the mulicenter stationary-phase condition becomes

$$\nabla_{\mathbf{k}} \left[\mathbf{k} \cdot (\mathbf{R}_j - \mathbf{R}_{j'}) + \frac{1}{2} \int_{t'}^{t} \mathrm{d}t'' \ \left[\mathbf{k} + \mathbf{A}(t'') \right]^2 \right] \Bigg|_{\mathbf{k}=\mathbf{k}_s} = 0, \tag{3.23}$$

with the stationary points

$$\mathbf{k}_s^{(j,j')} = -\frac{1}{t-t'} \left[\mathbf{R}_j - \mathbf{R}_{j'} + \int_{t'}^{t} \mathrm{d}t'' \ \mathbf{A}(t'') \right]. \tag{3.24}$$

Consequently, the dipole velocity reads

$$\begin{aligned} \langle \Psi(t) | \mathbf{p} | \Psi(t) \rangle \ \approx \ & - \left(\frac{1}{2\pi} \right)^3 \int_0^t \mathrm{d}t' \exp \left(\mathrm{i} \left[\varepsilon_0 (t-t') - \frac{1}{2} \int_{t'}^{t} \mathrm{d}t'' \mathbf{A}^2(t'') \right] \right) \\ & \times \left(\frac{2\pi}{\varepsilon + \mathrm{i}(t-t')} \right)^{3/2} \sum_{j,j'} d_j^{\mathrm{ion}} \left(\mathbf{k}_s^{(j,j')}, t' \right) \mathbf{v}_{j'}^{\mathrm{rec}} \left(\mathbf{k}_s^{(j,j')}, t \right) \\ & \times \exp \left(-\mathrm{i} \left[\frac{1}{2} \left(\mathbf{k}_s^{(j,j')} \right)^2 (t-t') + \mathbf{k}_s^{(j,j')} \cdot \int_{t'}^{t} \mathrm{d}t'' \ \mathbf{A}(t'') \right] \right) \\ & + \text{c.c.} \end{aligned} \tag{3.25}$$

where d_j^{ion} and $\mathbf{v}_{j'}^{\mathrm{rec}}$ are the components of Eqs. (3.18) and (3.20), respectively. The ε appearing in the formula is an *ad hoc* parameter preventing the integral from diverging. Though the results depend weakly on its value, it is not decisive for the HHG spectra.

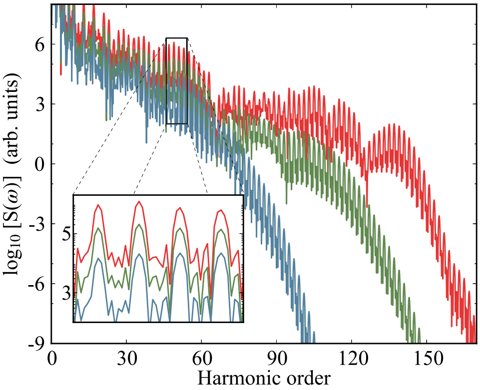

Figure 3.4: The HHG power spectrum as a function of harmonic order for a circular graphene sheet of 348 atoms (lower, blue line), 954 atoms (middle, green line), and 2918 atoms (upper, red line) exposed to a linearly polarized laser. The inset shows a close up of the spectra. The polarization angle of the laser field is $\theta = 45^\circ$. The figure is taken from Paper V.

CHAPTER 4

MULTIPHOTON IONIZATION AND ATOMIC STABILIZATION

4.1 Atoms in superintense laser fields

4.1.1 Atomic stabilization

Our intuition tells us that the more force we apply the more response we get. This was for years the reasoning behind the ionization process of atoms subjected to laser pulses. Lowest-order perturbation theory (LOPT), supports this idea stating that the ionization probability scales like I^n, where I is the intensity and n is the number of photons involved. Though LOPT is not, in any respect, the whole truth, it was with surprise one observed higher order methods to yield a non-monotonically increasing ionization probability. In practise this means that at a certain electric field strength of the applied laser pulse, the atom enters a regime where it is less prone to ionize, i.e., it stabilizes. Since there are several methods and definitions associated with the term "stabilization" it should be stressed that in this thesis the term is used concordant with what is in [72] referred to as *dynamic stabilization*. That is, we solve the time-dependent Schrödinger equation (TDSE), and observe the ionization probability to either level off below unity, or even, locally or globally decrease as a function of the laser intensity. A simplified stabilization curve is displayed in Fig. 4.1.

To get an intuitive grip on the stabilization phenomenon, one can imagine a classical electron bound to an atom, but whose motion is mainly governed by a superintense laser field. If the electric field is strong enough, the excursion amplitude of the electron is approximately given by the quiver amplitude $\alpha_0 = E_0/\omega_0^2$, where E_0 is the field strength and ω_0 is the central frequency of the laser pulse. As the electric field increases the excursion amplitude grows larger, and as a consequence, the electron spends on average more time away from the nucleus. As interaction with the nucleus is a prerequisite for ionization in this regime, the ionization process becomes less likely.

4.1.2 Above threshold ionization

In the limit of strong fields one may observe so-called *above threshold ionization (ATI)*, a phenomenon reminiscent of the high-order harmonic generation discussed in Sec. 3.2. Instead of photons as in HHG, electrons are ejected at energies being multiples of the frequency of the driving laser field, according to the formula

$$E_s = (n+s)\omega - I_\mathrm{p}. \tag{4.1}$$

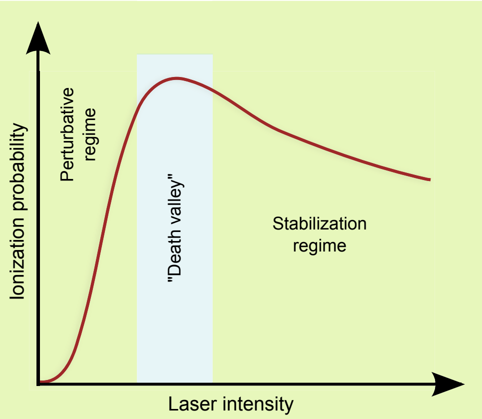

Figure 4.1: The figure illustrates the phenomenon of atomic stabilization. The ionization probability as a function of laser intensity (or field strength) is divided into three regimes. The perturbation regime where the ionization probability scales with intensity like I^n, the "death valley"[1] where the stabilization effect sets in, and the stabilization region where the probability is either constant or decreasing.

In this expression, n is the minimum number of photons needed to exceed the ionization threshold, s is the number of excess photons absorbed by the ejected electron, and I_p is the ionization potential. It is apparent from Eq. (4.1) that the ATI appears as equally spaced peaks in the energy spectrum relative to the ionization potential.

4.1.3 Method

There are two stabilization studies included in the thesis. The overall methodology is basically the same in both, but the physical systems and viewpoint differ. The TDSE is solved in full dimensionality for either one single electron in hydrogen, with the Hamiltonian

$$H = \frac{\mathbf{p}^2}{2} - \frac{1}{r} + \mathbf{A}(t)\cdot\mathbf{p} \tag{4.2}$$

or two interacting electrons in helium, with

$$H = \sum_{i=1}^{2}\left(\frac{\mathbf{p}_i^2}{2} - \frac{2}{r_i} + \mathbf{A}(t)\cdot\mathbf{p}_i\right) + \frac{1}{|\mathbf{r}_1 - \mathbf{r}_2|}. \tag{4.3}$$

In both cases the laser-matter interaction is represented in the velocity gauge. Propagation and analysis of the wavefunction is performed in the Pyprop framework [73], which is a Python/C++ software package for solving the TDSE.

In Pyprop the radial coordinates of the wavefunction are expanded in a B-spline basis [74], while the angular rank is represented in coupled spherical harmonics. In the two-electron case the full wavefunction expansion reads

$$\Psi(\mathbf{r}_1,\mathbf{r}_2,t) = \sum_{i,j,k} c_{ijk}\frac{B_i(r_1)}{r_1}\frac{B_j(r_2)}{r_2}\mathcal{Y}^{LM}_{l_1,l_2}(\Omega_1,\Omega_2), \tag{4.4}$$

---

[1] The expression originates from studies of the lifetime of ground state hydrogen, where the resulting curves in this regime in fact resembles a valley [49].

where $k = \{L, M, l_1, l_2\}$ is a combined angular index and

$$\mathcal{Y}_{l_1,l_2}^{LM}(\Omega_1, \Omega_2) = \sum_m \langle l_1 l_2 m M - m | LM \rangle \, Y_{l_1}^m(\Omega_1) Y_{l_2}^{M-m}(\Omega_2) \tag{4.5}$$

are the coupled spherical harmonic basis functions. In the one particle case, one of the radial ranks of Eq. (4.4) is disregarded and the coupled spherical harmonics [Eq. (4.5)] reduce to regular spherical harmonics.

The Schrödinger equation is represented in matrix form and the wavefunction is propagated in time using a Crank-Nicolson type of propagator,

$$\left(\mathbf{S} + \frac{\mathrm{i}\Delta t}{2}\mathbf{H}\right) \mathbf{c}(t + \Delta t) = \left(\mathbf{S} - \frac{\mathrm{i}\Delta t}{2}\mathbf{H}\right) \mathbf{c}(t), \tag{4.6}$$

where $\mathbf{H}$ is the Hamilton matrix, $\mathbf{c}(t)$ is the vector containing the expansion coefficients of the wavefunction, and $\mathbf{S}$ is the B-spline overlap matrix resulting from the non-orthogonality of the B-spline basis functions. For a thorough discussion, see [32].

4.1.4 Stabilization in circular Rydberg states of hydrogen

Paper II presents a study of low-lying circular Rydberg states exposed to circularly polarized infrared laser fields. As pointed out in Sec. 2.2 a circular state means a state where the quantum numbers fulfill the requirement that $|m| = l = n - 1$. In Paper II m is chosen to be positive, and for that reason one can, in a classical perspective, imagine the electron to be “orbiting” the nucleus in a counterclockwise fashion. Motivated by this conception the state is exposed to a coplanar field that is either co- or counter-rotating with respect to the electron motion. The laser pulse is represented by the vector potential

$$\mathbf{A}(t) = A_0 \sin^2\left(\frac{\pi t}{T}\right) \left[\sin(\omega t + \phi_x)\hat{\mathbf{x}} + \sin(\omega t + \phi_y)\hat{\mathbf{y}}\right], \tag{4.7}$$

where $A_0 = E_0/\omega$, E_0 is the peak amplitude of the electric field, ω is the laser frequency and T is the total pulse duration. As seen from above, the field is defined to rotate clockwise if $\phi_x = 0$ and $\phi_y = \pi/2$ and counterclockwise if the phases are interchanged.

It turns out that stabilization also occurs in purely classical calculations when solving the Newtonian equations of motion for a large number of initial conditions picked at random from a microcanonical ensemble. In this method, knows as classical trajectory Monte Carlo (CTMC) [75, 76], trajectories which fulfill the initial constraints all represent electrons that are bound to the nucleus. After the pulse some of the trajectories correspond to free electrons, and the ratio between the number of these to the total number of trajectories gives an estimate of the ionization probability. In this particular case only trajectories conforming to the constraint $(m - 1/2)\hbar < L_z < (m + 1/2)\hbar$, and with energy equal to the quantum mechanical binding energy, are taken into account in order to mimic the circular behavior of the initial state. In this expression m is the angular projection quantum number of the initial state and L_z is the z-component of the angular momentum of the classical orbit.

In Fig. 4.2 the ionization probability is calculated as a function of intensity/excursion amplitude for the initial state $5g$ $(m = 4)$ when subjected to 800 nm $(\omega = 0.057\,\text{a.u.})$ laser pulses of varying pulse duration. In the upper panels the electric field and the electron are co-rotating (clockwise) whereas in the lower panels they are counter-rotating. The TDSE and CTMC calculations are shown in the left and right panels, respectively. Moreover, the shaded functions at the bottom show the radial distributions in the two cases, and the dashed lines mark the radial expectation values. The lighter shaded areas, representing one standard deviation to each side of the expectation value, provide a gauge of the width of the distributions.

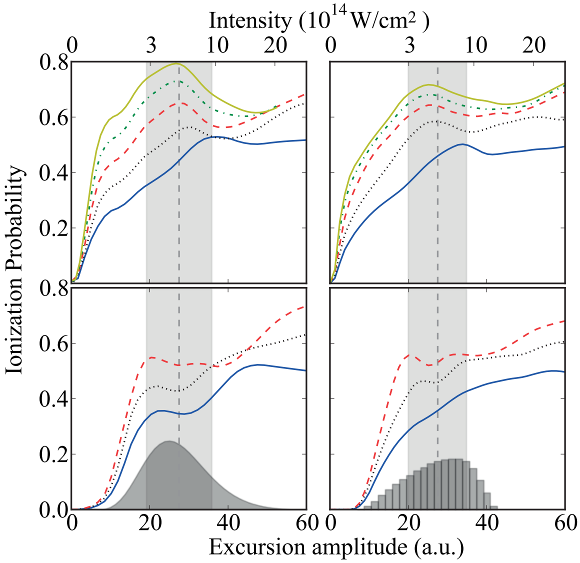

Figure 4.2: Ionization probability as a function of excursion amplitude/laser intensity for the circular $5g$ $(m = 4)$ state. The laser wavelength is 800 nm. The left panels are TDSE results, and the right panels are results from classical trajectory Monte Carlo (CTMC) calculations. For the upper panels a circular field that is co-rotating with respect to the electronic motion was used. The curves, from bottom up, represent laser pulses with 4, 6, 8, 10 and 12 optical cycles. The lower panels are the results for the corresponding counter-rotating case. Here, the curves, from bottom up, represent laser pulses with 4, 6 and 8 optical cycles. The shaded function in the bottom left panel is the shape of the radial probability distribution of the initial (quantum mechanical) state, and the histogram in the bottom right panel represents the distribution of initial radii for the electrons in the CTMC simulations. The dashed lines mark the radial expectation values $\langle r \rangle$, in the two cases, and the lighter shaded areas indicate the widths of the initial probability distributions, here taken to be the standard deviation. The figure is taken from Paper II.

The first thing to notice about Fig. 4.2 is that in all four panels the ionization probability reaches a maximum in the vicinity of the radial expectation value. This close correlation between the torus radius and the excursion amplitude of the electron at the stabilization threshold can be explained in a simple fashion. During the action of the pulse the torus-shaped electron "cloud" is driven around the heavy and nearly stationary nucleus. At a certain field strength the excursion amplitude and the radial expectation value are of comparable magnitudes, and the densest part of the electron "cloud" is pulled through the nucleus. Taken into consideration that interaction between the electron and the nucleus is a catalyst for ionization to take place, it stands to reason that the ionization probability is enhanced at this point. For weaker field strengths the nucleus will stay inside the torus throughout the pulse and the state is consequently less likely to ionize. On the other hand, for field strengths beyond the stabilization threshold the torus is displaced to such a degree that it is no longer “in touch” with the nucleus causing a decline in the ionization probability. However, the large displacement of the torus also implies that the nucleus fails to hold the electron “cloud” together and part of it is flung out and ionizes through dispersion. As a whole, these two mechanisms qualitatively explain the local minima that appear at the largest excursion amplitudes.

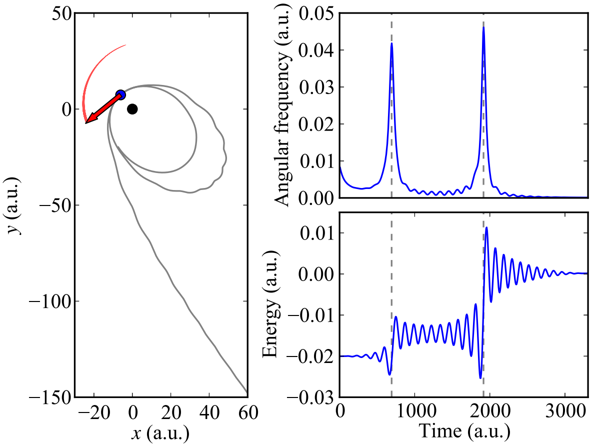

Figure 4.3: Left panel: The trajectory of a classical electron in an elliptical orbit being kicked out when closest to the nucleus (black dot). The red arrow indicates the direction of the force from the field acting on the electron (blue dot) at the very moment when the ionization takes place. Upper right panel: The angular frequency of the electron, relative to the origin, as a function of time. Lower right panel: The energy of the electron as a function of time. The two times the distance between electron and nucleus is minimized are marked by vertical dashed lines in the right panels. The peak intensity is 1.08×10^{11} W cm^{-2}. The figure is taken from Paper II.

One also notices a striking resemblance between the quantum mechanical and classical calculations. Both types of calculations demonstrate a clear difference between the co- and counter-rotating results in the low intensity limit. This observation reflects the classical nature of circular Rydberg states, and can be seen as an example of Bohr’s correspondence principle [13]. Apparently, the mechanism that enhances the ionization probability when the field and electron are co-rotating can be explained classically.

As mentioned, in the CTMC calculations the initial states are modeled by a collection of electron orbits (∼30000) having approximately the same angular momentum, but which are of varying eccentricity. Common to all of them is that the electron is orbiting the nucleus counterclockwise. The electric field which is rotating approximately nine times faster than the electron will, regardless of rotation direction, alternately accelerate and decelerate the electron. This is where the co- and counter-rotation differs. It turns out that the periods of acceleration and deceleration are longer when the field and the electron are co-rotating. Moreover, the better the laser frequency matches the rotational frequency of the electron in the orbit, the longer these periods become. Thus, if the orbit is so that the rotational frequency is instantaneously comparable to the frequency of the laser when the electron is closest to the nucleus, the electron may get an energy boost. An example of such an electron trajectory is shown in the left panel of Fig. 4.3. The figure clearly shows how the electron is simply "kicked out" of the orbit in something like a field assisted "sling-shot maneuver". To underpin this argument the upper and lower right panels display the electron's instantaneous angular frequency and energy. It is seen that the angular frequency indeed approaches the laser frequency $\omega_0 = 0.057\,\mathrm{a.u.}$ two times during the trajectory, and both times the particle experiences a sudden leap in energy.

4.1.5 Stabilization and multiphoton ionization in helium

In Paper I ground state helium is exposed to a linearly polarized extreme ultraviolet (or soft x-ray)[2] laser pulse in the z-direction. The pulse is modeled by the vector potential

$$\mathbf{A}(t) = A_0 \sin^2\left(\frac{\pi t}{T}\right)\cos(\omega t)\hat{\mathbf{z}}, \tag{4.8}$$

where the parameters are as described in Eq. (4.7).

To gauge the importance of the electron-electron interaction on the stabilization phenomenon we also introduce an independent electron (IE) model defined by

$$\Psi(\mathbf{r}_1,\mathbf{r}_2,t) = \psi_{\mathrm{SAE}}(\mathbf{r}_1,t)\psi_{\mathrm{He}^+}(\mathbf{r}_2,t). \tag{4.9}$$

In this simplified model one identifies an "outer" and an "inner" electron in the helium atom. The "outer" electron is represented by a single active electron (SAE) wavefunction which experiences a screened nuclear potential [77] due to the "inner" electron. The "inner" electron, on the other hand, is modeled by a helium ion wavefunction completely disregarding the other electron in the atom. The effect of the electron-electron correlation is neglected everywhere but in the screened potential where it enters indirectly.

Figure 4.4 shows the total (single + double) ionization probability versus excursion amplitude for three different laser frequencies, $\omega = 4$ (left panel), 5 (middle panel), and 10 a.u. (right panel), and for four different pulse durations, 3, 6, 12, and 24 optical cycles (from bottom to top). In the majority of the considered cases the ionization probability increases with the excursion amplitude until it reaches a maximum where the stabilization sets in. One striking feature of this figure is that the independent electron calculations (dashed lines) coincide with the full TDSE calculations (solid lines) for weak fields and long pulses, but otherwise tend to overestimate the stabilization effect.

Intuitively one might expect the role of the electron-electron correlation to become less important in the strong field limit, but Fig. 4.4 demonstrates quite the opposite. This seemingly counterintuitive phenomenon can be understood within the so-called

---

[2] Extreme ultraviolet is typically defined as electromagnetic waves with wavelengths in the range $1-100\,\mathrm{nm}$ or energy $1240-12.5\,\mathrm{eV}$ ($45.6-0.46\,\mathrm{a.u.}$), but the boundaries are vague. For instance, the laser frequencies in Fig. 4.4, $\omega = 4$, 5 and 6 a.u., translate into 10.1, 9.1 and 8 nm, respectively.

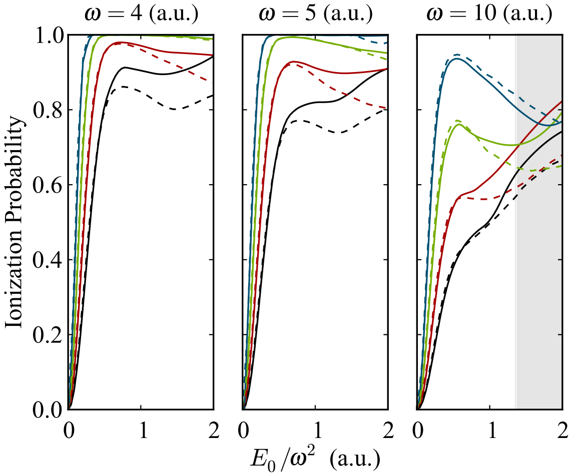

Figure 4.4: Ionization probabilities plotted as a functions of the electronic displacement (E_0/ω^2) for the frequencies $\omega = 4$ (left panel), $\omega = 5$ (middle panel), and $\omega = 10$ a.u. (right panel). In each panel, the pulses are of 3, 6, 12, and 24 cycles duration from bottom to top. The solid lines are the results from the full calculations. The dashed lines are the results from the IE calculations. In the right panel, the excursion amplitude extends into a region (shaded) where relativistic (nondipole) effects may have an influence on the results, and the corresponding velocity of a classical free electron moving in the field exceeds 10% of the speed of light. The figure is taken from Paper I.

Kramers-Henneberger frame. This is the rest frame of a classical free electron in the laser field with the Hamiltonian

$$H_{\mathrm{KH}} = \sum_{i=1}^{2} \left(\frac{\mathbf{p}_i^2}{2} - \frac{2}{|\mathbf{r}_i + \boldsymbol{\alpha}(t)|} \right) + \frac{1}{|\mathbf{r}_1 - \mathbf{r}_2|}, \tag{4.10}$$

where

$$\boldsymbol{\alpha}(t) = \int_0^t A_z(t')\mathrm{d}t'\hat{\mathbf{z}}, \tag{4.11}$$

represents the displacement of the classical electron with respect to the laboratory frame. The second term in Eq. (4.10), the Kramers-Henneberger potential, might as well be expanded in a Fourier series

$$V_{\mathrm{KH}}[\mathbf{r}_i + \boldsymbol{\alpha}(t)] = -\frac{2}{|\mathbf{r}_i + \boldsymbol{\alpha}(t)|} = \sum_n V_n(\alpha_0, \mathbf{r}_i)\mathrm{e}^{-\mathrm{i}n\omega t} \tag{4.12}$$

with the Fourier amplitudes

$$V_n(\alpha_0, \mathbf{r}_i) = \frac{1}{T}\int_0^T \mathrm{e}^{-\mathrm{i}n\omega t} V_{\mathrm{KH}}[\mathbf{r}_i + \boldsymbol{\alpha}(t)]\mathrm{d}t. \tag{4.13}$$

Especially notice that in this frame the laser-interaction enters into the electron-nucleus interaction term which consequently becomes time-dependent.

By solving the TDSE using high-frequency Floquet theory Gavrila *et al.* [72, 78–80] showed that the first Fourier amplitude ($n = 0$) is more important the higher the values of the excursion amplitude (α_0) become. Moreover, Førre *et al.* [81] showed that in the limit of superintense fields the ionization dynamics of hydrogen is mainly governed by the V_0 potential. These results motivate an effective Hamiltonian for the system in the superintense regime,

$$\widetilde{H}_{\mathrm{KH}} = \sum_{i=1}^{2} \left(\frac{\mathbf{p}_i^2}{2} + V_0(\alpha_0, \mathbf{r}_i) \right) + \frac{1}{|\mathbf{r}_1 - \mathbf{r}_2|}. \tag{4.14}$$

It turns out that in the limit where α_0 approaches infinity the V_0-potential is negligible relative to the electron-electron repulsion term given that $\langle r_1 \rangle \ll \alpha_0$ and $\langle r_2 \rangle \ll \alpha_0$. This means that for superintense fields and short pulses the dynamics of the system is basically that of a Coulomb explosion trigged by the electron-electron repulsion. Alternatively, in the laboratory frame, the two electrons in helium can be considered as almost free particles moving side by side in the superintense field. At some excursion amplitude the Coulomb potential can be neglected and the atom ionizes in an electron-electron scattering event. These considerations clearly demonstrate that the electron-electron correlation in fact plays an important role even in the strong field limit.

Figure 4.5 displays the double-ionization energy distribution for three different field strengths, 1, 10 and 20 a.u., in the case of a six-cycle pulse of frequency 5 a.u. In the upper panel, with the lowest field strength, the spectrum is dominated by the one-photon “ridge”. It stretches between the two extremities where only one of the electrons escapes with all the excess energy[3]. For the intermediate field strength two- and three-photon double-electron above threshold ionization (DATI) peaks become visible along the second and the third auxiliary line. The highly correlated one-photon process, on the other hand, fades away and is almost negligible at the highest field strength where exchange of energy between the electrons becomes less probable.

The importance of the electron-electron correlation can also be seen in the energy distributions. Usually the process of two-photon DATI appears as a double peak structure resulting from a sequential ionization process. For ultrashort pulses the second photon is absorbed before the residual ion has time to relax to the ground state and consequently the process appears as a single peak centered at equal energy sharing. The merge of the two-photon peaks in the short pulse limit has been thoroughly studied in the weak field limit. Here it is demonstrated that the phenomenon is also present in the superintense field regime, which once again points to the inadequacy of the independent electron picture.

4.2 Two-photon double ionization of H_2

Using the same numerical framework (Pyprop) as in the two previously mentioned papers, we have also studied the process of two-photon double ionization (TPDI) taking place in the hydrogen molecule when exposed to intense laser pulses.

The TPDI process in H_2 may happen in two ways: sequentially or directly (non-sequentially). Initially the system wavefunction is assumed to be in the H_2 ground

---

[3] The binding energy of helium is 2.9 a.u., and consequently the excess energy is 2.1 a.u.

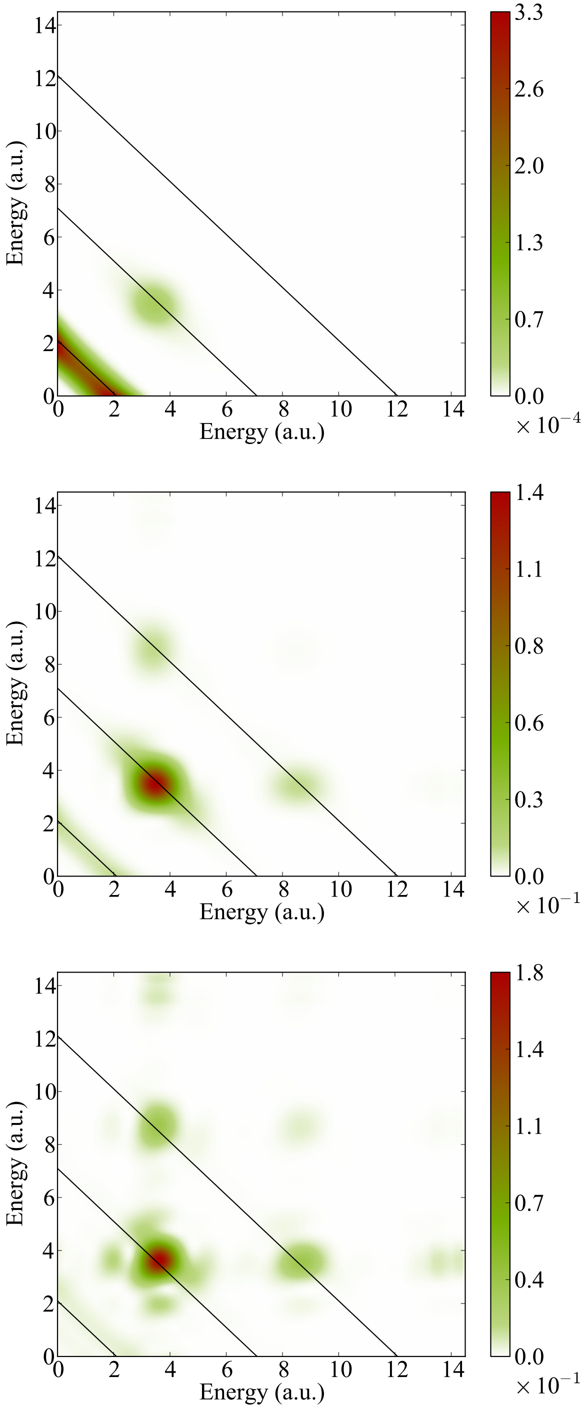

Figure 4.5: Double-ionization energy distribution for an $\omega = 5$ a.u. six-cycle pulse (182 as), and for field strengths of 1 (upper panel), 10 (middle panel), and 20 a.u. (lower panel). The figure is taken from Paper I.

state. In the sequential process, the first photon strikes; one electron is captured into the H_2^+ ground state, while the other is liberated with an energy equal to the energy difference

$$E = E_{\text{photon}} - (E_{H_2^+} - E_{H_2}). \tag{4.15}$$

Subsequently, a second photon ionizes the electron that is still bound. In the direct ionization process, however, the two electrons are launched to the continuum simultaneously by two photons. When the photon energy of the incident laser pulse is less than the binding energy of H_2^+, but larger than half the binding energy of H_2, i.e.,

$$25.6\,\text{eV} \leq E_{\text{photon}} \leq 34.8\,\text{eV}, \tag{4.16}$$

only the direct process is energetically accessible. An illustration of the two ionization schemes is shown in Fig. 4.6.

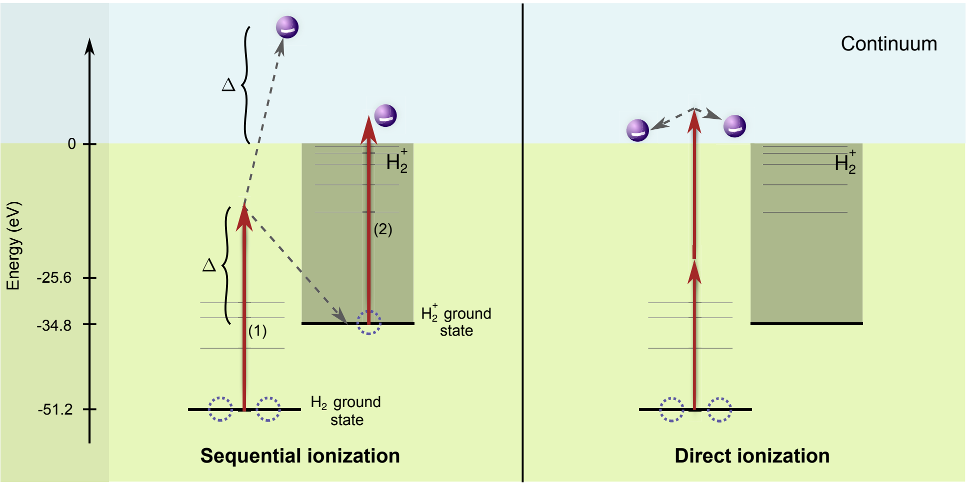

Figure 4.6: An illustration of the sequential (left panel) and the direct (right panel) ionization process in H_2. The blue balls represents the electrons and the red arrows the photons. The dashed arrows show how the electrons share the energy. The states to the left of each panel are the states of H_2 and the ones to the right are those of H_2^+.

By assuming the velocity gauge and the fixed-nuclei approximation the Hamiltonian for molecular hydrogen interacting with a laser field becomes

$$H = \sum_{i=1}^{2} \left(\frac{\mathbf{p}_i^2}{2} - \frac{1}{|\mathbf{r}_i + \mathbf{R}/2|} - \frac{1}{|\mathbf{r}_i - \mathbf{R}/2|} + \mathbf{A}(t) \cdot \mathbf{p}_i \right) + \frac{1}{|\mathbf{r}_1 - \mathbf{r}_2|} \tag{4.17}$$

The distance between the two nuclei is fixed at the equilibrium internuclear distance $R = 1.4\,\text{a.u.}$ of the molecule. This approximation can be justified by the fact that the electrons are ejected almost simultaneously in the direct TPDI process, and move apart much faster than the Coulomb exploding nuclei. From this it follows, taking into account the time separation between the two photons, that the approximation is not necessarily valid when studying the sequential ionization process. Nevertheless, the fixed nuclear approximation has been applied in studies of the sequential process utilizing ultrashort (attosecond) pulses [82].

In Paper III we calculate the total (generalized) and the single-differential cross section in the direct ionization regime [cf. Eq. (4.16)] using a 15-cycle linearly polarized laser pulse. We consider both parallel and perpendicular orientation of the polarization vector with respect to the internuclear axis. The use of cross sections rather than ionization probabilities enables the results obtained with different pulses to be compared, given that the pulses are not too short. The generalized cross section is found from the expression

$$\sigma = \left(\frac{\omega}{I}\right)^2 \frac{P_{\text{ion}}}{T_{\text{eff}}}, \tag{4.18}$$

where P_{ion} is the double ionization probability, ω and I are the frequency and peak intensity of the laser, and T_{eff} is the effective pulse duration. The latter is, in the case of a $\sin^2$-shaped laser pulse, given by $\frac{35}{128}T$ [28], with T being the pulse duration.

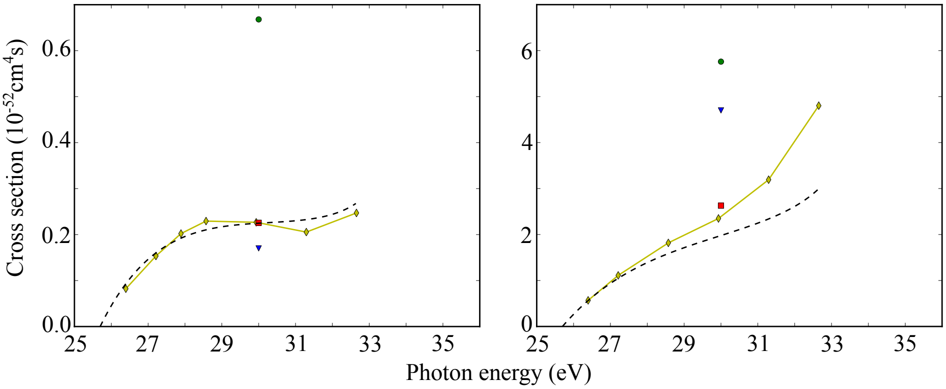

Figure 4.7: The total (generalized) cross section for the process of direct two-photon double ionization of H_2. The molecule is oriented parallel and perpendicular to the laser polarization axis in the left and the right panel, respectively. Yellow line with diamonds: *ab initio* result. Dashed line: model results. Blue triangle: theoretical result of Colgan *et al.* [33]. Green circle: theoretical result of Morales *et al.* [34]. Red square: theoretical result of Guan *et al.* [36]. The figure is taken from Paper III.

CHAPTER 5

INTRODUCTION TO THE PAPERS

This chapter provides a short introduction to the papers included in the dissertation. It should be emphasized that all papers are the product of collaboration and open discussions among all the authors.

Paper I: *Multiphoton ionization and stabilization of helium in superintense xuv fields*

In this paper we focus on the process of multiphoton ionization of ground state helium. The helium atom is exposed to short extreme ultraviolet laser pulses of intensity high enough for the ionization to enter the stabilization regime. The study investigates in particular the role of the electron-electron interaction on the ionization dynamics, and demonstrates that calculations where this mechanism is neglected tend to overestimate the stabilization effect. To this end, two different approaches are taken. First and foremost, the Schrödinger equation is solved in full dimensionality for two interacting electrons. In addition, an independent electron model is introduced based on products of single-electron wavefunctions. The inadequacy of the independent electron picture is underpinned by an explanation in which the system is seen from the Kramers-Henneberger frame. We argue that for sufficiently short pulses in the limit of superintense fields the dynamics of the two-electron system reduces to that of a Coulomb explosion.

I have performed a substantial portion of both the *ab initio* calculations and the single-electron calculations used as input in the independent electron model. I was involved in the writing of the paper, especially the part concerning stabilization, and made some of the figures.

Paper II: *Stabilization of circular Rydberg atoms by circularly polarized infrared laser fields*

We revisit the phenomenon of atomic stabilization but in a different system. Low-lying circular Rydberg states of hydrogen are subjected to circularly polarized infrared laser fields. The near classical nature of circular Rydberg states motivates a conception where the electron is orbiting the nucleus in a clockwise fashion given that $m > 0$. We show that in the low-intensity limit the ionization probability depends critically on whether the electron and field polarization vector are co- or counter-rotating. Furthermore, it is observed that the ionization probability reaches a maximum (and stabilization sets in) at an intensity which is related to the radius of the electron "cloud". In addition to the main approach, which is solving the Schrödinger equation *ab initio*, we also perform classical trajectory calculations to further elucidate the problem. The classical calculations are shown to qualitatively coincide with the quantum mechanical results. The former approach is therefore used when explaining why the ionization is enhanced when the field and the electron are co-rotating.

I have implemented the velocity gauge laser-matter interaction for circularly polarized pulses in our computer code, and ran the majority of the quantum mechanical calculations. I contributed to the writing of the paper, with emphasize on the method section, and made the figures except of figure 4.

Paper III: *Direct two-photon double ionization of* H_2

In this paper we calculate the total (generalized) and the single-differential cross section in the direct ionization regime using a 15-cycle linearly polarized laser pulse. We consider both parallel and perpendicular orientation of the polarization vector with respect to the internuclear axis. The results are compared to previous theoretical studies perform by other research groups as well as a simple approximate model.

For this paper I have prepared and implemented the diatomic potential and the perpendicular laser-matter interaction for our numerical framework. I have also contributed to the writing of the paper, especially the theory section.

Paper IV: *Femtosecond-pulse-train ionization of Rydberg wave packets*

A Rydberg wave packet is formed within the Stark split $n = 16$ shell in hydrogen. Transitions between the states are induced by a resonant rotating microwave field, and the wave packet is repeatedly driven between the circular state and the linear state. As the wave packet slowly makes its way back and forth between the two extremities, it is hit by a train of femtosecond pulses. We study how the total and the angular resolved ionization probability varies with the number of pulses in the sequence and the time separation between them. Since the microwave field and the pulse-train act on completely different time scales, the computational scheme is two-fold. Whereas the dynamics of the wave packet is computed by propagating the time-dependent Schrödinger equation the femtosecond pulses are modeled by use of perturbation theory, considering the wave packet to be frozen.

For this paper I have developed the theory and the computer code used in the calculations in close collaboration with the first author. I also contributed to all sections of the paper in the writing process and in the making of the figures.

Paper V: *High-order harmonic generation from graphene: Strong attosecond pulses with arbitrary polarization*

We present a numerical simulation of high-order harmonic generation (HHG) from a graphene sheet. Graphene is a two-dimensional monolayer of carbon atoms arranged in a hexagonal pattern. It was first experimentally realized in 2004, though it has been studied theoretically for decades. HHG from molecules allows for the electron to recombine with a nucleus different from the one that it was originally ionized from. Consequently, higher cutoff harmonics are observed in molecular systems as compared to atoms. Two different scenarios are considered. Either the graphene sheet is exposed to a linearly polarized laser pulse tilted with respect to the z-axis, or it is subjected to a pulse which is circularly polarized in the xy-plane. The paper demonstrates how the cutoff harmonic changes with the number of atoms in the graphene sample and the polarization angle. Moreover, it is shown that the HHG-spectrum resulting from the circularly polarized pulses exhibits an interesting twin-peak structure.

I have derived the theory and developed the computer codes in collaboration with the co-authors. I performed about half the calculations, contributed to all sections of the paper in the writing process, and made some of the figures.

CHAPTER 6

SUMMARY AND OUTLOOK

The aim of this thesis has been to investigate the ionization dynamics of atoms and molecules exposed to few-cycle laser pulses, encompassing systems that are within experimental reach and beyond. To this end, five studies have been conducted, addressing several topics within the field of atomic, molecular and optical sciences. The laser-matter interaction has been scrutinized both perturbatively and non-perturbatively in scenarios where the laser field strength varies from weak to super-strong. Different regimes require different approaches; in the present work the time-dependent Schrödinger equation has been solved both using approximative methods as well as from first principles.

In the perturbative regime we have studied Rydberg atoms – atomic systems existing on the borderline between classical physics and quantum mechanics. We have shown that the angular resolved ionization probability of an n-shell Rydberg wave packet exposed to a train of weak femtosecond pulses is intimately related to the number of times the pulse-train strikes. One can envision that this knowledge can come useful in experiments reconstructing the image of the exotic Rydberg states based on the angular distributions.

Imaging is also one of the proposed applications of high-order harmonic generation. Our results suggest that utilizing graphene as the target medium is an efficient way to realize large cutoff harmonics, that graphene may serve as a source of selective harmonic generation, and that it can potentially become important in the generation of complex attosecond pulses. There are other forms of carbon which share many of the properties of graphene. One possible extension of this project could be high-order harmonic generation from allotropes like carbon nanotubes and fullerenes.

Results on atomic stabilization have been presented – a topic where the theoretical treatment has been the driving force. After more than 20 years of research, studies showing experimental verification are virtually absent. This makes the pursuit of theoretical results even more important, especially in the limit of superintense laser pulses. In this regime we have demonstrated the correlation between the electrons to have a detrimental effect on the stabilization process. Moving to a different system, stabilization in low-lying circular Rydberg states is within experimental reach. Using the parameters of conventional Ti:sapphire lasers we have shown that the ionization probability strongly depends on the rotation direction of the circularly polarized laser pulses. A continuation of these studies could be stabilization in simple molecules, for instance H_2, where the orientation of the nuclear axis with respect to the laser polarization is an interesting aspect.

Correlation is also a keyword in the process of direct two-photon double ionization of molecular hydrogen. This is a research domain where both the theoretical and the experimental results are scarce, and where every new contribution provides valuable insight. The process is difficult to measure in experiments and theoretical calculations are quite demanding. As with the atomic stabilization we have solved the system *ab initio*, but have had to restrict ourselves to a model where the nuclear axis is fixed. A step further could therefore be to also incorporate the nuclear motion in the computations like Martín *et al.* [83] did for the corresponding one-photon process, and hopefully, the future will bring experimental results on this process where much is still to be discovered.

CHAPTER 7

SCIENTIFIC RESULTS

PAPER I

Multiphoton ionization and stabilization of helium in superintense xuv fields

S. A. Sørngård, S. Askeland, R. Nepstad and M. Førre

Physical Review A, **83**, 033414 (2011)

PHYSICAL REVIEW A **83**, 033414 (2011)

Multiphoton ionization and stabilization of helium in superintense xuv fields

S. A. Sørngård, S. Askeland, R. Nepstad, and M. Førre
Department of Physics and Technology, University of Bergen, N-5007 Bergen, Norway

(Received 19 January 2011; published 21 March 2011)

Multiphoton ionization of helium is investigated in the superintense field regime, with particular emphasis on the role of the electron-electron interaction in the ionization and stabilization dynamics. To accomplish this, we solve *ab initio* the time-dependent Schrödinger equation with the full electron-electron interaction included. By comparing the ionization yields obtained from the full calculations with the corresponding results of an independent-electron model, we come to the somewhat counterintuitive conclusion that the single-particle picture breaks down at superstrong field strengths. We explain this finding from the perspective of the so-called Kramers-Henneberger frame, the reference frame of a free (classical) electron moving in the field. The breakdown is tied to the fact that *shake-up* and *shake-off* processes cannot be properly accounted for in commonly used independent-electron models. In addition, we see evidence of a change from the multiphoton to the shake-off ionization regime in the energy distributions of the electrons. From the angular distribution, it is apparent that the correlation is an important factor even in this regime.

DOI: 10.1103/PhysRevA.83.033414 PACS number(s): 32.80.Fb, 32.80.Rm

I. INTRODUCTION

More than 20 years ago, theoretical studies of atomic hydrogen in ultraintense, high-frequency laser fields produced an unexpected result [1–9]: When increasing the intensity of the laser pulse to such a degree that the applied forces dominate over the Coulomb attraction between the nucleus and the electron, the ionization probability does not increase accordingly but rather stabilizes or starts subsiding. This counterintuitive phenomenon was dubbed atomic stabilization and was subject to much research in the following decade. The discussions, controversies, and conclusions are available in a number of review articles. (See, e.g., [10–12] and references therein.) It has also been pointed out that atomic stabilization has a classical counterpart [13,14]. (See also [10] and references therein.)

At the start of the 1990s, the laser technology required to experimentally observe the stabilization effect in tightly bound systems was not available. For example, in order to measure the stabilization in atomic hydrogen, photon energies exceeding 13.6 eV, the binding energy of the atom, and intensities on the order of 10^{16} W/cm^2 or more are required [15,16]. Grobe and Eberly [17] demonstrated that stabilization could occur in H$^-$ at moderate intensities ($\sim 10^{13}$ W/cm^2) and photon energies ($\sim$2 eV), and Wei *et al.* [18] suggested an experiment in which a laser, of realistic frequency and intensity, could possibly stabilize the unstable He$^-$ ion. However, at present, the only experimental confirmations of stabilization are from studies of low-lying Rydberg states [19–22]. With recent advances in free-electron laser (FEL) technology, extremely high peak intensities have been achieved, with wavelengths ranging from vacuum ultraviolet to soft x rays [23,24], and even higher intensities are expected to be delivered in the near future [25]. Thus, laser technology is approaching the regime needed for observing atomic stabilization in ground-state (neutral) atomic systems.

Although atomic stabilization has been studied extensively during the last two decades, studies of stabilization in systems containing two electrons are still scarce [10,26], and most often assessed with simplified physical models of reduced dimensionality. A study on stabilization in a model two-electron xenon atom revealed that both the single- and double-ionization channels may be subjected to stabilization [27,28]. However, it has also been pointed out that the electron-electron interaction suppresses atomic stabilization [17,29–31]. Including a second electron adds a new dimension to the problem, manifested through the electronic repulsion. Although *ab initio* calculations of helium have previously been performed at fairly high intensities in the extreme ultraviolet (xuv) regime [32,33], only recently were such endeavors extended into the stabilization regime [34], confirming the detrimental effect of the electron-electron interaction on stabilization. However, it was shown that the effect is markedly less than predicted in models of reduced dimensionality.

In this paper, we revisit the problem of the multiphoton ionization of helium in superintense, high-frequency fields. In continuation of the work of Birkeland *et al.* [34], we look more closely into the strong-field-ionization dynamics of the atom, with particular emphasis on atomic stabilization, considering laser pulses of various central frequencies and durations. A comparison of the ionization yields obtained from the *ab initio* calculations, including correlations, with corresponding results obtained from an independent-electron model reveals that the validity of the latter breaks down at strong fields. An analysis of the system equations in the so-called Kramers-Henneberger frame [35–38] shows that the electron-electron interaction plays a decisive role in this limit. We further show that this is manifested in the energy and angular distributions of the ejected electrons.

Atomic units, where m_e, $\hbar$, and e are scaled to unity, are used throughout unless stated otherwise.

II. METHODS

A. *Ab initio* calculations

We obtain the ionization probability of ground-state helium in extreme laser fields from first principles, i.e., by solving (numerically) the full time-dependent Schrödinger equation (TDSE). Formulating the problem in the velocity gauge, the

©2011 American Physical Society

Hamiltonian assumes the form

$$H = \sum_{i=1}^{2} \left(\frac{\mathbf{p}_i^2}{2} - \frac{2}{r_i} + A_z(t) p_{z_i} \right) + \frac{1}{|\mathbf{r}_1 - \mathbf{r}_2|}. \tag{1}$$

A sine-squared carrier envelope was chosen for the laser interaction:

$$A_z(t) = A_0 \sin^2 \left(\frac{\pi t}{T} \right) \cos(\omega t), \tag{2}$$

where $A_0 = E_0/\omega$, E_0 is the peak amplitude of the electric field, ω is the laser frequency, and T is the total pulse duration. The semiclassical treatment of the field is a valid approach due to the enormous photon flux of superintense lasers.

The pulse fulfills the constraint of a physical pulse [39]:

$$\int_0^T \mathbf{E}(t) dt = 0. \tag{3}$$

Propagation and analysis of the wave function is performed with the PYPROP framework [40], a PYTHON/C++ software package for solving the TDSE.

The wave function is expanded in a B-spline basis [41,42] for each of the radial components, and a coupled spherical harmonic basis for the angular components,

$$\Psi(\mathbf{r}_1,\mathbf{r}_2,t) = \sum_{i,j,k} c_{ijk} \frac{B_i(r_1)}{r_1} \frac{B_j(r_2)}{r_2} \mathcal{Y}_{l_1,l_2}^{LM}(\Omega_1,\Omega_2), \tag{4}$$

where $k = \{L,M,l_1,l_2\}$ is a combined index for the angular indices. The coupled spherical harmonic basis functions

$$\mathcal{Y}_{l_1,l_2}^{LM}(\Omega_1,\Omega_2) = \sum_m \langle l_1 l_2 m M - m | L M \rangle Y_{l_1}^m(\Omega_1) Y_{l_2}^{M-m}(\Omega_2) \tag{5}$$

are obtained by linearly combining products of ordinary spherical harmonics, weighted by Clebsch-Gordan coefficients [43].

As the B-spline basis functions are not orthogonal, an overlap matrix $S_{ij} = \int B_i(r) B_j(r) dr$ is introduced for each electronic coordinate. From these the total overlap matrix is found for every angular momentum component by taking the Kronecker product $\mathbf{S} = \mathbf{I}_k \otimes \mathbf{S}_1 \otimes \mathbf{S}_2$, where $\mathbf{I}_k$ denotes the identity matrix and k is the angular index. The resulting TDSE may then be written as

$$i \mathbf{S} \frac{\partial}{\partial t} \mathbf{c}(t) = \mathbf{H}(t) \mathbf{c}(t) \tag{6}$$

in matrix form.

We solve the TDSE using a scheme based on the first-order approximation to the matrix exponential

$$\exp(-i \Delta t \mathbf{S}^{-1} \mathbf{H}) = \mathbf{I} - i \Delta t \mathbf{S}^{-1} \mathbf{H} + O(\Delta t^2). \tag{7}$$

A direct application of this formula is not desirable due to numerical instabilities. Instead, we combine one half step forward in time

$$\mathbf{c}(t + \Delta t/2) = \left(\mathbf{I} - \frac{i \Delta t}{2} \mathbf{S}^{-1} \mathbf{H} \right) \mathbf{c}(t), \tag{8}$$

with one half step backward in time

$$\mathbf{c}(t + \Delta t/2) = \left(\mathbf{I} + \frac{i \Delta t}{2} \mathbf{S}^{-1} \mathbf{H} \right) \mathbf{c}(t + \Delta t), \tag{9}$$

to obtain the unconditionally stable Cayley-Hamilton form of the time propagator

$$\left(\mathbf{S} + \frac{i \Delta t}{2} \mathbf{H} \right) \mathbf{c}(t + \Delta t) = \left(\mathbf{S} - \frac{i \Delta t}{2} \mathbf{H} \right) \mathbf{c}(t). \tag{10}$$

This linear system of equations is too large to be solved directly; hence, we use an iterative method. Since the matrix $(\mathbf{S} + \frac{i\Delta t}{2} \mathbf{H})$ is not Hermitian, our choice is the generalized minimum-residual method (GMRES), a Krylov subspace method which combines Arnoldi iterations with a least-squares problem in the projected space [44,45]. In the GMRES algorithm, the error in the least-squares residuals is controlled by the dimension of the Krylov subspace, which can be increased until the desired precision is obtained.

B. Calculating ionization

In this paper, we compute the ionization probability resolved in direction and energy. We also do a series of smaller simulations, calculating only the total-ionization probabilities. Separating the single and double ionization is achieved by a projection onto double continuum states. In order to obtain these continuum states exactly, one needs to solve a scattering problem for the full two-particle system. As this is computationally cumbersome, an approximation using single-particle states is adopted instead. It can be described as follows: In the case of double ionization, when both electrons are far from the nucleus, a product of continuum He^+ $(Z = 2)$ states is used. For single ionization, when one electron is close to the nucleus and the other far away, a product of bound He^+ and continuum H $(Z = 1)$ is used [46].

The single-electron states are not orthogonal to the bound states of the two-electron system, which may become populated during the action of the pulse. Therefore, the projection of the final wave function on the doubly bound states is removed before further analysis is conducted. Moreover, as the electron-electron correlation is neglected in the double continuum states, the system must be propagated after the pulse for all quantities to converge [47].

On the other hand, when only calculating the total ionization, a small radial box is sufficient. It is no longer necessary to propagate the system after the pulse, in order to minimize the interaction term, nor to project onto continuum He^+ states. An absorbing potential is applied at the box boundary in order to absorb the emitted electrons and to minimize reflection. When coupled with an absorbing potential, we find that only about one-third of the radius needed to resolve the differential probabilities is necessary. The total-ionization probability is simply the complement of the probability of being in one of the bound states.

To find the bound states, we use the implicitly restarted Arnoldi method [48]. This is a version of the Arnoldi method for finding eigenpairs that refines the Krylov subspace basis in order to find the wanted eigenvectors and eigenvalues. As the Arnoldi method tends to find the largest eigenvalues, we also use shifted inverse iterations, which let us find the eigenvalues near a given value.

Further details on the discretization, the time integration, and the analysis were presented in a recent paper [49].

C. Independent-electron model

In order to gauge the importance of the electron-electron interaction, we repeat the calculations using an independent-electron (IE) model [50]. The total wave function is approximated as a product of two single-electron wave functions

$$\Psi(\mathbf{r}_1,\mathbf{r}_2) = \psi_{\mathrm{SAE}}(\mathbf{r}_1)\psi_{\mathrm{He}^+}(\mathbf{r}_2). \tag{11}$$

The subscript SAE refers to the single-active electron approximation. This is a common approximation for many-electron problems, which focuses on one electron at a time. Any dependence on the rest of the electrons is included in a common potential that is constant with regard to the other electron positions. To find the first electron wave function ψ_{SAE}, we apply a pseudo potential, which includes the shielding of the nucleus caused by the other electron [51],

$$V(r) = -\frac{Z + a_1 e^{-a_2 r} + a_3 r e^{-a_4 r} + a_5 e^{-a_6 r}}{r}. \tag{12}$$

For helium, the effective charge $Z = 1$ and the coefficients $a_1 = 1.231, a_2 = 0.662, a_3 = 1.325, a_4 = 1.236, a_5 = 0.231$, and $a_6 = 0.480$ were adopted. The other electron moves in a He^+ potential, and it is therefore an accurate model for the singly ionized atom. The IE model reproduces the correct ground-state energies and single- and double-ionization thresholds, and decently represents the excited states. As the name of the model suggests, the electrons do not interact with each other, beyond what is included in the shielded nuclear potential. That makes this a three-dimensional, rather than a six-dimensional problem, and it can be calculated with relative ease on an ordinary computer. As a consequence of working with independent particles, the total- (single + double) ionization probability becomes

$$P^{\mathrm{ion}}_{\mathrm{total}} = 1 - P^{\mathrm{b}}_{\mathrm{SAE}} P^{\mathrm{b}}_{\mathrm{He}^+}, \tag{13}$$

where $P^{\mathrm{b}}_{\mathrm{SAE}}$ and $P^{\mathrm{b}}_{\mathrm{He}^+}$ are the probability of the SAE and the He^+ electron, respectively, being in a bound state. The probability for double ionization is obtained from the product

$$P^{\mathrm{ion}}_{\mathrm{double}} = P^{\mathrm{ion}}_{\mathrm{SAE}} P^{\mathrm{ion}}_{\mathrm{He}^+}, \tag{14}$$

and the single-ionization probability is

$$P^{\mathrm{ion}}_{\mathrm{single}} = P^{\mathrm{b}}_{\mathrm{SAE}} P^{\mathrm{ion}}_{\mathrm{He}^+} + P^{\mathrm{ion}}_{\mathrm{SAE}} P^{\mathrm{b}}_{\mathrm{He}^+}, \tag{15}$$

where $P^{\mathrm{ion}}_{\mathrm{SAE}}$ and $P^{\mathrm{ion}}_{\mathrm{He}^+}$ are the ionization probabilities of the SAE and the He^+ electrons.

D. Convergence of the calculations

When doing the largest calculations, the radial domain typically extends to 80 a.u., although the double of this was employed to test the convergence. A fifth-order B-spline basis of 185 splines is used, distributed exponentially near the nucleus, and linearly further away. Up to 300 splines were used for convergence test purposes. Regarding the angular basis of coupled spherical harmonics, $l \leqslant 5$ and $L \leqslant 6$ were found to be sufficient. Note that the system retains cylindrical symmetry in the presence of the z polarized laser field. Therefore, the M quantum number is set to 0 throughout. Based on the calculations with a larger basis, the error is estimated to be less than 1% in the ionization probabilities.

For the smaller calculations, intended to provide only the total-ionization probability, we use a small radial box of 30 a.u. and 80–100 B splines of order 7, distributed linearly. Note that we have only one-third of the box size but one-half of the number of B splines. In these calculations, the angular basis went up to $l = 7$ and $L = 6$. The small box made it possible to go to higher intensities and pulse lengths than did the large box. The error in the ionization probability is gauged to be less than 5% when $E_0/\omega^2 > 1$ a.u. and less than 2% for lower intensities.

III. RESULTS

A. Ionization probabilities

Figure 1 shows the total- (single + double) ionization probability versus α_0 for three different laser frequencies, $\omega = 4$ (left panel), 5 (middle panel), and 10 a.u. (right panel), and for four different pulse durations, 3, 6, 12, and 24 cycles (from bottom to top). Notice that on the abscissas, the domains are given in $\alpha_0 = E_0/\omega^2$, instead of intensity or peak electric field strength. Here, α_0 represents the displacement amplitude of a free classical electron in the oscillating field [4]. This scaling allows us to easily compare the results obtained with different laser frequencies. In most of the considered cases, the ionization probability increases with α_0 up to some point, where it attains a maximum before it starts to decline, i.e., we are entering the so-called stabilization regime. When stabilization occurs, the ionization peak (corresponding to the "death valley" [10]) is typically situated between $\alpha_0 = 0.6$ and

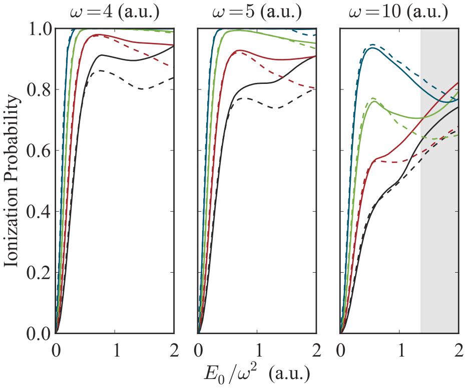

FIG. 1. (Color online) Ionization probabilities plotted as functions of the electronic displacement (E_0/ω^2) for the frequencies $\omega = 4$ (left panel), $\omega = 5$ (middle panel), and $\omega = 10$ a.u. (right panel). In each panel, the pulses are of 3, 6, 12, and 24 cycles duration from bottom to top. The solid lines are the results from the full calculations. The dashed lines are the results from the IE calculations. In the right panel, the displacement (α_0) extends into a region (shaded) where relativistic (nondipole) effects may have an influence on the results [15,30,31,52], and the corresponding velocity of a classical free electron moving in the field exceeds 10% of the speed of light.

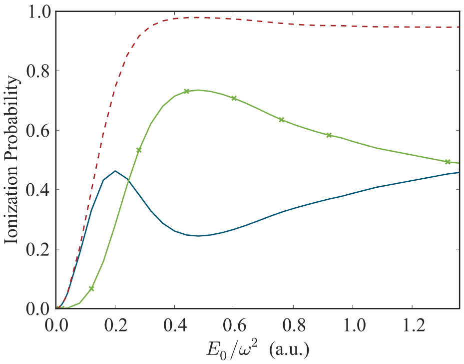

FIG. 2. (Color online) Single (full blue line), double (full green line with crosses) and total (dashed red line) ionization probabilities plotted against the electronic displacement for the case of a 6-cycle pulse with $\omega = 4$ a.u.

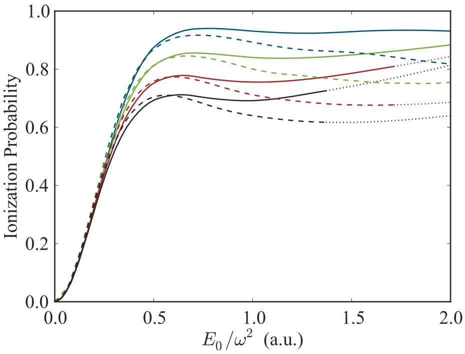

FIG. 3. (Color online) Ionization probabilities for a constant pulse duration of 2π a.u. The lines correspond to laser frequencies of $\omega =$ 4, 6, 8, and 10 a.u. from top to bottom, or equivalently pulse lengths of 4, 6, 8, and 10 cycles. The solid lines are the full calculations. The dashed lines are the IE calculations. The dotted parts of the curves indicate where relativistic (nondipole) effects may influence the results.

0.7 a.u., independent of laser frequency and pulse duration. For very short pulse durations, e.g., the three-cycle pulse of $\omega = 10$ a.u., we observe a knee in the function, rather than a peak at the stabilization point. This is probably due to the relatively large bandwidth of these short pulses and the averaging this leads to. For long pulse durations, e.g., the 24-cycle pulse of $\omega = 4$ a.u., the atom is almost fully ionized, and the stabilizing effect turns out to be weak. The dashed lines in the figure are the results of the independent-electron model. They show good agreement with the full calculations for weak fields ($\alpha_0 < 0.5$ a.u.) and for long pulses, but otherwise tend to overestimate the stabilization. As a matter of fact, the results show that the electron-electron interaction suppresses stabilization in all cases. We will return to the reason for this later.

In Fig. 2, we examine in more detail the case with 6 cycles and $\omega = 4$ a.u., showing both the total-ionization probability and its single- and double-ionization components. Both the single- and double-ionization probabilities peak at specific values of the field, which is in qualitative agreement with the results of Volkova *et al.* [27] and Popov *et al.* [28]. As expected, the single ionization dominates for weak fields, but it peaks at $\alpha_0 \simeq 0.2$ a.u., where the probability for double ionization starts to increase rapidly. From $\alpha_0 \simeq 0.3$ a.u. on, double ionization is the dominant ionization channel. Then, the double-ionization probability attains a maximum value at the point where the single-ionization probability reaches its minimum, i.e., at $\alpha_0 \simeq 0.5$ a.u. The subsequent decrease in the double-ionization probability, in the stabilization regime, is accompanied by a corresponding rise in the single-ionization yield. This feature is a characteristic of the stabilization dynamics of helium in few-cycle laser pulses [34].

Figure 3 shows the ionization probability as a function of α_0 for a pulse of constant duration $T = 2\pi$ a.u., but for varying frequencies, $\omega = 4$, 6, 8, and 10 a.u. The corresponding results of the IE model are shown in dashed lines. One immediately perceives that for higher frequencies, the atom stabilizes at lower ionization probabilities, in accordance with the results in Fig. 1. Note that in the limit of weak fields, single ionization is by far the dominating ionization channel. Thus, from first-order perturbation theory, $P^{\text{ion}}_{\text{total}} \propto \alpha_0^2 T$. Now, since the pulse duration is kept fixed in Fig. 3 (as opposed to Fig. 1), this explains why the results of the calculations with different frequencies almost coincide at smaller fields. The figure also demonstrates the fact that the discrepancy between the IE model (dashed lines) and the full calculations (solid lines) increases with the intensity. Furthermore, the stabilizing effect turns out to be very weak in the fully correlated system. Whereas the full *ab initio* calculations give ionization probabilities that level off (low frequencies) or increase (high frequencies) for high intensities, the IE model returns probabilities that are noticeably lower. As the intensity grows, so does the discrepancy. As such, the simplified model tends to always underestimate the ionization probability, with the consequence that the stabilization effect is overestimated.

Note that for the highest frequencies considered in Figs. 1 and 3, the calculations extend into a region where the non-relativistic (dipole) approximation is likely to break down [15,30,31,52]. This is indicated in the figures. While we expect relativistic (nondipole) corrections to affect the calculated ionization probabilities to some extent in this region of field strengths, our analysis and conclusions are not dependent upon the affected subset of results and remain unaltered.

B. The role of electronic correlation

Figures 1 and 3 clearly demonstrate that the validity of the independent-electron model (11) breaks down in the superintense field regime. This may appear counterintuitive, as one might well expect the opposite to happen, i.e., that the importance of the electron-electron interaction should be negligible in the presence of a strong external perturbation. The reason why the electron-electron interaction in fact becomes more important in this limit can be understood by analyzing the dynamics in the so-called Kramers-Henneberger (KH) frame [35–38], the rest frame of a classical free electron in the laser field. In this frame, the Hamiltonian, Eq. (1), is cast into the form

$$H_{\mathrm{KH}} = \sum_{i=1}^{2} \left(\frac{\mathbf{p}_i^2}{2} + V_{\mathrm{KH}}\left[\mathbf{r}_i + \boldsymbol{\alpha}(t)\right] \right) + \frac{1}{|\mathbf{r}_1 - \mathbf{r}_2|}, \quad (16)$$

where

$$V_{\mathrm{KH}}\left[\mathbf{r}_i + \boldsymbol{\alpha}(t)\right] = -\frac{2}{|\mathbf{r}_i + \boldsymbol{\alpha}(t)|} \quad (17)$$

is the Kramers-Henneberger potential, and

$$\boldsymbol{\alpha}(t) = \int_0^t A_z(t')\, dt' \hat{\mathbf{z}} \quad (18)$$

represents the position relative to the laboratory frame of a classical free electron in the electric field $E_z(t) = -\partial A_z/\partial t$. One characteristic feature of the KH frame is that the dipole interaction terms enter into the electron-nucleus Coulomb potentials [c.f. Eq. (17)], which in turn become time dependent and modified by the external field. Note also that the electron-electron interaction term is left unaffected by the HK transformation. Assuming for the moment that the Hamiltonian is periodic in time, i.e., neglecting the pulse profile, the KH potentials, Eq. (17), are expanded in a Fourier series as

$$V_{\mathrm{KH}}\left[\mathbf{r}_i + \boldsymbol{\alpha}(t)\right] = \sum_n V_n(\alpha_0, \mathbf{r}_i) e^{-in\omega t} \quad (19)$$

with

$$V_n(\alpha_0, \mathbf{r}_i) = \frac{1}{T} \int_0^T e^{-in\omega t} V_{\mathrm{KH}}\left[\mathbf{r}_i + \boldsymbol{\alpha}(t)\right] dt. \quad (20)$$

Inserting the expansion [Eq. (19)] into the TDSE and applying high-frequency Floquet theory, Gavrila *et al.* [10,53–55] showed that the $n = 0$ component in Eq. (20) plays an increasingly important role in the dynamics at higher values of α_0. Furthermore, in the limit of superintense fields ($\alpha_0 \gg 1$), Førre *et al.* [15] showed that the ionization dynamics of atomic hydrogen is mainly dictated by the V_0 potential. Thus, in this limit, the dynamics of the system is approximately given by the effective Hamiltonian

$$H_{\mathrm{KH}}^{\mathrm{eff}} = \sum_{i=1}^{2} \left(\frac{\mathbf{p}_i^2}{2} + V_0(\alpha_0, \mathbf{r}_i) \right) + \frac{1}{|\mathbf{r}_1 - \mathbf{r}_2|}. \quad (21)$$

Note that this Hamiltonian is time independent and accounts for *shake-up* (excitation) and *shake-off* (ionization) in the strong-field limit.

An analysis of the properties of the V_0 potential term in the vicinity of the origin reveals that it can be neglected relative to the electron-electron repulsion term in the limit $\alpha_0 \to \infty$, provided the two-electron wave function is localized, i.e., $\langle r_1 \rangle \ll \alpha_0$ and $\langle r_2 \rangle \ll \alpha_0$. This means that the dynamics of the two-electron system, in the limit of superintense fields and for sufficiently short pulses, ultimately reduces to that of a pure Coulomb explosion process effectuated by the Coulomb repulsion term in Eq. (21). From this, we conclude that the electron-electron interaction is in fact very important in the strong-field limit, effectively reducing the stabilization effect. Returning to the laboratory frame of reference, this should be understood in the following way: In the very-strong-field limit, the electrons effectively behave like free particles in the field, moving side by side with respect to the field axis. As this happens, the nuclear attraction may become less important than the mutual repulsion between the electrons, and the ionization is most likely initiated by electron-electron scattering events (Coulomb explosion) and not electron-nucleus collisions. This explains qualitatively why the ionization probabilities, calculated within the independent-electron model, deviate increasingly from the exact ones in the limit of stronger fields (cf. Figs. 1 and 3). As such, the observed deviation is indeed a manifestation of the breakdown of the single-particle picture in superstrong fields.

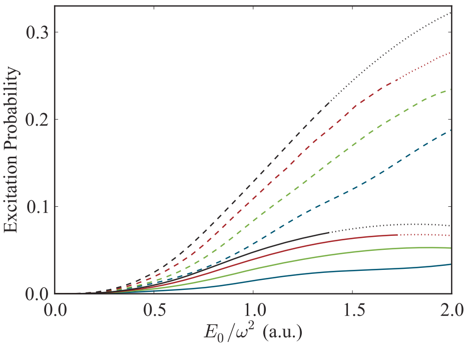

FIG. 4. (Color online) Excitation probabilities for the same scenario as in Fig. 3. The laser frequencies are $\omega = 10$, 8, 6, and 4 a.u. from top to bottom. The dashed lines are the results from the IE model, while the solid lines are the results from the full calculations. Relativistic (nondipole) effects may influence the results for high frequencies and field strengths (dotted curves).

Notice that the effective Hamiltonian in Eq. (21) only depends indirectly on the laser frequency through the displacement amplitude α_0, explaining why the validity of the IE model in Fig. 3 breaks down at approximately the same value of α_0 independent of the laser frequency.

Figure 4 shows the probability of excitation of helium for the cases considered in Fig. 3. Comparing Figs. 3 and 4, we observe that the decreasing ionization probability in the stabilization regime is accompanied by a corresponding increase in the excitation probability. Note that due to the high photon energy, excitation is here caused by shake-up processes, merely demonstrating the importance of the V_0 potential in the stabilization regime. The figure also clearly expresses the fact that shake-up is more important for the higher frequencies and that the IE model fails in describing shake-up (and shake-off) processes accurately, in accordance with the KH discussion above.

C. Analysis of angular and energy distributions

Further insight into the strong-field behavior of helium may be gained by examining the energy distribution of the ejected

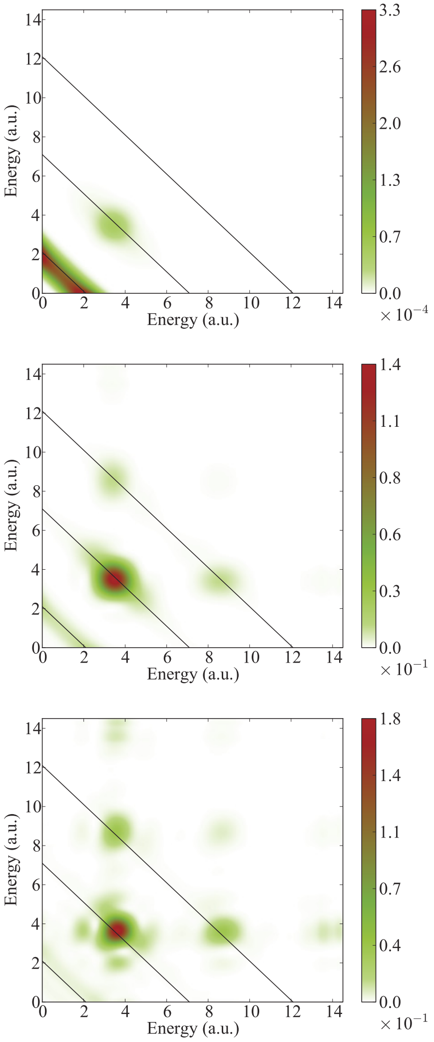

FIG. 5. (Color online) Double-ionization energy distribution for an $\omega = 5$ a.u. six-cycle pulse (182 as), and for field strengths of 1 (upper panel), 10 (middle panel), and 20 a.u. (lower panel).

electrons. In particular, imprints left by the electron interaction in the angular distribution of the outgoing electrons may give further clues as to its importance at the different field-strength regimes considered here.

In Fig. 5, the double-ionization energy distribution is shown for three different field strengths, 1, 10, and 20 a.u. (from top to bottom). The pulse duration was fixed at six cycles (182 as) with a frequency of 5 a.u. At the lower intensity (amplitude), one-photon ionization dominates as expected. As the intensity increases, two-photon ionization becomes prominent, and higher-order double-electron above threshold ionization (DATI) peaks start to appear [32]. Since the one-photon process is highly correlated and depends critically on the exchange of energy between the two electrons, it becomes less important at stronger fields, and two-photon double ionization takes over as the dominating channel. At the highest intensity, more structures appear in the energy spectrum, caused by sidebands in the pulse, and the one-photon-ionization process has become negligible.

The two-photon DATI component manifests itself as a single-peaked structure in Fig. 5, in contrast to the common double-peak structure associated with sequential ionization [32]. With the ultrashort pulse considered here, the second photon is absorbed before the residual ion has had time to relax to the ground state, but if the duration is increased to beyond 20 cycles, relaxation may occur and a double-peak structure appears (not shown here). The fact that the two peaks, corresponding to sequential two-photon double ionization in the long-pulse limit, shift toward each other in the short-pulse regime and eventually merge into one single peak (located at equal energy sharing) is well known and has been studied in a series of papers in the weak-field (perturbative) limit [33,56–65]. The results in Fig. 5 demonstrate that this feature survives in the superintense field regime, representing a clear departure from the independent-electron model [Eq. (11)].

Figure 6 shows the conditional angular distributions of the ejected electrons obtained at the two-photon DATI peak in Fig. 5, with equal energy sharing, and one of the electrons emitted along the polarization direction (indicated with an

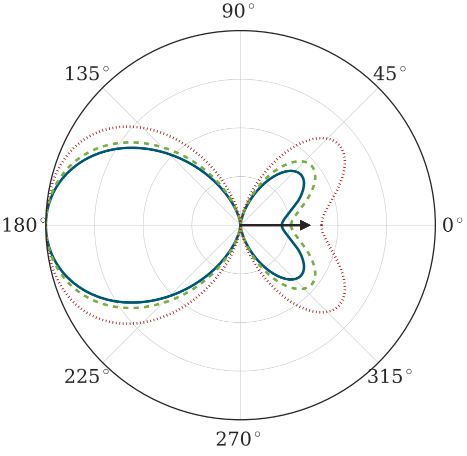

FIG. 6. (Color online) Angular distributions for double ionization with equal energy sharing $E_1 = E_2 = (2\omega - I_p)/2$. The arrow indicates the fixed direction of the first electron. Solid (blue) line: $E_0 = 1$ a.u. Dashed (green) line: $E_0 = 10$ a.u. Dotted (red) line: $E_0 = 20$ a.u.

arrow in the figure). The figure clearly shows that the distribution has a backward-forward asymmetry even at the highest intensity considered, demonstrating the breakdown of the single-particle picture, wherein a symmetric double-lobe (dipole) distribution would be found. The results are in accordance with recent results obtained at weaker fields [56,57,63], and shows that the back-to-back ejection mechanism is largely preserved even at very strong fields.

From numerical studies of stabilization in atomic hydrogen, it is known that the stabilization phenomenon is accompanied by the appearance of slow electrons [15]. As the intensity is increased beyond the ionization maximum, where stabilization sets in, and for sufficiently short pulses, a peak structure near zero energy appears in the electron energy spectrum, becoming increasingly dominant as the intensity becomes large. This may be understood from the Kramers-Henneberger analysis above and the importance of the V_0 potential in the limit of short, intense pulses. In order to provide a baseline comparison for the two-electron case considered here, we have calculated the energy distribution for ionization of He$^+$, with identical pulse characteristics as those used in Fig. 5. The result is shown in the upper panel of Fig. 7. We note the presence of above threshold ionization peaks, and, at the highest intensities, a slow electron peak (SEP) near zero energy [15,66]. The corresponding single-ionization energy distribution of helium is shown in the lower panel of Fig. 7, and indeed, a slow electron peak is visible. Note that the onset of slow electrons occurs at lower-field strengths in the single ionization of helium than in He$^+$, which is related to the different ionization potentials (I_p).

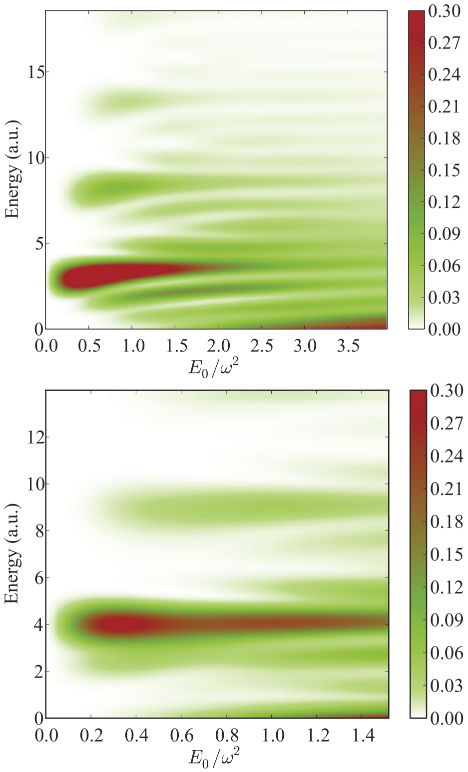

FIG. 7. (Color online) Energy distributions as a function of laser field strength. Top panel: He$^+$. Bottom panel: helium (single ionization). See text for details.

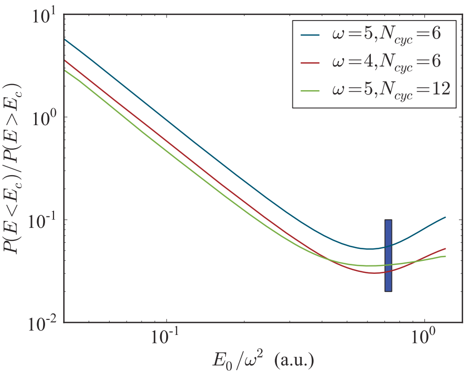

FIG. 8. (Color online) Ratio of slow to fast electrons for the double-ionization process, shown for different pulse frequencies and durations, and plotted as a function of α_0. The blue bar indicates the region where the corresponding double-ionization probability is maximum, where stabilization sets in.

Now, examining the lower panel in Fig. 5, it appears that slow electrons do not emerge in the double-ionization process at this intensity. However, the ionization potential is greater than that for single ionization, and, therefore, higher intensities are needed to reach the regime where a SEP may appear. Since He$^+$, with an ionization potential of $I_p = 2$ a.u., exhibits an onset of slow electrons around 50 a.u., similar or possibly even higher-field strengths may be required for a SEP to appear in the double ionization of helium. We may, however, observe the onset of slow electrons by partitioning the double-ionization energy distribution into a low- and a high-energy part, and considering the ratio of these two (cf. Fig. 8). In this figure, values of the ratio $P(E < E_c)/P(E > E_c)$, where $E_c = 3/2\omega - I_p$, for different frequencies and pulse durations are shown, and in all cases, we observe an increase of low-energy electrons after the stabilization peak (indicated by the blue bar); however, it is most pronounced for the shorter pulses.

IV. CONCLUSION

In conclusion, we have presented an in-depth analysis of two-electron dynamics driven by high-intensity ultrashort laser pulses in the xuv regime. Expanding on our earlier investigation of correlation effects in the stabilization of helium, we have shown that stabilization occurs within a narrow interval of values of α_0, independent of frequency and pulse duration. This is also the point at which an independent-electron picture begins to break down, demonstrating the important role of the electron-electron interaction at high intensities. Through an analysis of a high-intensity limit form of the Hamiltonian, expressed in the Kramers-Henneberger frame, this feature may be understood. Further indications of intense-field correlation effects are found in the angular distributions, where a backward-forward asymmetry is found for a wide range of intensities. Finally, we have shown that slow electrons emerge at high intensities, as they do in one-electron systems, but at different intensities for single and double ionization.

ACKNOWLEDGMENTS

This work was supported by the Bergen Research Foundation (Norway). The calculations were performed on the Cray XT4 (Hexagon) supercomputer at Parallab, University of Bergen (Norway). CPU hours were provided by NOTUR.

[1] M. Pont and M. Gavrila, Phys. Rev. Lett. **65**, 2362 (1990).

[2] Q. Su, J. H. Eberly, and J. Javanainen, Phys. Rev. Lett. **64**, 862 (1990).

[3] M. V. Fedorov and A. M. Movsesian, J. Phys. B **21**, L155 (1988).

[4] J. H. Eberly and K. C. Kulander, Science **262**, 1229 (1993).

[5] S. Geltman, J. Phys. B **27**, 257 (1994).

[6] M. Pont, N. R. Walet, M. Gavrila, and C. W. McCurdy, Phys. Rev. Lett. **61**, 939 (1988).

[7] K. C. Kulander, K. J. Schafer, and J. L. Krause, Phys. Rev. Lett. **66**, 2601 (1991).

[8] K. Burnett, P. L. Knight, B. R. M. Piraux, and V. C. Reed, Phys. Rev. Lett. **66**, 301 (1991).

[9] S. Geltman, Chem. Phys. Lett. **237**, 286 (1995).

[10] M. Gavrila, J. Phys. B **35**, R147 (2002).

[11] A. M. Popov, O. V. Tikhonova, and E. A. Volkova, J. Phys. B **36**, R125 (2003).

[12] K. Yamanouchi, S. L. Chin, P. Agostini, G. Ferrante, and M. Fedorov, in *Progress in Ultrafast Intense Laser Science I*, Springer Series in Chemical Physics, Vol. 84 (Springer, Berlin, 2006), pp. 1–18.

[13] R. Grobe and C. K. Law, Phys. Rev. A **44**, R4114 (1991).

[14] J. Grochmalicki, M. Lewenstein, and K. Rzkazewski, Phys. Rev. Lett. **66**, 1038 (1991).

[15] M. Førre, S. Selstø, J. P. Hansen, and L. B. Madsen, Phys. Rev. Lett. **95**, 043601 (2005).

[16] M. Dondera, H. G. Muller, and M. Gavrila, Phys. Rev. A **65**, 031405(R) (2002).

[17] R. Grobe and J. H. Eberly, Phys. Rev. A **47**, R1605 (1993).

[18] Q. Wei, S. Kais, and N. Moiseyev, Phys. Rev. A **76**, 013407 (2007).

[19] M. P. de Boer, J. H. Hoogenraad, R. B. Vrijen, L. D. Noordam, and H. G. Muller, Phys. Rev. Lett. **71**, 3263 (1993).

[20] N. J. van Druten, R. C. Constantinescu, J. M. Schins, H. Nieuwenhuize, and H. G. Muller, Phys. Rev. A **55**, 622 (1997).

[21] A. Talebpour, C.-Y. Chien, and S. L. Chin, J. Phys. B **29**, 5725 (1996).

[22] J. H. Hoogenraad, R. B. Vrijen, and L. D. Noordam, Phys. Rev. A **50**, 4133 (1994).

[23] T. Shintake *et al.*, Nature Photon. **2**, 555 (2008).

[24] W. Ackermann *et al.*, Nat. Photon. **1**, 336 (2007).

[25] E. Allaria, C. Callegari, D. Cocco, W. M. Fawley, M. Kiskinova, C. Masciovecchio, and F. Parmigiani, New J. Phys. **12**, 075002 (2010).

[26] M. Gavrila and J. Shertzer, Phys. Rev. A **53**, 3431 (1996).

[27] E. A. Volkova, V. V. Gridchin, A. M. Popov, and O. V. Tikhonova, JETP **99**, 320 (2004).

[28] A. M. Popov, O. V. Tikhonova, and E. A. Volkova, Laser Phys. **17**, 103 (2007).

[29] D. Bauer and F. Ceccherini, Phys. Rev. A **60**, 2301 (1999).

[30] A. Staudt and C. H. Keitel, J. Phys. B **36**, L203 (2003).

[31] A. Staudt and C. H. Keitel, Phys. Rev. A **73**, 043412 (2006).

[32] J. S. Parker, L. R. Moore, K. J. Meharg, D. Dundas, and K. T. Taylor, J. Phys. B **34**, L69 (2001).

[33] S. Laulan, H. Bachau, B. Piraux, J. Bauer, and G. L. Kamta, J. Mod. Opt. **50**, 353 (2003).

[34] T. Birkeland, R. Nepstad, and M. Førre, Phys. Rev. Lett. **104**, 163002 (2010).

[35] W. Pauli and M. Fierz, Nuovo Cimento **15**, 167 (1938).

[36] H. A. Kramers, *Collected Scientific Papers* (North-Holland, Amsterdam, 1956).

[37] W. C. Henneberger, Phys. Rev. Lett. **21**, 838 (1968).

[38] F. H. Faisal, J. Phys. B **6**, L89 (1973).

[39] H. G. Muller and M. Fedorov, *Super Intense Laser-Atom Physics*, Vol. 4 (Kluwer, Dordrecht, 1996).

[40] T. Birkeland and R. Nepstad, computer code PYPROP [http://pyprop.googlecode.com].

[41] C. de Boor, *A Practical Guide to Splines*, rev. ed. (Springer-Verlag, New York, 2001).

[42] H. Bachau, E. Cormier, P. Decleva, J. E. Hansen, and F. Martín, Rep. Prog. Phys. **64**, 1815 (2001).

[43] B. H. Bransden and C. J. Joachain, *Physics of Atoms and Molecules*, 2nd ed. (Pearson Education, Harlow, 2003).

[44] Y. Saad and M. H. Schultz, J. Sci. Stat. Comput. **7**, 856 (1986).

[45] Y. Saad, *Iterative Methods for Sparse Linear Systems* (SIAM, Philadelphia, 2003).

[46] J. Feist, S. Nagele, R. Pazourek, E. Persson, B. I. Schneider, L. A. Collins, and J. Burgdörfer, Phys. Rev. A **77**, 043420 (2008).

[47] L. B. Madsen, L. A. A. Nikolopoulos, T. K. Kjeldsen, and J. Fernández, Phys. Rev. A **76**, 063407 (2007).

[48] D. C. Sorensen, SIAM J. Matrix Anal. Appl. **13**, 357 (1992).

[49] R. Nepstad, T. Birkeland, and M. Førre, Phys. Rev. A **81**, 063402 (2010).

[50] S. Geltman, Phys. Rev. Lett. **54**, 1909 (1985).

[51] X. M. Tong and C. D. Lin, J. Phys. B **38**, 2593 (2005).

[52] S. Selstø, E. Lindroth, and J. Bengtsson, Phys. Rev. A **79**, 043418 (2009).

[53] M. Gavrila and J. Z. Kamiński, Phys. Rev. Lett. **52**, 613 (1984).

[54] M. Gavrila, *Atoms in Intense Laser Fields* (Academic, New York, 1992).

[55] M. Gavrila, I. Simbotin, and M. Stroe, Phys. Rev. A **78**, 033404 (2008).

[56] A. Palacios, T. N. Rescigno, and C. W. McCurdy, Phys. Rev. A **79**, 033402 (2009).

[57] J. Feist, S. Nagele, R. Pazourek, E. Persson, B. I. Schneider, L. A. Collins, and J. Burgdörfer, Phys. Rev. Lett. **103**, 063002 (2009).

[58] S. Laulan and H. Bachau, Phys. Rev. A **68**, 013409 (2003).

[59] K. L. Ishikawa and K. Midorikawa, Phys. Rev. A **72**, 013407 (2005).

[60] I. F. Barna, J. Wang, and J. Burgdörfer, Phys. Rev. A **73**, 023402 (2006).

[61] E. Foumouo, S. Laulan, B. Piraux, and H. Bachau, J. Phys. B **39**, S427 (2006).

[62] E. Foumouo, P. Antoine, H. Bachau, and B. Piraux, New J. Phys. **10**, 025017 (2008).

[63] A. Palacios, D. A. Horner, T. N. Rescigno, and C. W. McCurdy, J. Phys. B **43**, 194003 (2010).

[64] E. Foumouo, A. Hamido, P. Antoine, B. Piraux, H. Bachau, and R. Shakeshaft, J. Phys. B **43**, 091001 (2010).

[65] T.-G. Lee, M. S. Pindzola, and F. Robicheaux, Phys. Rev. A **79**, 053420 (2009).

[66] K. Toyota, O. I. Tolstikhin, T. Morishita, and S. Watanabe, Phys. Rev. Lett. **103**, 153003 (2009).

PAPER II

II

Stabilization of circular Rydberg atoms by circularly polarized infrared laser fields

S. Askeland, S. A. Sørngård, I. Pilskog, R. Nepstad and M. Førre

Physical Review A, **84**, 033423 (2011)

PHYSICAL REVIEW A **84**, 033423 (2011)

Stabilization of circular Rydberg atoms by circularly polarized infrared laser fields

S. Askeland,[1,*] S. A. Sørngård,[1,†] I. Pilskog,[1,2] R. Nepstad,[1] and M. Førre[1,‡]
[1]*Department of Physics and Technology, University of Bergen, N-5007 Bergen, Norway*
[2]*Laboratoire de Chimie Physique - Matière et Rayonnement, Université Pierre et Marie Curie - CNRS (UMR 7614), F-75231 Paris Cedex 05, France*

(Received 31 August 2011; published 29 September 2011)

The ionization dynamics of circular Rydberg states in strong circularly polarized infrared (800 nm) laser fields is studied by means of numerical simulations with the time-dependent Schrödinger equation. We find that at certain intensities, related to the radius of the Rydberg states, atomic stabilization sets in, and the ionization probability decreases as the intensity is further increased. Moreover, there is a strong dependence of the ionization probability on the rotational direction of the applied laser field, which can be understood from a simple classical analogy.

DOI: 10.1103/PhysRevA.84.033423 PACS number(s): 32.80.Fb, 32.80.Rm, 32.80.Ee

I. INTRODUCTION

Photoionization of atoms and molecules by a single photon impact has been studied since the early days of quantum mechanics. For the simplest atomic system in nature, hydrogen, which has a binding energy of 13.6 eV, absorption of a single photon with an energy exceeding this value will induce direct breakup of the system. With increasing photon flux, additional photons can be absorbed, giving rise to multiphoton processes and above-threshold ionization (ATI) [1,2]. From perturbation theory calculations, a general increase in breakup probability with intensity of the imposed radiation field is expected. It therefore came as a big surprise to many when, more than 20 years ago, theoretical studies of atomic hydrogen in ultraintense, high-frequency laser fields showed some evidence of the complete opposite scenario, i.e., that the atom may eventually become more stable as the ionizing radiation gets stronger [3–11]. This rather counterintuitive phenomenon, called atomic stabilization, has since then been studied extensively; see, e.g., [12–15] and references therein. It has also been argued that atomic stabilization has a classical counterpart [16,17]. (See also [12] and references therein.) Very recently, the stabilization dynamics of helium in intense xuv laser pulses was investigated [18,19].

Primarily a high-frequency phenomenon, atomic stabilization is expected to be important at photon energies exceeding the binding energy of the system at hand and for very high intensities. In the case of the hydrogen atom, photon energies exceeding 13.6 eV and intensities on the order of 10^{16} W/cm^2 or more are required [9,20,21]. Up to present times, experimental confirmation of atomic stabilization in tightly bound atomic systems, such as neutral atoms in their ground state, has been obstructed due to lack of the laser technology required to produce the necessary conditions. The possibility of observing the phenomenon in excited atomic states was pointed out early [4,22–25], and the first experimental signature of atomic stabilization in low-lying Rydberg atoms was reported in 1993 [26,27] and later confirmed [28], irradiating $5g$ circular states in neon by intense ($\sim 10^{13}$–10^{14} W/cm^2) 620-nm linearly polarized laser pulses. The experimental findings are consistent with theoretical predictions [29–32].

In this work, we investigate atomic stabilization of circular Rydberg states in hydrogen exposed to short, intense circularly polarized laser pulses, using parameters well within reach of conventional Ti:sapphire lasers. The m quantum number is set equal to l for the initial state, so that the electron is "orbiting" the nucleus in a counterclockwise fashion. Furthermore, the field polarization vector is chosen to lie in the plane defined by the initial circular state. We show that stabilization occurs for a range of pulse durations and different initial states, and that the radius of the circular initial state determines at which intensities stabilization sets in. It is also shown that the polarization direction of the applied field has a significant impact on the ionization dynamics for lower lying Rydberg states. Specifically, at 800 nm the $5g$ circular state is orders of magnitude more likely to ionize with counterclockwise (co-rotating field) as opposed to clockwise (counter-rotating field) polarization at lower intensities, but both enter the stabilization regime at the same intensity. This difference disappears for more highly excited states, such as the $10l$ circular state. Classical ensemble calculations are performed to investigate the underlying mechanisms.

Atomic units, where m_e, $\hbar$, and e are scaled to unity, are used throughout unless stated otherwise.

II. METHOD

In this paper we study the ionization dynamics of hydrogen when the atom is excited to a low-lying circular Rydberg state and exposed to a rotating electric field. To that end we solve numerically the time-dependent Schrödinger equation (TDSE) in full dimensionality. The Hamiltonian of such a system, described in the frame of the velocity gauge and the dipole approximation, reads

$$H = \frac{\mathbf{p}^2}{2} - \frac{1}{r} + A_x(t)p_x + A_y(t)p_y. \qquad (1)$$

Each component of the circularly polarized laser field, here represented by its vector potential, is modulated by a

---

[*] sigurd.askeland@ift.uib.no
[†] stian.sorngard@ift.uib.no
[‡] morten.forre@ift.uib.no

©2011 American Physical Society

sine-squared carrier envelope,

$$A_j(t) = A_0 \sin^2\left(\frac{\pi t}{T}\right)\sin(\omega t + \phi_j), \quad (2)$$

where $A_0 = E_0/\omega$, E_0 is the peak amplitude of the electric field, ω is the laser frequency, and T is the total pulse duration. To make the field rotate in the xy plane, there is a phase difference between the two components. We define the field to be rotating clockwise (as seen from above) if $\phi_x = 0$ and $\phi_y = \pi/2$, and counterclockwise if the phases are interchanged.

The radial and angular ranks of the wave function are expanded in B splines and spherical harmonics, respectively,

$$\Psi(\mathbf{r},t) = \sum_{k,l,m} c_{klm}(t)\frac{B_k(r)}{r}Y_{lm}(\Omega). \quad (3)$$

The wave function, expressed as a vector of the expansion coefficients c_{klm}, is propagated forward in time using the unconditionally stable Cayley-Hamilton form of the time propagator

$$\left(\mathbf{S} + \frac{i\Delta t}{2}\mathbf{H}\right)\mathbf{c}(t+\Delta t) = \left(\mathbf{S} - \frac{i\Delta t}{2}\mathbf{H}\right)\mathbf{c}(t). \quad (4)$$

Here $\mathbf{H}$ is the Hamilton matrix of the TDSE and $\mathbf{S}$, with $S_{ij} = \int B_i(r)B_j(r)\,dr$, is the B-spline overlap matrix. The need for an overlap matrix stems from the fact that B-spline functions are not orthogonal.

This propagation scheme calls for solving a linear system of equations in each time step. The set is too large to be solved directly, and an iterative method must therefore be applied. The selected one is the so-called generalized minimum-residual method (GMRES) [33,34], a Krylov subspace method well suited for non-Hermitian systems of equations, which is the case in Eq. (4). As the system is rather stiff, a preconditioning of the matrix $(\mathbf{S} + i\Delta t/2\mathbf{H})$ is required to ensure a reasonable convergence of the GMRES iterations. For this purpose the incomplete LU factorization [34] is employed to provide an approximation $\mathbf{M}$ to the matrix. Thus we are in practice solving the system $\mathbf{M}^{-1}(\mathbf{S} + i\Delta t/2\mathbf{H})\mathbf{c} = \mathbf{M}^{-1}(\mathbf{S} - i\Delta t/2\mathbf{H})\mathbf{c}$, rather than the one in Eq. (4). Even so, a Krylov subspace spanned by up to 40 vectors are required to converge within a tolerance of 10^{-13} at the highest field intensities.

The large spatial extension of the Rydberg states requires large radial boxes when propagated in time. In our computations we use boxes with an upper bound between 600 and 2000 a.u., depending on the initial state and the electric field strength. We use a number of seventh-order B splines corresponding to one spline per unit length, and let them be equally distributed throughout the range. The angular basis is truncated at $l = 41$ in computations where $E_0 \leqslant 0.3$ a.u., and at $l = 63$ otherwise.

The ionization probability is found through projection of the wave function onto hydrogen bound states,

$$P_{\text{ion}} = 1 - |\langle\Psi(\mathbf{r},T)|\psi_{\text{bound}}\rangle|^2. \quad (5)$$

Another approach, i.e., projecting the final wave function onto continuum state wave functions (Coulomb waves), has also been applied to a selection of test cases in order to verify consistency with the bound state analysis.

All velocity gauge calculations were performed with the PYPROP framework [35], a PYTHON/C++ based software package for solving the TDSE; details may be found elsewhere [36,37]. Additional calculations were made with a split-operator approach using the acceleration form of the light-matter interaction (the Kramers-Henneberger frame of reference) [21,38], to independently check the reliability of our results.

III. RESULTS

The majority of the TDSE simulations were performed with a $5g$ ($m = 4$) initial state. This is a circular state, i.e., the probability density is roughly torus shaped. The torus is positioned in the xy plane symmetrically with respect to the z axis. We define the major radius of the torus to be equal to the expectation value of r, viz. 27.5 a.u. Our case differs from the scenario studied earlier [26–32] in that we apply (in-plane) circularly polarized pulses, with components in the x and y directions, instead of z polarized fields. Thus, the axial symmetry of the problem is broken, resulting in a strong m mixing. In addition, we model a Ti:sapphire laser pulse with a wavelength of 800 nm. For all initial states considered, the photon energy $\hbar\omega$ exceeds the binding energy E_i, viz. $\hbar\omega > E_i$, and atomic stabilization is expected to occur at high intensities [12]. The ionization and stabilization dynamics are studied for pulses of different durations and varying peak intensities.

In the following discussion the reader will notice that we continually refer to the term "excursion amplitude." By this we mean the spatial displacement of a classical free electron influenced by an electric field. This quantity, also known as the quiver amplitude, is given by $\alpha = E_0/\omega^2$.

At the considered wavelength, nondipole effects are expected to play a role when the intensity exceeds 10^{16} W/cm^2. As the majority of the calculations were performed at intensities significantly lower than this, nondipole effects were not expected to be important here. To further confirm this, additional calculations including nondipole terms were conducted [21,39]. Regarding relativistic effects, these should also be negligible, because the maximum quiver velocity ($v = E_0/\omega$) attained by the electron in our calculations is less than 9% of the speed of light.

We first consider the TDSE calculations for the $5g$ initial state; see the left panels in Fig. 1. These depict the ionization probabilities as a function of the peak intensity of the laser pulse, for a number of pulse durations, ranging from 4 to 12 optical cycles. In all cases, stabilization, i.e., a local maximum in the ionization probability, occurs for excursion amplitudes in the vicinity of $\langle r\rangle = 27.5$ a.u., indicated by a dashed vertical line in the figure. The probability density of the initial state is shown as a shaded shape at the bottom of the lower panel. With circularly polarized light, there are two field configuration options: the field either co-rotates or counter-rotates relative to the electronic probability current in the torus. The upper (left) panel in Fig. 1 depicts the results for the co-rotation scenario, while the lower panel shows the corresponding results for the counter-rotation case. There is a slight difference in the position of the stabilization threshold for the two cases: 21 a.u. for counter-rotation and 28 a.u. for co-rotation.

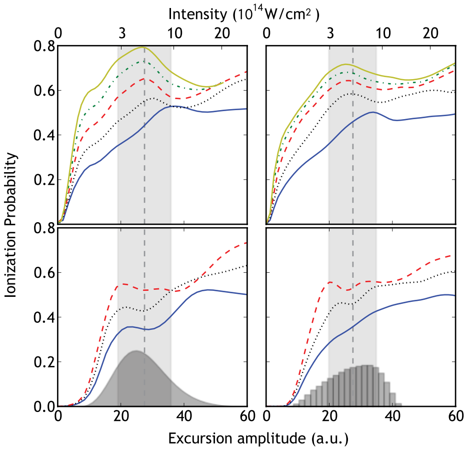

FIG. 1. (Color online) Ionization probability as function of excursion amplitude and laser intensity for the circular 5g ($m = 4$) state. The laser wavelength is 800 nm. The left panels are TDSE results, and the right panels are results from classical trajectory Monte Carlo (CTMC) calculations. For the upper panels a circular field that is co-rotating with respect to the electronic motion was used. The curves, from bottom up, represent laser pulses with 4, 6, 8, 10, and 12 optical cycles. The lower panels are the results for the corresponding counter-rotating case. Here, the curves, from bottom up, represent laser pulses with 4, 6, and 8 optical cycles. The shaded function in the bottom left panel is the shape of the radial probability distribution of the initial (quantum mechanical) state, and the histogram in the bottom right panel represents the distribution of initial radii for the electrons in the CTMC simulations. The dashed lines mark the radial expectation values $\langle r \rangle$ in the two cases, and the lighter shaded areas indicate the widths of the initial probability distributions, here taken to be the standard deviation.

When comparing the upper and lower (left) panels in Fig. 1, it is worth noting the different behavior at low intensities. While the curves for the co-rotation set out with a steep inclination, for the counter-rotation case they display a much more gradual increase. Quantum mechanically, the great difference in ionization yields between the co- and counter-rotation cases for lower field strengths is simply connected to a correspondingly great difference in their respective electric dipole couplings. For a circular state, the dipole selection rules for the absorption of one photon from the field are

$$\begin{aligned} \text{Counter-rot.: } \Delta m &= -1, & \text{Co-rot.: } \Delta m &= +1, \\ \Delta l &= \pm 1, & \Delta l &= +1. \end{aligned} \tag{6}$$

Thus, as long as one-photon absorption is the dominant ionization channel, the co-rotating field is more likely to ionize the system, simply because the relevant dipole couplings are about an order of magnitude larger (for the $n = 5$ circular state) than those relevant to the counter-rotating field. For more highly excited circular states, the difference between co- and counter-rotation is less pronounced, as can be seen in Fig. 2.

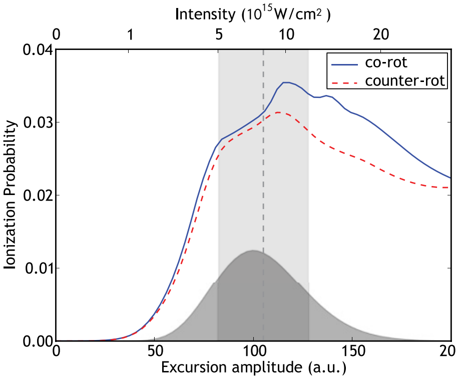

FIG. 2. (Color online) Ionization probability as function of excursion amplitude and laser intensity for the circular 10l ($m = 9$) state in circularly polarized electric fields with the wavelength 800 nm. The shaded function is the shape of the radial probability distribution of the initial state, and the dashed line marks its radial expectation value. The width of the torus, represented by the standard deviation of the radial distribution, is shown in a lighter shade of grey.

It is no coincidence that the value of the excursion amplitude at the point of stabilization coincides with the radius of the initial state probability density torus. When selecting the 10l ($m = 9$) state as the initial state (see Fig. 2), whose torus radius is 105 a.u., we get the stabilization threshold at 110–115 a.u., well within the "width" of the torus. Note that the co- and counter-rotating cases yield very similar results in this case, especially for the lower excursion amplitudes (field intensities), the reason being that the electron's (classical) "orbit" frequency is very low compared to the field frequency, making the difference between the co- and counter-rotating scenarios less important. We observe the same with a 7i ($m = 6$) initial state (not shown here), where again the stabilization threshold occurs at excursion amplitudes that approximately correspond to the torus radius, which in that case is 52.5 a.u. We made sure this connection also existed when using a different laser frequency, and if we used an in-plane linearly polarized laser field instead. Figure 3 shows the results for an x polarized laser pulse on a 5g ($m = 4$) initial state for pulses of 4, 6, and 8 optical cycles, and the results are, in fact, in qualitative agreement with the results in Fig. 1.

The observed close correlation between the torus radius $\langle r \rangle$ and the value of the excursion amplitude (electric field strength) at the stabilization threshold, has a simple intuitive explanation. During the action of an intense pulse, the electric field will drive the torus-shaped electron "cloud" around, while the heavy nucleus is nearly stationary (completely so in our model). When the excursion amplitude approaches the radius of the initial-state torus, the strong electric field pulls the densest part of the electron cloud into the nucleus. In the case of circularly polarized fields, the entire length of the torus may then be pulled through the "nuclear area," with the consequence that there is a high likelihood for the electron to interact strongly with the nucleus. Keeping in mind that interaction

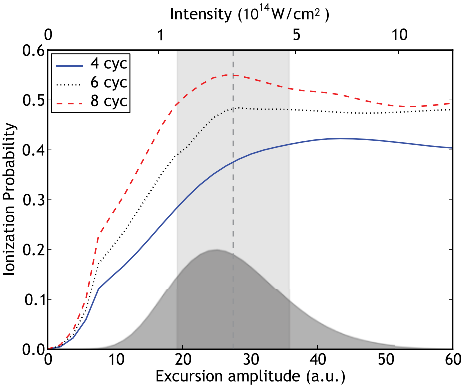

FIG. 3. (Color online) Ionization probability as function of excursion amplitude and laser intensity for the $5g$ $(m = 4)$ state in a linearly polarized electric field along the x direction with the wavelength 800 nm. The shaded function is the shape of the radial probability distribution of the initial state, and the dashed line marks its radial expectation value. The width of the torus, represented by the standard deviation of the radial distribution, is shown in a lighter shade of grey.

with the nucleus is the catalyst for ionization, it should be of no surprise that the point of maximum ionization approximately coincides with the excursion of the initial (circular) state. For lower intensities and excursion amplitudes, the nucleus will remain inside the torus, causing less ionization. Similarly, at larger excursion amplitudes beyond the stabilization point, the torus is displaced to such an extent that it no longer intersects the nucleus, and less ionization occurs. However, since the central attractive force is no longer centered inside the torus, the latter will start to disperse, in effect ionizing. The balance of these two mechanisms qualitatively explains the local minima of the ionization probability after stabilization has occurred.

Looking at the probability density function during the pulse for the different orientations, see Fig. 4, we notice that in co-rotating scenarios, part of the electron cloud is quickly pulled in close to the nucleus. This does not happen to the same extent in the counter-rotating scenarios. Specifically, Fig. 4 shows the probability density in the xy plane for half a cycle of the pulse when this phenomenon can easily be observed. The figure shows the developments for the co- and counter-rotating cases side by side. The arrows indicate the direction and strength of the electric field. The force on the electron works in the opposite direction. Looking at the left panels in Fig. 4, showing the counter-rotating scheme, we see little action. For the co-rotating case, on the other hand, a sizable portion of the electron probability is pulled to the nucleus at an early stage, making a spiraling tail structure behind the nucleus.

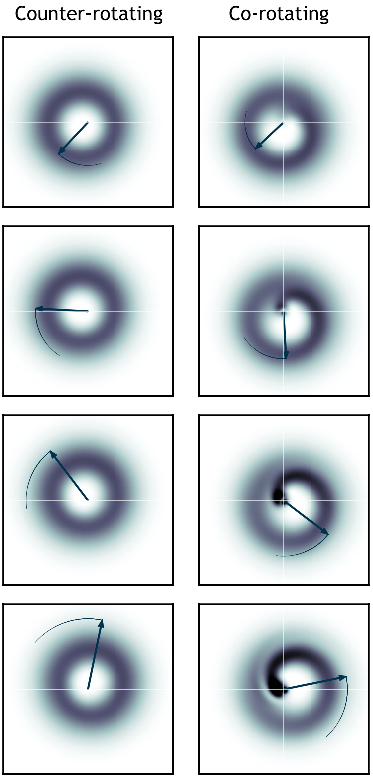

FIG. 4. (Color online) Snapshots of the probability density in the $z = 0$ plane, during half an optical cycle early in the laser pulse. The initial wave function is the circular $5g$ $(m = 4)$ state, and the laser pulse contains four optical cycles. The peak intensity is 0.44×10^{14} W/cm^2, corresponding to an excursion amplitude of 8 a.u., but the figure depicts the probability density function when the intensity is in the range 0.1–0.4×10^{14} W/cm^2, or for an excursion amplitude of 3–7 a.u. The left panels show the clockwise rotation of the electric field, and the right panels show the co-rotation. The arrows illustrate the size and direction of the electric field. For the counter-rotating pulse, the ionization probability is 0.02, and the probability of staying in the initial state is 0.97. For the co-rotating pulse, the ionization probability is 0.24, and the probability of staying in the initial state is 0.71.

The ionization dynamics of Rydberg atoms in circularly polarized fields has been studied before in terms of classical mechanics [40,41]. The classical approach may facilitate the interpretation of the results from the quantum-mechanical calculations, and provide further insight into the underlying physical mechanisms [40,41]. We therefore made supporting calculations using the classical trajectory Monte Carlo (CTMC) method [42,43]. Solving the Newtonian equations of motion for a large number ($\sim$30 000) of individual electron trajectories, corresponding to different initial conditions picked at random from a microcanonical ensemble [44–46], a classical estimate for the ionization probability P_{ion} is obtained simply by taking the ratio between the number of trajectories corresponding to a free electron after the pulse and the total number of trajectories. To mimic the initial circular quantum state, only orbits fulfilling the constraint $(m - 1/2)\hbar < L_z < (m + 1/2)\hbar$, $m = l = n - 1$ being the quantum numbers of the hydrogenic circular state and L_z the z component of the angular momentum, were selected.

The results of the classical calculations are shown in the right panels in Fig. 1. Comparing left and right panels, i.e., the quantum and classical results, respectively, the similarity is striking. The agreement could be seen as a manifestation of Bohr's correspondence principle [47]. In particular, the stabilization phenomenon is clearly seen to have a classical counterpart [12,16,17]. The classical ensemble calculations further support the close relationship between the radius of the initial state (distribution) and the point (field excursion amplitude) at which stabilization sets in.

As is apparent from the CTMC results in Fig. 1, the classical approach is well suited for these stabilization simulations. It stands to reason that the different behavior for low intensities should have a classical explanation as well as the quantum-mechanical explanation given above. This may also give us a more intuitive feel for the mechanisms involved. First we adopt the CTMC view of the initial state, that of an ensemble of independent electrons orbiting the nucleus. All the electrons will orbit in a counterclockwise fashion, with approximately the same angular momentum, but varying degree of eccentricity. The electric field, when it is turned on, rotates much (∼ ×9) faster than the electrons orbit the nucleus. The perturbations from the field drive the electrons into trajectories with a "telephone cord" appearance, in particular for higher field strengths. Regardless of rotational direction, the field will always alternately accelerate and decelerate the electron. This, however, is where the difference between co- and counter-rotation comes in. The periods of acceleration and deceleration will be longer in the co-rotating case than in the counter-rotating case, because the field and the electron are rotating in the same direction in the former case. The closer the frequency of the laser field is to the electron's rotation frequency, the longer the periods. For electrons in sufficiently eccentric orbits that pass close to the nucleus when the field is approximately aligned with the velocity of the electron, a large transfer of energy may occur in the co-rotating case. The eccentricity of the orbit is here crucial for the ionization to take place, since the instantaneous electronic rotation frequency should match the field frequency when the electron is closest to the nucleus. This field-assisted "slingshot maneuver" scenario [48,49] is illustrated in Fig. 5, where a single ionizing trajectory is shown, together with energy and angular frequency as a function of time. Here, the electron clearly receives two "kicks" when passing close to the nucleus, before entering an open, ionizing orbit. Although for the sake of simplicity, only a single classical trajectory is shown in the figure, we would like to emphasize that, in the limit of weak fields, all ionizing orbits will indeed exhibit a very similar behavior to the one depicted in Fig. 5. As such, the chosen example contains all essential features of the ionization dynamics in the limit of weak fields. In the counter-rotating case the slingshot effect becomes much less efficient, simply due to the counter-rotating fashion of the field, effectively causing less ionization. This explains the great difference in the ionization yields between the co- and counter-rotation cases in Fig. 1.

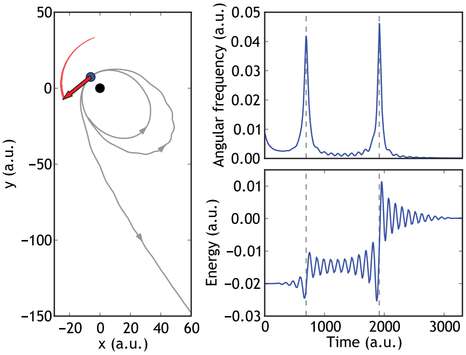

FIG. 5. (Color online) Left panel: The trajectory of a classical electron in an elliptical orbit being kicked out when closest to the nucleus (black dot). The red arrow indicates the direction of the force from the field acting on the electron (blue dot) at the very moment when the ionization takes place. Upper right panel: The angular frequency of the electron, relative to the origin, as function of time. Lower right panel: The energy of the electron as function of time. The two times the distance between electron and nucleus is minimized are marked by vertical dashed lines in the right panels. For the sake of illustration, the pulse applied in this figure is somewhat longer (30 cycles) than the pulses used throughout. The peak intensity is 1.08×10^{11} W/cm^2.

IV. CONCLUSION

By means of quantum simulations with the time-dependent Schrödinger equation supported by classical simulations using the classical trajectory Monte Carlo method, the ionization and stabilization dynamics of circular Rydberg states in hydrogen, subjected to circularly polarized 800-nm (Ti:sapphire) laser pulses, have been studied under experimentally realistic conditions. It is shown that at certain intensities, intimately related to the radius of the initial Rydberg states, atomic stabilization sets in. Both co- and counter-rotating fields with respect to the direction in which the electron orbits the nucleus were considered, and great differences in the corresponding ionization yields were identified, in particular for the lower-lying Rydberg states, but both enter the stabilization regime at similar intensities. These differences were reproduced in classical calculations, providing further insight into the underlying ionization mechanisms.

ACKNOWLEDGMENTS

This project was supported by the Bergen Research Foundation (Norway), and the computations were performed on the Cray XT4 (Hexagon) supercomputer at Parallab, University of Bergen (Norway). CPU hours were provided by the Norwegian Metacenter for Computational Science (NOTUR).

[1] P. Agostini, F. Fabre, G. Mainfray, G. Petite, and N. K. Rahman, Phys. Rev. Lett. **42**, 1127 (1979).

[2] W. Becker, F. Grasbon, R. Kopold, D. Milosevic, G. Paulus, and H. Walther, in *Advances In Atomic, Molecular, and Optical Physics*, Vol. 48, edited by B. Bederson and H. Walther (Academic, New York, 2002), p. 35.

[3] M. Pont, N. R. Walet, M. Gavrila, and C. W. McCurdy, Phys. Rev. Lett. **61**, 939 (1988).

[4] M. V. Fedorov and A. M. Movsesian, J. Phys. B **21**, L155 (1988).

[5] K. C. Kulander, K. J. Schafer, and J. L. Krause, Phys. Rev. Lett. **66**, 2601 (1991).

[6] K. Burnett, P. L. Knight, B. R. M. Piraux, and V. C. Reed, Phys. Rev. Lett. **66**, 301 (1991).

[7] M. Pont and M. Gavrila, Phys. Rev. Lett. **65**, 2362 (1990).

[8] Q. Su, J. H. Eberly, and J. Javanainen, Phys. Rev. Lett. **64**, 862 (1990).

[9] J. H. Eberly and K. C. Kulander, Science **262**, 1229 (1993).

[10] S. Geltman, J. Phys. B **27**, 257 (1994).

[11] S. Geltman, Chem. Phys. Lett. **237**, 286 (1995).

[12] M. Gavrila, J. Phys. B **35**, R147 (2002).

[13] A. M. Popov, O. V. Tikhonova, and E. A. Volkova, J. Phys. B **36**, R125 (2003).

[14] K. Yamanouchi, S. L. Chin, P. Agostini, G. Ferrante, and M. Fedorov, in *Progress in Ultrafast Intense Laser Science I*, Springer Series in Chemical Physics Vol. 84, (Springer, Berlin, 2006), p. 1.

[15] M. Boca, H. G. Muller, and M. Gavrila, J. Phys. B **37**, 147 (2004).

[16] J. Grochmalicki, M. Lewenstein, and K. Rzaewski, Phys. Rev. Lett. **66**, 1038 (1991).

[17] R. Grobe and C. K. Law, Phys. Rev. A **44**, R4114 (1991).

[18] T. Birkeland, R. Nepstad, and M. Førre, Phys. Rev. Lett. **104**, 163002 (2010).

[19] S. A. Sørngård, S. Askeland, R. Nepstad, and M. Førre, Phys. Rev. A **83**, 033414 (2011).

[20] M. Dondera, H. G. Muller, and M. Gavrila, Phys. Rev. A **65**, 031405(R) (2002).

[21] M. Førre, S. Selstø, J. P. Hansen, and L. B. Madsen, Phys. Rev. Lett. **95**, 043601 (2005).

[22] M. Pont and R. Shakeshaft, Phys. Rev. A **44**, R4110 (1991).

[23] R. J. Vos and M. Gavrila, Phys. Rev. Lett. **68**, 170 (1992).

[24] R. M. Potvliege and P. H. G. Smith, Phys. Rev. A **48**, R46 (1993).

[25] M. V. Fedorov, Laser Phys. **3**, 219 (1993).

[26] M. P. de Boer, J. H. Hoogenraad, R. B. Vrijen, L. D. Noordam, and H. G. Muller, Phys. Rev. Lett. **71**, 3263 (1993).

[27] M. P. de Boer, J. H. Hoogenraad, R. B. Vrijen, R. C. Constantinescu, L. D. Noordam, and H. G. Muller, Phys. Rev. A **50**, 4085 (1994).

[28] N. J. van Druten, R. C. Constantinescu, J. M. Schins, H. Nieuwenhuize, and H. G. Muller, Phys. Rev. A **55**, 622 (1997).

[29] B. Piraux and R. M. Potvliege, Phys. Rev. A **57**, 5009 (1998).

[30] A. M. Popov, O. V. Tikhonova, and E. A. Volkova, Laser Phys. **9**, 1053 (1999).

[31] A. M. Popov, O. V. Tikhonova, and E. A. Volkova, Laser Phys. **10**, 779 (2000).

[32] E. A. Volkova, A. M. Popov, and O. V. Tikhonova, J. Exp. Theor. Phys. **89**, 1045 (1999).

[33] Y. Saad and M. H. Schultz, J. Sci. Stat. Comput. **7**, 856 (1986).

[34] Y. Saad, *Iterative Methods for Sparse Linear Systems* (SIAM, Philadelphia, 2003).

[35] T. Birkeland and R. Nepstad, PYPROP, [http://pyprop.googlecode.com].

[36] T. Birkeland, Ph.D. thesis, University of Bergen, 2009.

[37] R. Nepstad, T. Birkeland, and M. Førre, Phys. Rev. A **81**, 063402 (2010).

[38] J. P. Hansen, T. Sørevik, and L. B. Madsen, Phys. Rev. A **68**, 031401 (2003).

[39] M. Førre, Phys. Rev. A **74**, 065401 (2006).

[40] D. Farrelly and T. Uzer, Phys. Rev. Lett. **74**, 1720 (1995).

[41] T. Uzer, E. Lee, and D. Farrelly, Phys. Rev. A **58**, 4761 (1998).

[42] R. Abrines and I. C. Percival, Proc. Phys. Soc. London **88**, 861 (1966).

[43] R. Abrines and I. C. Percival, Proc. Phys. Soc. London **88**, 873 (1966).

[44] C. O. Reinhold and C. A. Falcón, Phys. Rev. A **33**, 3859 (1986).

[45] J. P. Hansen, J. Lu, L. B. Madsen, and H. M. Nilsen, Phys. Rev. A **64**, 033418 (2001).

[46] H. M. Nilsen, L. B. Madsen, and J. P. Hansen, Phys. Rev. A **66**, 025402 (2002).

[47] N. Bohr, Z. Phys. **2**, 423 (1920).

[48] A. F. B. A. Prado, J. Guid. Control Dyn. **19**, 1142 (1996).

[49] U. Saalmann and J. M. Rost, Phys. Rev. Lett. **100**, 133006 (2008).

PAPER III

Direct two-photon double ionization of H_2

A. S. Simonsen, S. A. Sørngård, R. Nepstad and M. Førre

Physical Review A, **85**, 063404 (2012)

III

PHYSICAL REVIEW A **85**, 063404 (2012)

Direct two-photon double ionization of H_2

A. S. Simonsen,* S. A. Sørngård, R. Nepstad, and M. Førre†
Department of Physics and Technology, University of Bergen, N-5007 Bergen, Norway

(Received 2 February 2012; published 5 June 2012)

We have studied the process of direct (nonsequential) two-photon double ionization of molecular hydrogen (H_2). Solving the time-dependent Schrödinger equation by an *ab initio* method, total (generalized) and single-differential cross sections are obtained at photon energies from 26 to 33 eV. Both parallel and perpendicular orientation of the molecule with respect to the laser polarization direction are considered, and the results are compared with previously calculated cross sections at 30 eV, as well as the predictions of a simple model.

DOI: 10.1103/PhysRevA.85.063404 PACS number(s): 33.80.Rv, 33.80.Eh, 42.50.Hz

I. INTRODUCTION

The problem of direct, as opposed to sequential, two-photon double ionization of xenon [1] and helium [2,3] was introduced some time ago. Since then, the direct (nonsequential) process in helium has been the focus of great interest, both theoretically [4–21] and experimentally [22–27]. These investigations were partly triggered by the development of high-order harmonic [28,29] and free-electron laser (FEL) [30,31] light sources, as well as the development of sophisticated numerical methods, capable of tackling correlated motions in few [4,32] and multiphoton [33] ionization processes. The study of fundamental breakup processes in nature is important and paves the way for further investigations of the role of correlations in few and multiphoton multiple ionization processes in atoms and molecules. More recently, the four-body breakup of H_2 by two-photon impact has received considerable attention, both in the direct [34–37] and sequential regime [38,39].

Employing the time-dependent close coupling method, Colgan *et al.* [34] studied the direct two-photon double ionization of H_2 by 30 eV photons. Total and triple-differential cross sections for the process were obtained for both parallel and perpendicular orientation of the molecule with respect to the linear laser polarization direction. In 2009, Morales *et al.* [35] revisited the problem employing a time-independent approach and the method of exterior complex scaling. Clear discrepancies in the respective triple-differential cross sections were found. Even more recently, Guan *et al.* [36,37] calculated the corresponding cross sections using a fully *ab initio*, nonperturbative approach, solving the time-dependent Schrödinger equation in prolate spheroidal coordinates for a 10 cycle laser pulse of peak intensity 10^{14} W/cm^2. The cross sections were obtained projecting the final continuum wave function onto a set of uncorrelated two-center Coulomb waves, and the results were found to differ from those reported by both Colgan *et al.* [34] and Morales *et al.* [35].

In the present work we again consider the problem of direct two-photon double ionization (TPDI) of H_2. For this purpose, we solve the time-dependent Schrödinger equation in spherical coordinates employing a recently developed *ab initio* numerical framework [17,40]. The framework has here been further developed in order to take into account the two-center nature of the problem. Following [34–37] we assume the fixed-nuclei approximation in the calculations, that is, the nuclei are considered being fixed at their equilibrium internuclear distance at $R = 1.4$ a.u. throughout the interaction with the laser pulse. Since the electrons are ejected almost instantaneously in the direct TPDI process and move apart much faster than the Coulomb exploding nuclei, the approximation is expected to be very accurate, concordant with earlier findings in the corresponding one-photon double ionization process in H_2 [41,42].

Using a 15 cycle laser pulse of sine-squared shape, total (generalized) and single-differential cross sections are obtained for photon energies in the interval 26 to 33 eV. The TPDI cross sections are calculated by subtracting the bound and single continuum states from the total wave packet. In order to obtain sufficiently converged results and to minimize the effect of the Coulombic repulsion between the electrons, the wave function is propagated some additional optical cycles after the pulse before the projections are performed. The results of the full calculations are compared with the previous ones [34–37], and differences and similarities are noted. Furthermore, they are compared with the predictions of a simple approximate model, recently proposed for the corresponding TPDI process in helium [12,18].

Atomic units, where m_e, $\hbar$, and e are scaled to unity, are used throughout unless stated otherwise.

II. THEORY AND NUMERICAL APPROACH

A. Numerical model

The Hamiltonian for fixed-in-space H_2 interacting with a laser field consists of two parts,

$$\widehat{H} = \widehat{H}_{\mathrm{mol}} + \widehat{H}_{\mathrm{field}}, \tag{1}$$

where the first term is the field-free Hamiltonian for the hydrogen molecule,

$$\widehat{H}_{\mathrm{mol}} = \sum_{i=1}^{2}\left(\frac{\mathbf{p}_i^2}{2} - \frac{1}{|\mathbf{r}_i + \mathbf{R}/2|} - \frac{1}{|\mathbf{r}_i - \mathbf{R}/2|}\right) + \frac{1}{|\mathbf{r}_1 - \mathbf{r}_2|}, \tag{2}$$

$\mathbf{R}$ being the internuclear vector. The second term is the interaction with the laser field, which in a semiclassical approximation takes the form

$$\widehat{H}_{\mathrm{field}} = \mathbf{A}(t)\cdot(\mathbf{p}_1 + \mathbf{p}_2), \tag{3}$$

when the velocity gauge and the dipole approximation have been assumed. The laser field is modeled by the classical

---

*aleks.simonsen@gmail.com
†morten.forre@ift.uib.no

©2012 American Physical Society

electric field $\mathbf{E} = -\partial_t \mathbf{A}$, with the time-dependent vector potential given as

$$\mathbf{A}(t) = A_0 \sin^2\left(\frac{\pi t}{T}\right)\cos(\omega t)\hat{\mathbf{u}}. \tag{4}$$

Here the unit vector $\hat{\mathbf{u}}$ defines the polarization of the linearly polarized field, $A_0 = \frac{E_0}{\omega}$, E_0 is the peak electric field amplitude, ω is the central frequency, and T is the pulse duration.

The standard procedure for solving a partial differential equation numerically is to expand the solution in a convenient basis, and subsequently solve the resulting system of ordinary differential equations. In our approach, the angular rank of the two-electron wave function is expanded in coupled spherical harmonics, and the radial ranks in B splines [43,44],

$$\Psi(r_1,r_2,\Omega_1,\Omega_2,t) = \sum_{i,j,k} c_{i,j,k}(t)\frac{B_i(r_1)}{r_1}\frac{B_j(r_2)}{r_2}\mathcal{Y}^{L,M}_{l_1,l_2}(\Omega_1,\Omega_2). \tag{5}$$

Here $k = \{l_1,l_2,L,M\}$ is a combined index for the angular indices. In this basis the radial and angular kinetic energy operators have a very sparse structure with few nonzero elements.

The H_2 molecule is a two-center system, and is in many respects best represented in prolate spheroidal coordinates, in which the H_2^+ molecule is separable. Nevertheless, it is still possible to utilize the single-center approach at the cost of being able to fully exploit the symmetry properties of the two-center system. In our case, the electron-nucleus interaction operator is expanded in spherical harmonics using the multipole expansion,

$$\begin{aligned}
&-\frac{1}{|\mathbf{r}_i + \mathbf{R}/2|} - \frac{1}{|\mathbf{r}_i - \mathbf{R}/2|} \\
&\quad = -\sum_{j\in 2\mathbb{Z}^*}\sum_{m=-j}^{j}\frac{4\pi}{2j+1}\frac{r_<^j}{r_>^{j+1}}Y^*_{j,m}(\theta,\phi)Y_{j,m}(0,0),
\end{aligned} \tag{6}$$

where $r_>$ and $r_<$ are the largest and smallest of r_i and $R/2$, respectively, the internuclear vector is assumed to lie along the z axis, and the index j runs over even integers. The single-center approach in H_2 deviates in general very little from the formalism commonly used for two-electron atomic systems like helium. The only difference, as evident from Eq. (6), is the need for terms beyond the monopole term to support the two-center nature of the system, making the calculations more demanding regarding memory requirements and run time.

As opposed to helium, the total angular momentum L is not a conserved quantity in the hydrogen molecule. While the helium ground state comprises only the $L = 0$ symmetry, the nonspherical symmetric electron-nucleus interaction entails the H_2 ground state to be composed of several even L components. In addition to $L = 0$ the most prominent components are those of $L = 2$, 4, and 6. When exposing the molecule to a linearly polarized laser field, it should be noted that the projection of the total angular momentum $M = m_1 + m_2$ onto the z axis is conserved and equal to zero as long as the axis of polarization is parallel to the internuclear vector (z axis). Whenever the polarization axis points elsewhere, the cylindrical symmetry of the system is broken and hence the M quantum number is not conserved.

Our numerical scheme for solving the two-electron time-dependent Schrödinger equation (TDSE) in the basis (5) was presented earlier [17,40]. The framework has already been used for single and double ionization studies in helium [17,18,45,46] and the negative hydrogen ion [47].

B. Extracting physical information

Extracting physical quantities for a two-photon double ionization process is a nontrivial task, because of the complications that arise in separating the single and double continuum. In the present work, an approximation to the double continuum component is obtained by applying complementary projection operators to the final wave function. The complementary projection operators are constructed to remove the population from bound and single continuum channels. First the bound component is removed. Then the single continuum is removed by subtracting all components from the wave function corresponding to one electron remaining in a bound H_2^+ state, as follows:

$$\begin{aligned}
|\Psi_{\mathrm{DC}}\rangle = {} & |\Psi_{\mathrm{f}}(\mathbf{r}_1,\mathbf{r}_2,t)\rangle - \sum_m \big\langle \phi_m^{H_2^+}(\mathbf{r}_1)\big|\Psi_{\mathrm{f}}(\mathbf{r}_1,\mathbf{r}_2,t)\big\rangle\big|\phi_m^{H_2^+}(\mathbf{r}_1)\big\rangle \\
& - \sum_{m'} \big\langle \phi_{m'}^{H_2^+}(\mathbf{r}_2)\big|\Psi_{\mathrm{f}}(\mathbf{r}_1,\mathbf{r}_2,t)\big\rangle\big|\phi_{m'}^{H_2^+}(\mathbf{r}_2)\big\rangle \\
& + \sum_{m,m'} \big\langle \phi_m^{H_2^+}(\mathbf{r}_1)\big|\big\langle \phi_{m'}^{H_2^+}(\mathbf{r}_2)\big|\Psi_{\mathrm{f}}(\mathbf{r}_1,\mathbf{r}_2,t)\big\rangle \\
& \times \big|\phi_m^{H_2^+}(\mathbf{r}_1)\big\rangle\big|\phi_{m'}^{H_2^+}(\mathbf{r}_2)\big\rangle.
\end{aligned} \tag{7}$$

Here m and m' sum over all H_2^+ bound states, which are obtained by numerical diagonalization of the H_2^+ single-particle Hamiltonian. Furthermore, Ψ_{DC} represents the double continuum wave packet, and $\Psi_{\mathrm{f}}(\mathbf{r}_1,\mathbf{r}_2,t)$ is the total (single + double) continuum wave function at some time t after the pulse. It should be noted that in this approximation to the double continuum, the electron-electron interaction is completely disregarded. Thus, for the method to be valid, it is important that the electrons are as far apart as possible. This is achieved by letting the wave packet propagate for some additional time after the end of the laser pulse, typically 5–10 optical cycles, in order for the ionized wave packet to reach near-asymptotic distances before the projections are performed. The disadvantage of this approach is of course the necessity of using correspondingly larger radial boxes.

After the double continuum wave packet Ψ_{DC} is found using Eq. (7), the generalized cross section is easily obtained,

$$\sigma = \left(\frac{\omega}{I_0}\right)^2 \frac{P_{\mathrm{ion}}}{T_{\mathrm{eff}}}, \tag{8}$$

where

$$P_{\mathrm{ion}} = \langle \Psi_{\mathrm{DC}}|\Psi_{\mathrm{DC}}\rangle \tag{9}$$

is the double ionization probability. Here ω is the photon energy, I_0 is the laser intensity, and T_{eff} is the effective pulse duration. The latter quantity depends on the pulse shape, and for a sine squared envelope it is given by $T_{\mathrm{eff}} = \frac{35}{128}T$ [14].

The electron energy distributions are derived from the double continuum wave packet by projecting it onto pairs of H_2^+ field-free continuum energy eigenstates—one for each

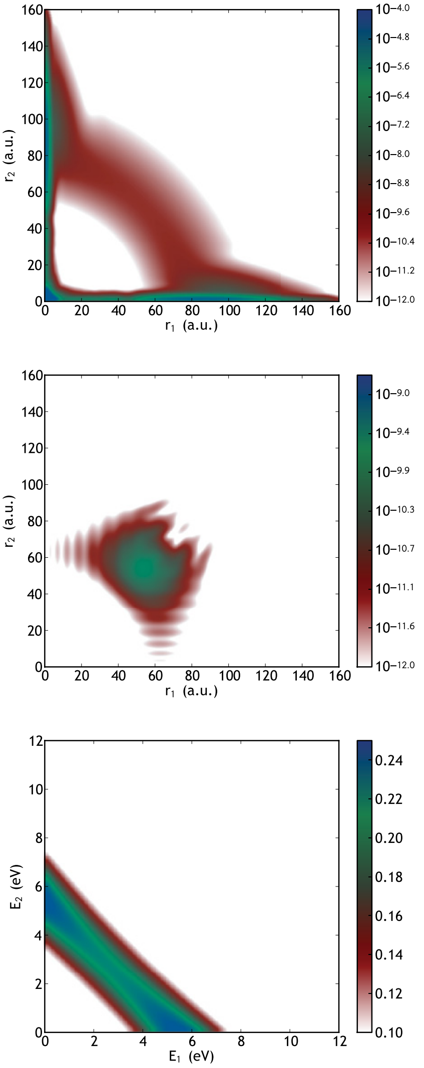

FIG. 1. (Color online) Upper panel: Radial wave function density (in a.u.) obtained at seven optical cycles after the end of the pulse, for a 15-cycle laser pulse of central frequency $\omega = 1.05$ a.u. (corresponding to the photon energy 28.6 eV), and intensity 10^{13} W/cm^2. The molecule is oriented parallel to the polarization axis of the laser field. The scale is logarithmic. Intermediate panel: Radial wave function density (in a.u.) of the double continuum wave packet, after the bound and single ionized populations have been removed. Lower panel: Corresponding energy distribution of the outgoing electrons in units of 10^{-5} a.u.

electron, as obtained by numerical diagonalization of the full one-electron H_2^+ Hamiltonian imposing zero boundary condition at the edge of the radial box. Although these energy eigenstates do not fulfill the incoming-wave boundary condition [48], which would be a prerequisite for calculating angular-differential cross sections, they do produce accurate energy-differential quantities, provided the electron-electron interaction can be neglected.

III. RESULTS AND DISCUSSION

In our calculations, and in the case of parallel alignment of the molecule, we have used a radial box extending to $r_{\max} = 160$ a.u., covered by 147 B splines. The B splines are distributed on a grid such that the density of splines is exponentially decreasing away from the center of mass. After

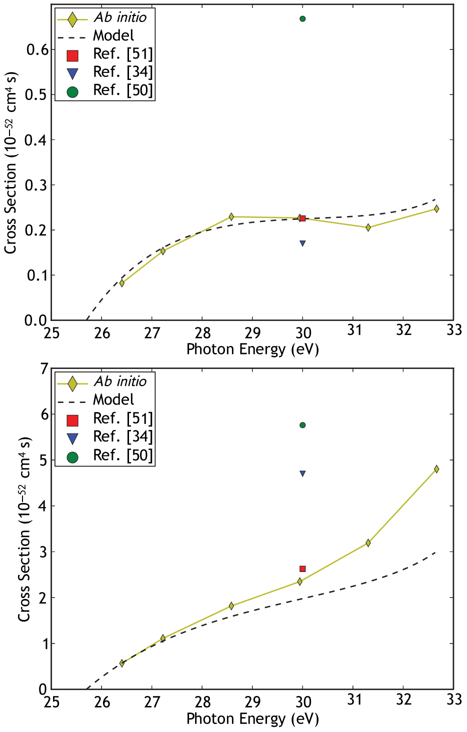

FIG. 2. (Color online) Total (generalized) cross section for the process of direct (nonsequential) two-photon double ionization of H_2. Upper panel: molecule oriented parallel with the laser polarization axis. Lower panel: molecule oriented perpendicular to the laser polarization axis. Golden line with diamonds: present *ab initio* result. Dashed line: model result Eq. (10). Blue triangle: theoretical result by Colgan *et al.* [34]. Green circle: theoretical result by Morales *et al.* [35,50]. Red square: theoretical result by Guan *et al.* [37,51].

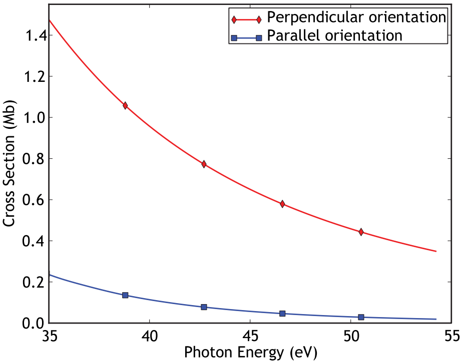

FIG. 3. (Color online) Photoionization cross section obtained for fixed-in-space H_2^+ molecules at $R = 1.4$ a.u. Blue line with squares: molecule oriented parallel to the laser polarization axis. Red line with diamonds: molecule oriented perpendicular to the laser polarization axis.

some distance (8 a.u in this work), the density of splines is held constant. The higher density close to the origin enables resolving the ground state to a satisfactory level. Furthermore, the angular basis is truncated at $l_{\max} = 6$, $L_{\max} = 12$, and $M = 0$. With this basis we obtain the ground state energy -1.8852 a.u., which is in satisfactory agreement with the calculated benchmark value -1.8888 a.u. [49]. Due to memory limitations, a somewhat smaller basis has been applied for the perpendicular geometry. In that case, $l_{\max} = 4$, $L_{\max} = 8$, $M = -2,-1,0,1,2$, and 101 B splines are distributed in a radial box extending to $r_{\max} = 150$ a.u. Varying the size of the basis sets, it is found that the cross sections are fairly well converged, both for the parallel and perpendicular geometries.

The upper panel in Fig. 1 displays the radial wave function density seven optical cycles after the interaction with a 15-cycle laser pulse. The photon energy is 28.6 eV. The corresponding double continuum wave packet, as obtained by the subtraction procedure described in Sec. II B, is shown in the intermediate panel. From this wave packet, the electrons' energy distribution is derived and depicted in the lower panel.

Figure 2 depicts our results for the total cross section, both for parallel (upper panel) and perpendicular (lower panel) orientation of the molecule with respect to the laser polarization axis. The results are obtained for a 15-cycle laser pulse of intensity 10^{13} W/cm^2. The wave packet is propagated for about seven optical cycles after the action of the pulse before the projections are performed. It should be noted that the calculated total cross sections vary by less than 3% from the time just after the pulse up to this point.

Also shown in Fig. 2 is the result of Colgan *et al.* [34] (blue triangle), Morales *et al.* [35,50] (green circle), and Guan *et al.* [37,51] (red square) at the photon energy 30 eV. The agreement between our calculated cross section at 30 eV and the value in [37,51] turns out to be excellent, whereas clear discrepancies with the results of the two other studies are found. It is not clear to us what is the origin of these discrepancies, but we nevertheless point out two possible explanations. First, Colgan *et al.* [34] used a 12-cycle (flat-top) laser pulse of peak intensity 10^{15} W/cm^2, which supports three and higher-order photon processes to a greater extent compared to our pulse, and that could possibly lead to a nonnegligible depletion of the population in the initial state. Second, as already pointed out by Colgan and co-authors [34], the doubly excited states of H_2, the first one lying only about 30 eV above the H_2 ground state at $R = 1.4$ a.u. [48], may have some influence on the results. This could possibly explain the difference between the results of the time-dependent and time-independent approaches, respectively.

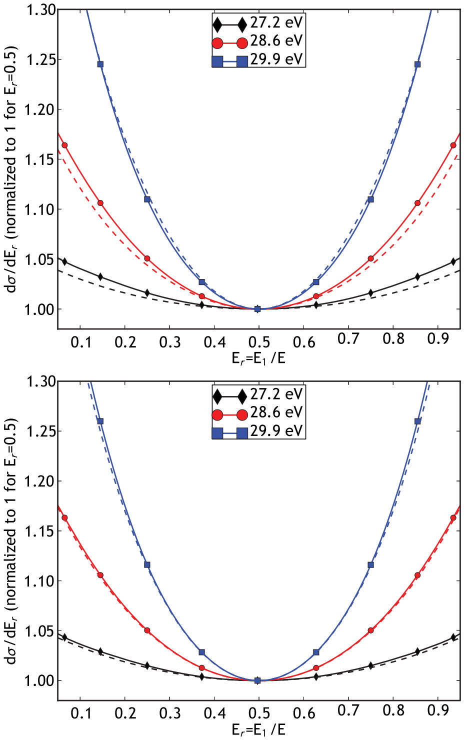

FIG. 4. (Color online) Single differential cross section (SDCS) for direct two-photon double ionization of H_2 at the photon energies 27.2, 28.6, and 29.9 eV. Full lines are the *ab initio* results and dashed lines indicate the prediction of the model Eq. (10). Upper panel: molecule oriented parallel with the laser polarization axis. These SDCSs are scaled, in order to align them for equal energy sharing, with the factors, 6.88, 4.82, and 5.31 for the photon energies 27.2, 28.6, and 29.9 eV, respectively. Lower panel: molecule oriented perpendicular to the laser polarization axis. Similarly, the SDCSs are scaled with the factors 0.95, 0.61, and 0.52 for the three photon energies 27.2, 28.6, and 29.9 eV.

A simple approximate model for the single-differential cross section for direct two-photon double ionization of helium was recently proposed by Horner *et al.* [12] and Førre *et al.* [18]. As a natural extension of these works, we propose the following approximate formula for the single-differential cross section in the process of two-photon double ionization of H_2,

$$\frac{d\sigma}{dE_1} \simeq \frac{1}{4}\left[\sqrt{f(E_1)} + \sqrt{f(2\hbar\omega - E_b - E_1)}\right]^2,$$
$$f(E_1) \equiv \frac{\hbar^3\omega^2}{\pi}\,\frac{\sigma_{H_2}(E_1+E_{H_2})\,\sigma_{H_2^+}(2\hbar\omega - E_1 - E_{H_2})}{(E_1+E_{H_2})(2\hbar\omega - E_1 - E_{H_2})(E_1+E_{H_2}-\hbar\omega)^2}. \tag{10}$$

Here $E_b = 51.4$ eV is the total binding energy of H_2, the energy $E_{H_2} = 16.5$ eV corresponds to the first (single) ionization threshold of H_2, and σ_{H_2} and $\sigma_{H_2^+}$ indicate the photoionization cross section for one-photon single ionization of H_2 and H_2^+, respectively. For further details about the models, see Refs. [18,52]. The relevant photoionization cross sections for the single ionization of H_2 was calculated by Sánchez and Martín [53]. Furthermore, the photoionization cross section of H_2^+ at $R = 1.4$ a.u. is given in Fig. 3 for the parallel and perpendicular orientation of the molecule, respectively.

The total cross section, as obtained by applying the approximate formula Eq. (10), is depicted in Fig. 2 by dashed lines. The model seems to yield results that are in reasonable agreement with our *ab initio* findings, which is somewhat surprising given the high complexity of the problem. Quite interestingly, and in agreement with our *ab initio* calculations, the model predicts a cross section about an order of magnitude larger for the perpendicular orientation as compared to the parallel one. In the model, this difference is attributed to a corresponding difference in the photoionization cross section of H_2^+ (cf. Fig. 3).

We now turn to the energy distributions of the ejected electrons. Figure 4 shows the energy resolved single-differential cross sections (SDCSs) at three selected photon energies, 27.2, 28.6, and 29.9 eV. The SDCSs are obtained from the respective energy distributions of the two electrons (cf. lower panel in Fig. 1). Upper and lower panels in Fig. 4 depict the results for the parallel and perpendicular geometry, respectively. Again, the agreement between the fully *ab initio* result and the model prediction is at a quantitative level, demonstrating the strength of the simple formula. At this point it should, however, be noted that the model does not apply to angular-resolved differential cross sections. As a matter of fact, the Coulombic repulsion between the electrons turns out to play a decisive role for the movement of the electrons in the continuum, even a long time after they have been ejected. Such long-range effects are not included in the model, and it is therefore not expected to be valid for the calculation of angular distributions.

IV. CONCLUSIONS

In conclusion, we have studied the two-photon double ionization of fixed-in-space hydrogen molecules (H_2), applying a B-spline based numerical method. Total (generalized) and single-differential cross sections are calculated at various photon energies and compared, when possible, with previously published results [34,35,37,50,51]. Our results are in agreement with the results of Guan *et al.* [37,51], as far as the total cross section is concerned, but further theoretical and experimental investigations are required in order to settle the problem definitely. We furthermore find that our results are in quantitative agreement with the predictions of a simple model, both for the total and single-differential cross sections. These observations are concordant with previous findings in the corresponding process in helium [18,20].

ACKNOWLEDGMENTS

This work was supported by the Bergen Research Foundation and the Norwegian metacenter for computational science (Notur). All calculations were performed on the Cray XT4 (Hexagon) supercomputer installation at Parallab, University of Bergen (Norway). The authors would like to thank X. Guan, K. Bartschat, F. Morales, and C. W. McCurdy for sending their results in numerical form.

---

[1] A. L'Huillier and G. Wendin, Phys. Rev. A **36**, 5632 (1987).
[2] M. Crance and M. Aymar, J. Phys. (France) **46**, 1887 (1985).
[3] M. A. Kornberg and P. Lambropoulos, J. Phys. B **32**, L603 (1999).
[4] J. Colgan and M. S. Pindzola, Phys. Rev. Lett. **88**, 173002 (2002).
[5] L. Feng and H. W. van der Hart, J. Phys. B **36**, L1 (2003).
[6] S. Laulan and H. Bachau, Phys. Rev. A **68**, 013409 (2003).
[7] B. Piraux, J. Bauer, S. Laulan, and H. Bachau, Eur. Phys. J. D **26**, 7 (2003).
[8] S. X. Hu, J. Colgan, and L. A. Collins, J. Phys. B **38**, L35 (2005).
[9] E. Foumouo, G. L. Kamta, G. Edah, and B. Piraux, Phys. Rev. A **74**, 063409 (2006).
[10] R. Shakeshaft, Phys. Rev. A **76**, 063405 (2007).
[11] I. A. Ivanov and A. S. Kheifets, Phys. Rev. A **75**, 033411 (2007).
[12] D. A. Horner, F. Morales, T. N. Rescigno, F. Martín, and C. W. McCurdy, Phys. Rev. A **76**, 030701(R) (2007).
[13] L. A. A. Nikolopoulos and P. Lambropoulos, J. Phys. B **40**, 1347 (2007).
[14] J. Feist, S. Nagele, R. Pazourek, E. Persson, B. I. Schneider, L. A. Collins, and J. Burgdörfer, Phys. Rev. A **77**, 043420 (2008).
[15] X. Guan, K. Bartschat, and B. I. Schneider, Phys. Rev. A **77**, 043421 (2008).
[16] E. Foumouo, P. Antoine, B. Piraux, L. Malegat, H. Bachau, and R. Shakeshaft, J. Phys. B **41**, 051001 (2008).
[17] R. Nepstad, T. Birkeland, and M. Førre, Phys. Rev. A **81**, 063402 (2010).
[18] M. Førre, S. Selstø, and R. Nepstad, Phys. Rev. Lett. **105**, 163001 (2010).
[19] A. Palacios, D. A. Horner, T. N. Rescigno, and C. W. McCurdy, J. Phys. B **43**, 194003 (2010).
[20] D. A. Horner, T. N. Rescigno, and C. W. McCurdy, Phys. Rev. A **81**, 023410 (2010).

[21] H. Bachau, Phys. Rev. A **83**, 033403 (2011).
[22] H. Hasegawa, E. J. Takahashi, Y. Nabekawa, K. L. Ishikawa, and K. Midorikawa, Phys. Rev. A **71**, 023407 (2005).
[23] Y. Nabekawa, H. Hasegawa, E. J. Takahashi, and K. Midorikawa, Phys. Rev. Lett. **94**, 043001 (2005).
[24] P. Antoine, E. Foumouo, B. Piraux, T. Shimizu, H. Hasegawa, Y. Nabekawa, and K. Midorikawa, Phys. Rev. A **78**, 023415 (2008).
[25] A. A. Sorokin, M. Wellhöfer, S. V. Bobashev, K. Tiedtke, and M. Richter, Phys. Rev. A **75**, 051402(R) (2007).
[26] A. Rudenko, L. Foucar, M. Kurka, T. Ergler, K. U. Kühnel, Y. H. Jiang, A. Voitkiv, B. Najjari, A. Kheifets, S. Lüdemann *et al.*, Phys. Rev. Lett. **101**, 073003 (2008).
[27] M. Kurka, J. Feist, D. A. Horner, A. Rudenko, Y. H. Jiang, K. U. Kühnel, L. Foucar, T. N. Rescigno, C. W. McCurdy, R. Pazourek *et al.*, New J. Phys. **12**, 073035 (2010).
[28] M. Hentschel, R. Kienberger, C. Spielmann, G. A. Reider, N. Milosevic, T. Brabec, P. Corkum, U. Heinzmann, M. Drescher, and F. Krausz, Nature (London) **414**, 509 (2001).
[29] P. M. Paul, E. S. Toma, P. Breger, G. Mullot, F. Augé, P. Balcou, H. G. Muller, and P. Agostini, Science **292**, 1689 (2001).
[30] T. Shintake *et al.*, Nat. Photon. **2**, 555 (2008).
[31] W. Ackermann *et al.*, Nat. Photon. **1**, 336 (2007).
[32] J. S. Parker, L. R. Moore, K. J. Meharg, D. Dundas, and K. T. Taylor, J. Phys. B **34**, L69 (2001).
[33] J. S. Parker, B. J. S. Doherty, K. T. Taylor, K. D. Schultz, C. I. Blaga, and L. F. DiMauro, Phys. Rev. Lett. **96**, 133001 (2006).
[34] J. Colgan, M. S. Pindzola, and F. Robicheaux, J. Phys. B **41**, 121002 (2008).
[35] F. Morales, F. Martín, D. A. Horner, T. N. Rescigno, and C. W. McCurdy, J. Phys. B **42**, 134013 (2009).
[36] X. Guan, K. Bartschat, and B. I. Schneider, Phys. Rev. A **82**, 041404(R) (2010).
[37] X. Guan, K. Bartschat, and B. I. Schneider, Phys. Rev. A **84**, 033403 (2011).
[38] Y. H. Jiang, A. Rudenko, E. Plésiat, L. Foucar, M. Kurka, K. U. Kühnel, T. Ergler, J. F. Pérez-Torres, F. Martín, O. Herrwerth *et al.*, Phys. Rev. A **81**, 021401(R) (2010).
[39] T.-G. Lee, M. S. Pindzola, and F. Robicheaux, J. Phys. B **43**, 165601 (2010).
[40] T. Birkeland, Ph.D. thesis, University of Bergen, 2009.
[41] W. Vanroose, D. A. Horner, F. Martín, T. N. Rescigno, and C. W. McCurdy, Phys. Rev. A **74**, 052702 (2006).
[42] W. Vanroose, F. Martín, T. N. Rescigno, and C. W. McCurdy, Science **310**, 1787 (2005).
[43] C. de Boor, *A Practical Guide to Splines*, revised ed. (Springer, New York, 2001).
[44] H. Bachau, E. Cormier, P. Decleva, J. E. Hansen, and F. Martín, Rep. Prog. Phys. **64**, 1815 (2001).
[45] T. Birkeland, R. Nepstad, and M. Førre, Phys. Rev. Lett. **104**, 163002 (2010).
[46] S. A. Sørngård, S. Askeland, R. Nepstad, and M. Førre, Phys. Rev. A **83**, 033414 (2011).
[47] R. Nepstad and M. Førre, Phys. Rev. A **84**, 021402(R) (2011).
[48] F. Martín, J. Phys. B **32**, R197 (1999).
[49] J. Sims and S. Hagstrom, J. Chem. Phys. **124**, 094101 (2006).
[50] F. Morales (private communication).
[51] X. Guan (private communication).
[52] D. A. Horner, C. W. McCurdy, and T. N. Rescigno, Phys. Rev. A **78**, 043416 (2008).
[53] I. Sánchez and F. Martín, J. Phys. B **30**, 679 (1997).

PAPER IV

Femtosecond-pulse-train ionization of Rydberg wave packets

S. I. Simonsen, S. A. Sørngård, M. Førre and J. P. Hansen

Physical Review A, **86**, 043423 (2012)

PHYSICAL REVIEW A **86**, 043423 (2012)

Femtosecond-pulse-train ionization of Rydberg wave packets

S. I. Simonsen,[*] S. A. Sørngård,[†] M. Førre, and J. P. Hansen
Department of Physics and Technology, University of Bergen, N-5007 Bergen, Norway

(Received 25 June 2012; revised manuscript received 9 August 2012; published 19 October 2012)

We calculate, based on first-order perturbation theory, the total and differential ionization probabilities from a dynamic periodic Rydberg wave packet of a given n-shell exposed to a train of femtosecond laser pulses. The total probability is shown to depend crucially on the laser repetition rate: For certain frequencies the ionization probability vanishes, while for others it becomes very large. The origin of this effect is the strong dependence of the ionization probability on the Stark quantum number. Correspondingly, the angular electronic distribution also changes significantly with the increasing number of pulses for certain repetition rates.

DOI: 10.1103/PhysRevA.86.043423 PACS number(s): 32.80.Fb, 32.80.Ee, 32.80.Rm, 32.60.+i

I. INTRODUCTION

Exposure of atoms to short attosecond pulse trains phase-locked onto femtosecond pulses has recently given direct insight into electronic ground-state dynamics as the atom is perturbed by the femtosecond laser field [1,2]. The key ingredient which allows mapping between spectra of electron momenta and initial state dynamics is the very short and phase-locked attosecond burst as compared to the much slower original femtosecond laser pulse. A related experiment can be suggested based on highly excited atoms and on a much slower time scale: a train of femtosecond laser pulses firing on top of a microwave field which drives a Rydberg wave packet. The ionizing femtosecond pulse could in this case serve as a sensitive camera which could reconstruct the image of exotic electronic states on the border between classical physics and quantum dynamics.

The ionization of Rydberg atoms by femtosecond laser fields has been studied both experimentally and theoretically. For example, on the experimental side electron dynamics following two controlled time-delayed pulses has shown distinct electron emission characteristics [3,4]. On the theory side strong effects of counterpropagating pulses on Rydberg atom ionization probability have been predicted [5]. Recently, the ionization of low-lying circular Rydberg states exposed to circularly polarized laser fields was investigated both by solving the Schrödinger equation and by using the classical trajectory Monte Carlo (CTMC) method [6]. CTMC calculations have also been used extensively in exploring Rydberg atoms with very high principal quantum numbers, lately in the study of localized Bohr-like wave packets [7–9].

Several studies have investigated the dynamics of inter-n Rydberg wave packets in static electric fields through their ionization by half-cycle electric field pulses that ionize the wave packet during its motion [10,11]. More recently, the response of dynamic Rydberg wave packets created by a picosecond laser pulse from the Li($3d$) state in the presence of an inter-n mixing microwave field has been reported [12]. A strong modification of the selective field ionization (SFI) signal depending on the wave packet creation time with respect to the phase of the microwave field was detected.

Previous experimental works have considered wave packet dynamics and ionization where the Rydberg atom is exposed to strong n-mixing fields [10]. Here we consider theoretically the ionization signature of a related but different wave packet which can be created within a single n level when the atom is exposed to much weaker electric fields, below the Inglis-Teller limit, $1/3n^5$ (a.u.) [13]. The intra n-shell (angular) wave packet of hydrogen is driven by a microwave time-dependent electric field and exposed to a train of ionizing femtosecond laser pulses. The microwave field in our setup drives a wave packet of a given n-shell periodically between a maximum polarized (linear) Stark state and a circular state [14,15]. The ionization probability and electron emission characteristics are calculated as function of the number of laser pulses and the time separation between the pulses. The single-pulse ionization probability is found to be orders of magnitude larger for high Stark quantum numbers compared to the lower ones, and the angular emission spectra are shown to be detailed functions of the number of times the Rydberg wave packet is hit in highly polarized vs unpolarized states. Once the highly polarized states are hit they dominate the angular emission spectra completely.

In the following section we outline the theory and in the subsequent section results are discussed. Atomic units, where m_e, $\hbar$, and e are scaled to unity, are used throughout unless stated otherwise.

II. THEORY

Our starting point is a Rydberg wave packet driven in a Stark setup [16–18] by a resonant rotating microwave field,

$$\mathbf{E}_\mu(t) = \epsilon_0 \cos \omega_\mu t \hat{x} - \epsilon_0 \sin \omega_\mu t \hat{y} - \epsilon_z \hat{z}, \tag{1}$$

repeatedly between the circular ($|km\rangle = |0\ m_{\max}\rangle$) and the linear ($|km\rangle = |k_{\max}\ 0\rangle$) state in the Stark manifold, as shown in color in Fig. 2. k denotes the Stark quantum number. The field strength of the oscillating xy components is $\epsilon_0 = 10^{-8}$a.u., whereas the constant z component $\epsilon_z = 10^{-7}$a.u. induces a Stark energy splitting $\Delta E_z = 3/2n\epsilon_z = \omega_\mu = 2.4 \times 10^{-6}$a.u. When calculating matrix elements of the dipole operator within a principal n-shell the operator replacement $\hat{r} \rightarrow 3n/2\hat{a}$ [19] may be performed, where $\hat{a}$ is the operator for the Runge-Lenz vector. Since this operator behaves identically to a spin operator with each Stark state being eigenstates of $\hat{a}^2$ and $\hat{a}_z$, the selection rule $|\Delta k| = 1$ follows directly, as a parallel to

---

[*] sigrid.simonsen@ift.uib.no

[†] stian.sorngard@ift.uib.no

©2012 American Physical Society

the well-known selection rule $|\Delta m| = 1$ in the spherical basis. Due to the clockwise rotation of the resonant microwave field, one-photon absorption and emission solely allow transitions satisfying the selection rules $\Delta m = \pm 1$ and $\Delta k = \mp 1$. The wave packet will make one round trip along the Stark ladder in about ten revolutions of the microwave field.

We consider the situation where the wave packet slowly evolving in the microwave field is hit by a series of short femtosecond laser pulses. We assume that only a small fraction of the wave packet is launched to the continuum at each pulse; thus from first-order time-dependent perturbation theory the transition amplitude from the jth pulse in the pulse train reads

$$a_{qlm}^{(j)} = -i \int_{t_j}^{t_j+T} \langle \psi_{qlm} | V(t) | \Psi_b(t_j) \rangle e^{i(E_q - E_b)t} dt, \tag{2}$$

where q is the momentum of the ionized electron and T is the pulse duration of each pulse. The present Stark shift ΔE_z is of the order of 10^{-6}a.u., which is negligible compared to the binding energy of the $n = 16$ level without the Stark shift ($I_p \approx 0.002$ a.u.) when probing with an 800-nm pulse.

The bound electron wave function $\Psi_b(t)$ in Eq. (2) can be described as

$$|\Psi_b(t)\rangle = \sum_{k,m} c_{km}(t) |\psi_{nkm}\rangle, \tag{3}$$

where $|\psi_{nkm}\rangle$ denotes the Stark states. These can in turn be expanded in the spherical basis states $|\psi_{nlm}\rangle$ [20],

$$|\psi_{nkm}\rangle = \sum_l (-1)^l \left\langle \frac{n-1}{2}, \frac{m-k}{2}, \frac{n-1}{2}, \frac{m+k}{2} \middle| lm \right\rangle |\psi_{nlm}\rangle. \tag{4}$$

The amplitudes are Clebsch-Gordan coefficients, and we refer to them as b_{klm}. This gives the following expression for the bound state at time t:

$$|\Psi_b(t)\rangle = \sum_{k,m} \sum_l c_{km}(t)\, b_{klm}\, |\psi_{nlm}\rangle. \tag{5}$$

The coupling $V(t) = \mathbf{E}(t) \cdot \mathbf{r}$ in Eq. (2) is the laser-matter interaction within the dipole approximation when represented in the length gauge. Due to the short duration of the pulse ($\sim 10^2$ a.u.) compared to the time of evolution of the bound wave packet in the microwave field ($\sim 10^6$ a.u.), we neglect the effect of the microwave field during the action of the femtosecond probe pulse. In addition, due to the finite spectral width of the short ionizing pulse, excited (bound) states are populated throughout the interaction with the laser field, but the population in these states is nevertheless so small that it does not influence the subsequent ionization dynamics.

After interaction with a pulse train of N pulses separated by a time Δt, the continuum part of the total wave function of the system can be written as

$$|\Psi_c\rangle = \sum_{q,l,m} \sum_{j=1}^{N} a_{qlm}^{(j)} |\psi_{qlm}\rangle e^{-iE_q(N-j)\Delta t}, \tag{6}$$

giving the following amplitudes for the final continuum states,

$$\alpha_{qlm} = \sum_{j=1}^{N} a_{qlm}^{(j)} e^{-iE_q(N-j)\Delta t}. \tag{7}$$

Moreover, the continuum wave function is expanded in Coulomb partial waves $|\psi_{qlm}\rangle$, which conform to incoming boundary conditions,

$$\langle r | \psi_{qlm} \rangle = i^l e^{-i\sigma_l} Y_{lm}(\hat{r}) Y_{lm}^{*}(\hat{q}) R_{ql}(r), \tag{8}$$

where $\sigma_l = \arg \Gamma(l + 1 - i/q)$ is the Coulomb phase shift of the lth partial wave. The radial part, when normalized in momentum space, reads [21]

$$\begin{aligned} R_{ql}(r) \;=\; & \sqrt{\frac{2}{\pi}} \frac{e^{\pi/2q} |\Gamma(l + 1 - i/q)|}{(2l + 1)!} (2r)^l q^{l+1} e^{-iqr} \\ & \times {}_1F_1(l + 1 + i/q, 2l + 2, 2iqr). \end{aligned} \tag{9}$$

In the computations we have utilized the Coulomb wave implementation provided by the GNU Scientific Library (GSL) [22]. It should also be noted that the corresponding energy-normalized wave function is conveniently obtained through the scaling relation $R_{E_q l}(r) = q^{-1/2} R_{ql}(r)$.

To model the laser pulse we use a plane wave in the z direction modulated by a sine-square carrier envelope. The time-dependent electric field is derived from the vector potential

$$\mathbf{A}(t) = A_0 \sin^2 \left[\frac{\pi(t - t_j)}{T} \right] \sin[\omega(t - t_j)] \hat{z}, \tag{10}$$

through the relation $\mathbf{E}(t) = -\partial_t \mathbf{A}(t)$, where the central frequency ω of the plane wave corresponds to $\lambda = 800$ nm. The electric field strength is $E_0 = 2.0 \times 10^{-5}$ a.u. ($I_{\text{peak}} = 1.4 \times 10^7$ W cm^{-2}), and the duration of the pulse is given by $T = 2\pi N_{\text{oc}}/\omega$. In our calculations we have set the number of optical cycles $N_{\text{oc}} = 4$, which corresponds to a pulse duration of $T = 441$a.u. $= 11$fs.

With the amplitudes of the continuum wave packet at hand the differential probability is readlily obtained:

$$\frac{dP}{dq d\Omega} = \left| \sum_{l,m} \alpha_{qlm} \right|^2. \tag{11}$$

Integrating out the momentum gives the angular resolved ionization probability,

$$\frac{dP}{d\Omega}(\theta,\phi) = \int \left| \sum_{l,m} \alpha_{qlm} \right|^2 q^2 dq, \tag{12}$$

and alternatively, by performing the angular integral we obtain the energy spectrum,

$$\frac{dP}{dE_q} = \sum_{l,m} |\alpha_{qlm}|^2, \tag{13}$$

with $E_q = q^2/2$. For the sake of consistency, notice that in the latter formula the amplitudes α_{qlm} are energy normalized. Finally, the ionization probability is given by

$$P = \int \sum_{l,m} |\alpha_{qlm}|^2 q^2 dq. \tag{14}$$

In order to check the validity of the adopted first-order time-dependent perturbation theory approach, we compare in Fig. 1 the ionization probability so obtained with the exact

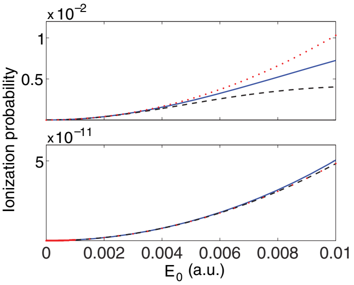

FIG. 1. (Color online) Ionization probability for a single pulse calculated using perturbation theory (red, dotted lines) and exact solution (blue, full lines) as a function of electric field strength E_0. A four-cycle laser pulse of the form given in Eq. (10) was used in the calculations. The initial states are $|nlm\rangle = |16\,0\,0\rangle$ (upper panel) and $|nlm\rangle = |16\;15\;15\rangle$ (lower panel). Also shown are the partial contributions of the $l = 1$ channel and the $l = 16$ channel (black, dashed lines) in the upper and lower panels, respectively. In the lower panel the three lines coincide.

one. The figure depicts the ionization probability for a single four-cycle pulse as a function of the electric field strength E_0 of the applied laser field. The upper and lower panels show the results for the initial states $|nlm\rangle = |16\;0\;0\rangle$ and $|nlm\rangle = |16\;15\;15\rangle$, respectively. Figure 1 also shows the partial contribution of the $l = 1$ channel (upper panel) and the $l = 16$ channel (lower panel) to the total ionization yield (red, dashed line), as obtained from the full calculation. The full calculations are performed using a spectral method where the eigenstates are expanded in either a Fourier series (in the case of the circular initial state) or a B-spline basis set (in the case of the 16s initial state), imposing a zero boundary condition at the edge of the radial box of some finite size $R_{\max}$. In the calculations $R_{\max}$ is varied in the interval 2400–5000 a.u. and the velocity gauge is assumed. Furthermore, angular momenta up to $l = 19$ are included in the basis set. As such, the results are checked for convergence with respect to both the number of angular momenta included and the size of the radial box. Figure 1 clearly indicates that the first-order time-dependent perturbation theory approach is valid up to electric field strengths of the order of 0.001 a.u., ensuring that the laser field applied in the present work ($E_0 = 2.0 \times 10^{-5}$a.u.) is well within the perturbative regime.

The ionization probabilities of Rydberg states are extremely small, and it is therefore important that the continuum is well represented, especially when calculating the angular-resolved ionization probability. Thus, we have conducted test calculations using different densities of states in the continuum discretization to make sure all quantities are converged.

Note finally that the widely used alternative perturbation theory based on Volkov waves completely fails in general when considering initial Rydberg states: Orders of magnitude discrepancies with exact calculations are obtained when replacing our final states with Volkov waves. The origin of the failure can be traced to the sensitivity of the initial state to electric fields. Other methods, like the sudden perturbation approximation [5,23], have been used on Rydberg atoms exposed to ultrashort laser pulses, but are not invoked here due to the good agreement between first-order perturbation theory and exact calculations.

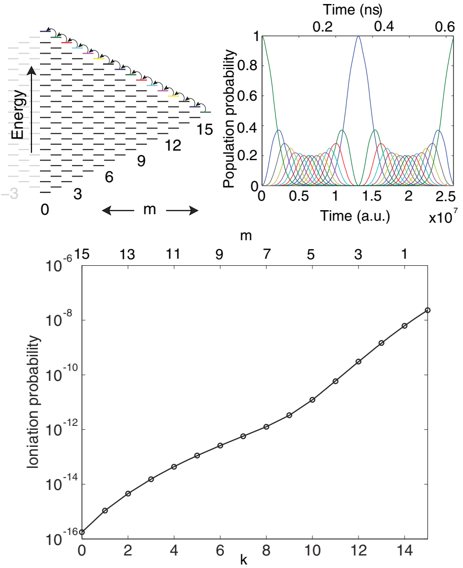

FIG. 2. (Color online) Upper left panel: Stark states $|km\rangle$ of the $n = 16$ level due to the constant electric field ϵ_z. Only the states with $m \geqslant 0$ are shown. The states populated by the rotating microwave field in the xy plane are shown in color and with arrows. Upper right panel: The population of the (colored) Stark states as a function of time for one round trip in the Stark setup, corresponding to time $\tau = 2.61 \times 10^7$ a.u. The initial state is the circular Stark state. After half the cycle τ the most polarized state is fully populated while the circular state is depleted. At the end of the round trip the circular state is totally revived. Lower panel: The ionization probability of the relevant Stark $|km\rangle$ states when fully populated. Field parameters are given in the text.

III. RESULTS

Before discussing the main findings it may be instructive to have a closer look at Fig. 2. The upper right panel shows the population probability for the states involved in one round trip in the Stark manifold (depicted in the left panel of the same figure). The period of this round trip is $\tau = 2.61 \times 10^7$ a.u. (0.63 ns), which again corresponds to about 10 times the period of the rotating microwave field in the xy plane. The wave function of the bound electron undergoes intrashell transitions, according to the selection rules $\Delta m = \pm 1$ and $\Delta k = \mp 1$, implying that only the “outermost” Stark states, i.e., the states

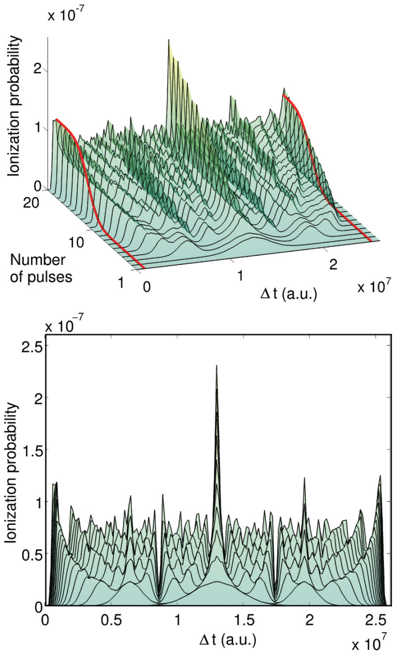

FIG. 3. (Color online) Ionization probability [cf. Eq. (14)] as a function of N succeeding pulses and time delay Δt. The initial state is the circular Stark state, $|nkm\rangle = |16\,0\,15\rangle$, and the maximum time separation $\tau = 2.61 \times 10^7$ a.u. corresponds to the revival time of the initial state in the microwave field. The lower panel shows the front view of the landscape plotted above. The minimum occurs at $\Delta t = 0$ and τ, but at time steps corresponding to $\tau/3$ and $2\tau/3$, there is only a small increase in the probability. The maximum is reached when pulses are separated by $\tau/2$, causing every second pulse to hit the most polarized Stark state. The thick red curves indicate the pulse sequences with $\Delta t = 9 \times 10^5$ a.u. and $\Delta t = 2.52 \times 10^5$ a.u. especially mentioned in Sec. III. Field parameters are given in the text.

with $m = n - k - 1$, are populated (cf. the upper left panel in Fig. 2).

The ionization probability of the Stark states in question, when fully populated, greatly varies in magnitude with increasing k, as the lower panel in Fig. 2 displays. The difference in ionization probability for the circular and linear states is of eight orders of magnitude, and this is related to the electron's ability to interact with the nucleus. The linear-most states are the states containing components of low angular momentum, which means that they are more likely to come close to the nucleus and hence are more likely to be slung out of the atom. The leap in the ionization probability is important for the understanding of what happens when the Stark manifold is hit by the pulse train and is referred to later in the discussion.

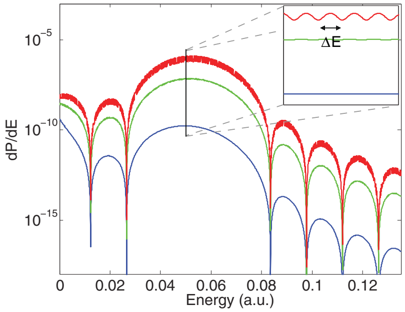

FIG. 4. (Color online) Energy distribution of the continuum wave packet for a series of pulses, $N = 3$ (lower, blue line), 4 (middle, green line), and 5 (upper, red line). The time separation between the pulses is $\Delta t = 3 \times 10^6$ a.u. Succeeding pulses hitting states with ionization probability differing only a few orders in magnitude cause interference in the continuum wave packet as observed between the fourth and the fifth pulse (upper line). The inset shows a closeup of the distributions on the interval $(0.05, 0.05 + 10^{-5})$ a.u. The period of the oscillations clearly matches the time delay between the pulses, i.e., $\Delta E = 2\pi/\Delta t \simeq 2.1 \times 10^{-6}$a.u. Field parameters are given in the text.

Figure 3 shows the total ionization probability [cf. Eq. (14)] of the Rydberg atom as a function of the number of femtosecond laser pulse shots N and the time delay Δt between the pulses. In each specific pulse train the pulses are equally separated in time. The initial state prior to the pulse train is the circular state $|nkm\rangle = |16\;0\;15\rangle$. In between the pulses in the pulse train the wave function of the bound electron undergoes intrashell transitions according to the scheme in Fig. 2, changing the state subject to ionization at each laser shot. The different pulse rates seem to yield approximately the same total ionization probability after the train of 20 pulses has passed, with the exception of six time separations Δt, for which the ionization probability is either strongly increased or totally suppressed. For $\Delta t \simeq 0$ and $\Delta t = \tau$ the pulse train hits the circular state at every impact, and thus the ionization probability remains at an absolute minimum at all times. The maximum is reached when $\Delta t = \tau/2$, causing every second pulse to hit the linear state, hence giving maximum contribution to the probability. A closer examination of the two valleys at $\Delta t = 8.7 \times 10^6$a.u. $= \tau/3$ and $\Delta t = 1.74 \times 10^7$a.u. $= 2\tau/3$ reveals that the ionization probability has a very small increase with N. This suggests, in light of the previous discussion, that for time separations corresponding to $\tau/3$ and $2\tau/3$ the laser pulses hit the wave packet only in states nearby, but not sufficiently close to, the linear state. It is interesting to notice that these are the only pulse rates, except for $\Delta t = 0$ and $\Delta t = \tau$, that seem to give such a behavior.

In addition, the total ionization probability depends on how many succeeding pulses are hitting the atom. As seen in the upper panel of Fig. 3 some time separations, like $\Delta t = 9 \times 10^5$ a.u. and $\Delta t = 2.52 \times 10^7$ a.u., yield a very slow increase

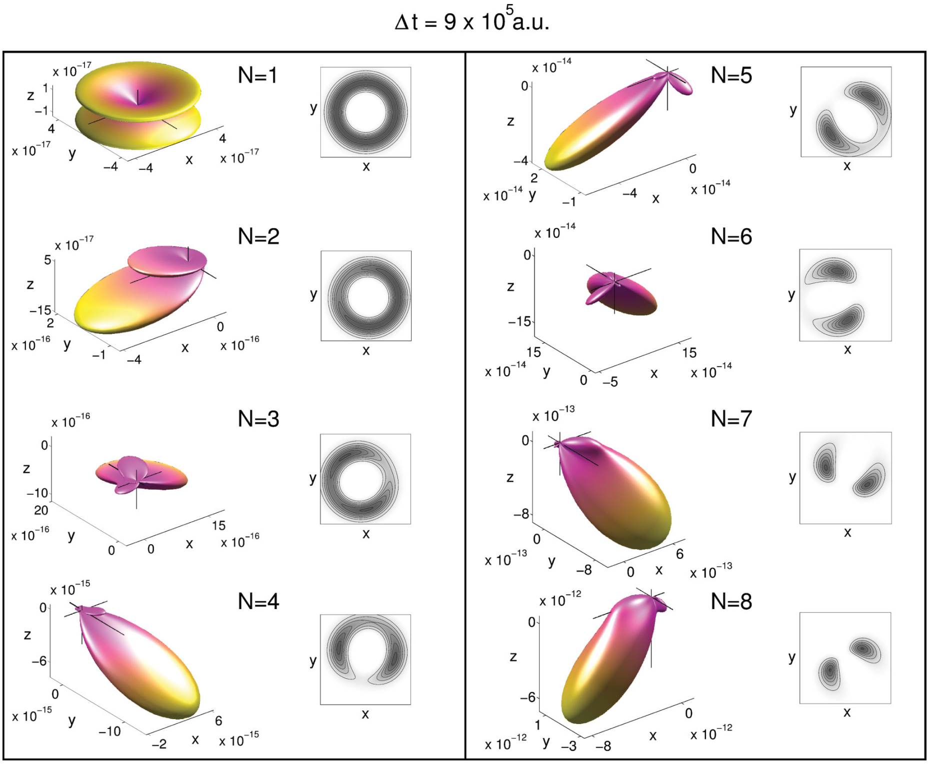

FIG. 5. (Color online) To the left in both panels are plotted the angular-resolved ionization probability $dP/d\Omega$ [c.f. Eq. (12)] for a series of N succeeding pulses with time separation $\Delta t = 9 \times 10^5$ a.u. To guide the eye we have included an auxiliary set of axes indicating the position of the origin. We observe that the distribution in the continuum rotates clockwise about the z axis with a period that is comparable to the period of the rotating microwave field. The right figures show cuts in the xy plane for the corresponding electron density distribution of the bound wave function from which the ionization happens. The initial state for the pulse train is the circular Stark state. Field parameters are given in the text.

in the ionization probability for the first 10 pulses, but a strong increase from 10 to 20 pulses. These two pulse sequences are shown as red (thick) curves in Fig. 3.

The energy spectrum, obtained by Eq. (13), of the total continuum wave packet after three, four, and five pulses are shown in Fig. 4, when the pulses are separated by $\Delta t = 3 \times 10^6$ a.u. As expected the distribution is dominated by the large one-photon resonance centered around the laser frequency $\omega = 0.057$ a.u. (800 nm). The side peaks in the spectrum can be attributed to the side bands of the sine-squared pulse envelope. More interestingly, one makes out some small oscillations superimposed on the energy spectrum of the fifth pulse, as can be seen in the inset of Fig. 4, where the energy distribution is plotted on a finer grid to obtain better resolution. These oscillations are caused by the interference between the wave packet launched to the continuum by the fifth pulse and the wave packet that is already there. We see that the period of the oscillations in question indeed corresponds to the time delay between the pulses, i.e., $\Delta E = 2\pi/\Delta t \simeq 2.1 \times 10^{-6}$ a.u. The interference effect is most pronounced when two succeeding wave packets are of comparable amplitudes, which is the case for the fourth and the fifth pulse (cf. upper panel of Fig. 3). One also notices that the relative height of the slow-electron peak close to the origin as compared to the one-photon resonance peak changes with number of pulses. These two peaks are the results of two different ionization processes. The first is the response to the electron cloud being pulled away from the nucleus, resulting in low-energy electrons being released from the core potential. The latter, dominating as the bound state gradually approaches the linear state, comes from the electron being "kicked out" when interacting with the nucleus, creating ionized electrons of higher energy.

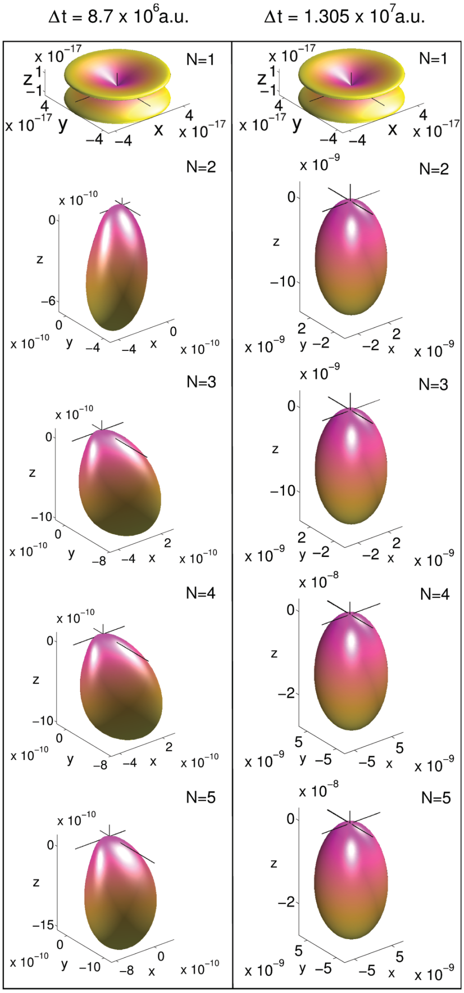

FIG. 6. (Color online) The figure shows the angular-resolved ionization probability $dP/d\Omega$ [cf. Eq. (12)] for five succeeding pulses. Starting in the circular Stark state the left column and the right column show the distribution when the time between the pulses is $\Delta t = 8.7 \times 10^6$ a.u and $\Delta t = 1.305 \times 10^7$a.u., respectively. To guide the eye we have included an auxiliary set of axes indicating the position of the origin. Field parameters are given in the text.

In Figs. 5 and 6 we consider the angular distribution of the ionized electron. In these figures we have plotted the angular-resolved ionization probability [cf. Eq. (12)] for a series of pulses of three different Δt. The first plot in all the three series corresponds to the initial state being the circular state. We see that the continuum wave packet for this state is symmetric about the z axis, as expected. To the left in both columns of Fig. 5 the evolution of the continuum from eight succeeding pulses with $\Delta t = 9 \times 10^5$ a.u. is shown. This is the time step causing the first peak in the plot of the total ionization probability (lower panel of Fig 3). The pulse repetition rate is so high that the bound wave packets do not have time to climb more than half the Stark ladder, and consequently the total ionization probability remains relatively low for the first eight pulses. It is interesting to observe that the main lobe of the angular distribution in this case seems to rotate clockwise about the z axis, and by careful examination of its period of rotation, it can be identified to match the period of the microwave field. This shows that femtosecond pulses firing on top of time-dependent radio frequency or microwave fields will, together with angular-resolved detection methods, serve as a direct camera of wave packet dynamics. To the right in the figure we have plotted a cut of the electron density distribution in the xy plane of the bound wave packet from which the ionization happens for each pulse N. The electron density rotates clockwise with the period of the rotating field, causing the rotation in the continuum distribution. Interestingly, it seems that the main lobe of the continuum distribution is turned a bit to the left from the least dense part of the bound wave packet for all pulses.

Starting with the right column of Fig. 6, we have plotted the angular distributions pertaining to the main ridge in Fig. 3. This is the special case in which the pulse train is tuned to strike the bound wave packet at times where it alternates between being at its most polarized and unpolarized, i.e., $\Delta t = \tau/2$. We observe that from the second pulse the distribution remains, for all practical means, unchanged throughout the pulse train. Taking into account that the first pulse hits the circular state, the next one hitting the linear state will completely overshadow the ionization from the first strike. The reason is evident when looking at Fig. 2, the linear Stark state, as compared to the circular Stark state, is by far more prone to be ionized.

Finally, we turn our attention to the left column of Fig. 6. The angular distributions in these plots correspond to the time step $\Delta t = \tau/3$ (cf. the first valley in Fig. 3). The difference in the repetition rate, as compared to the one in the right column, entails the femtosecond pulse hitting several states close to the linear one, and hence it introduces an asymmetry in the distributions. Comparing the two columns we see that though the distribution remains mostly along the negative z direction with increasing N for both cases, the ionization probability for $\Delta t = \tau/2$ is about an order of magnitude larger than that for $\Delta t = \tau/3$. It should also be mentioned that for increasing numbers of pulses, the ionization probability for $\Delta t = \tau/3$ will remain of the same order of magnitude as seen in Fig. 6, while for $\Delta t = \tau/2$ it will roughly be doubled for every other pulse.

IV. CONCLUSION

In this work we have studied features of single-electron ionization of a *dynamic* intra n-shell wave packet as compared to ionization from stationary states. Since the ionization probabilities of the stationary states vary largely with the degree of polarization (Stark quantum number), a strong sensitivity of the ionization probability to the repetition rate of the ionizing laser pulses occurs. In the most extreme cases the total ionization probability after a number of N pulses varies from almost zero to $N/2$ times the ionization probability of the maximum polarized Stark state. Moreover, the angular differential ionization probabilities are shown to be intimately related to the number of times the pulse train strikes the bound wave packet. The near-circular wave packets exhibit rotation in the xy plane due to the rotating microwave field, which is reflected in the continuum distribution. On the other hand, when the near-linear states are probed, the rotation in the continuum is completely overshadowed by the symmetric distribution of the highly polarized states in the z direction. Nevertheless, these findings suggest that more complex periodic dynamics of a Rydberg atom, for example, oscillations from classical to nonclassical states, may be monitored by weak ionizing femtosecond pulse trains.

ACKNOWLEDGMENTS

This project was supported by the Research Council of Norway (RCN) and the Bergen Research Foundation (Norway).

---

[1] J. Mauritsson, P. Johnsson, E. Mansten, M. Swoboda, T. Ruchon, A. L'Huillier, and K. J. Schafer, Phys. Rev. Lett. **100**, 073003 (2008).

[2] P. Johnsson, J. Mauritsson, T. Remetter, A. L'Huillier, and K. J. Schafer, Phys. Rev. Lett. **99**, 233001 (2007).

[3] M. L. Bajema, R. R. Jones, and T. F. Gallagher, Phys. Rev. A **70**, 062722 (2004).

[4] J. G. Story and H. N. Ereifej, Phys. Rev. Lett. **86**, 612 (2001).

[5] A. V. Lugovskoy and I. Bray, Phys. Rev. A **73**, 063401 (2006).

[6] S. Askeland, S. A. Sørngård, I. Pilskog, R. Nepstad, and M. Førre, Phys. Rev. A **84**, 033423 (2011).

[7] J. J. Mestayer, W. Zhao, J. C. Lancaster, F. B. Dunning, C. O. Reinhold, S. Yoshida, and J. Burgdörfer, Phys. Rev. Lett. **99**, 183003 (2007).

[8] J. J. Mestayer, B. Wyker, J. C. Lancaster, F. B. Dunning, C. O. Reinhold, S. Yoshida, and J. Burgdörfer, Phys. Rev. Lett. **100**, 243004 (2008).

[9] B. Wyker, S. Ye, F. B. Dunning, S. Yoshida, C. O. Reinhold, and J. Burgdörfer, Phys. Rev. Lett. **108**, 043001 (2012).

[10] C. Raman, T. C. Weinacht, and P. H. Bucksbaum, Phys. Rev. A **55**, R3995 (1997) .

[11] M. B. Campbell, T. J. Bensky, and R. R. Jones, Phys. Rev. A **59**, R4117 (1999).

[12] K. R. Overstreet, R. R. Jones, and T. F. Gallagher, Phys. Rev. A **85**, 055401 (2012).

[13] D. R. Inglis and E. Teller, Astrophys. J. **90**, 439 (1939).

[14] M. Førre, H. M. Nilsen, and J. P. Hansen, Phys. Rev. A **65**, 053409 (2002).

[15] L. Sælen, S. I. Simonsen, and J. P. Hansen, Phys. Rev. A **83**, 015401 (2011).

[16] R. G. Hulet and D. Kleppner, Phys. Rev. Lett. **51**, 1430 (1983).

[17] J. C. Day, T. Ehrenreich, S. B. Hansen, E. Horsdal-Pedersen, K. S. Mogensen, and K. Taulbjerg, Phys. Rev. Lett. **72**, 1612 (1994).

[18] R. Lutwak, J. Holley, P. P. Chang, S. Paine, D. Kleppner, and T. Ducas, Phys. Rev. A **56**, 1443 (1997).

[19] W. Pauli, Z. Phys. **36**, 336 (1926).

[20] T. F. Gallagher, *Rydberg Atoms* (Cambridge University Press, Cambridge, UK, 1994).

[21] H. A. Bethe and E. E. Salpeter, *Quantum mechanics of One- and Two-Electron Atoms* (Springer-Verlag, Berlin, 1957).

[22] The GNU Scientific Library, www.gnu.org/software/gsl.

[23] A. V. Lugovskoy and I. Bray, Phys. Rev. A **72**, 063402 (2005).

PAPER V

High-order harmonic generation from graphene: Strong attosecond pulses with arbitrary polarization

Stian Astad Sørngård, Sigrid Ina Simonsen and Jan Petter Hansen

Physical Review A, **87**, 053803 (2013)

PHYSICAL REVIEW A **87**, 053803 (2013)

High-order harmonic generation from graphene: Strong attosecond pulses with arbitrary polarization

Stian Astad Sørngård,[*] Sigrid Ina Simonsen,[†] and Jan Petter Hansen
Department of Physics and Technology, University of Bergen, N-5007 Bergen, Norway

(Received 23 November 2012; published 3 May 2013)

We explore high-order harmonic generation (HHG) from a graphene sheet exposed to intense femtosecond laser pulses based on the Lewenstein model. It is demonstrated that the HHG cutoff frequency increases with graphene size up to the classical limit for distant diatomic systems. In contrast to two-center systems, the cutoff frequency remains constant with increasing power of the harmonics as the graphene diameter extends beyond maximal electron excursion. It is shown that the extended nature of the graphene sheet allows for strong HHG signals at maximum cutoff for linearly as well as circularly polarized laser pulses, the latter opening for generation of strong circularly polarized attosecond pulses.

DOI: 10.1103/PhysRevA.87.053803 PACS number(s): 42.65.Ky, 33.20.Xx, 81.05.ue

High-order harmonic generation (HHG) refers to the nonlinear process of creation of very high overtones of an intense laser pulse with central frequency ω_0, which interacts with a dilute gas of atoms or molecules. The realization of laser intensities beyond 10^{14} W/cm^2 paved the way for theoretical studies [1,2] and experiments [3–5] on HHG from a gas of atoms in the early 1990s. Now, after about 20 years of intense HHG research, the three-step model [6] describing HHG within a single-atom picture is well established: The atom (i) ionizes, (ii) gains energy when accelerated by the electric field in the continuum, and (iii) eventually recombines with the ion emitting a photon at odd multiples of the driving-field frequency. Since a single excursion and recombination of an electron takes place within one-half optical cycle, the generated HHG photons define a coherent attosecond high-frequency laser pulse which is a unique tool for probing and imaging of ultrafast dynamics [7–9]. In laser-based imaging the HHG spectra have been used for tomographic reconstruction of molecular orbitals with ångström spatial resolution [10–12].

In recent years HHG following interaction with molecules has received particular attention. First, it has been shown that ionization at one molecular center and recombination at another allows for larger maximum harmonic frequencies [13,14]. Second, the two-center structure allows for the generation of attosecond pulses with elliptical polarization as well as even harmonics if the inversion symmetry is broken [15,16]. It has been shown theoretically that a preprepared molecular medium can be used to produce controlled secondary attosecond pulses, when exposed to a seed attosecond XUV pulse [17]. In addition, the study of HHG has been advancing towards molecules of increasing complexity such as benzene rings [18], fullerenes [19], and carbon nanotubes [20], including the investigation of symmetry properties essential for the selective generation of high-order harmonics.

The realization of graphene [21], a two-dimensional monolayer of carbon atoms, has received explosive interest in the last decade due to its extraordinary physical properties such as its superior strength and electronic conductivity. What was for years believed to be nothing but a theoretical toy model of a carbon allotrope is today considered to be a new paradigm in condensed-matter physics [22]. The ordered structure of the HOMO p_z-like orbitals of graphene makes it particularly interesting for HHG since the classical three-step model here allows for a large number of atomic pairs of sites for ionization and recombination for linearly as well as for circularly polarized driving laser pulses. This may generate strong attosecond pulses with tunable polarization, two features which are difficult to obtain when HHG originates from an unordered molecular gas.

Thus, in this paper we perform a numerical simulation of HHG from graphene within the strong-field approximation (SFA). We perform numerical calculations for one- and two-dimensional lattice structures and investigate the impact of the dimensionality on the harmonic power spectra. The calculations are carried out for laser light with various linear polarization angles with respect to the graphene sheet arranged in the xy plane and for a circularly polarized laser in the plane of the atomic sites. Atomic units, where m_e, $\hbar$, and e are scaled to unity are used throughout unless stated otherwise. The model system is illustrated in Fig. 1, which shows the HOMO p_z orbitals defining a honeycomb lattice (comprising hexagonal cells). A (red) laser pulse is schematically propagating through the graphene sheet and interacting with a number N of atomic graphene sites. As a result of this interaction, a possible trajectory of an electron ionized at one site and recombining at another site is highlighted.

The HHG power spectrum of photon frequencies ω_0 propagating in the $\mathbf{n}$ direction, when cast into the velocity form, reads

$$S_{\mathbf{n}}(\omega) = \left| \mathbf{n} \cdot \left(\int_{-\infty}^{\infty} dt [e^{i\omega t} \langle \Psi(t)|\mathbf{p}|\Psi(t)\rangle^{\mathrm{SFA}}] \right) \right|^2, \qquad (1)$$

where the superscript SFA denotes that the ionized wave function is calculated in the SFA [23,24]. This particular form of the power spectrum is the one that relates directly to the harmonic field from a solution of the Maxwell equations [25]. To describe the wave function we adopt a simple one-electron multicenter model of the bound (initial) state Ψ_b in graphene by a coherent sum of atomic orbitals distributed on a honeycomb

---

[*] stian.sorngard@ift.uib.no
[†] sigrid.simonsen@ift.uib.no

©2013 American Physical Society

lattice:

$$\Psi_{\mathrm{b}}(\mathbf{r},t) = \frac{1}{\sqrt{N}} \sum_{j}^{N} \psi(\mathbf{r}_j) e^{-i\varepsilon_0(t-t_0)}. \qquad (2)$$

Here ε_0 can be taken as the (negative) ionization potential of graphene, and Gaussian-type orbitals are employed to describe each site-specific wave function, $\psi(\mathbf{r}_j) = a_j r_{j_x}^{k_j} r_{j_y}^{l_j} r_{j_z}^{m_j} e^{-\alpha(\mathbf{r}-\mathbf{R}_j)^2}$. The results depend very weakly on the detailed shape of the site functions so we limit the present investigation to a single Gaussian-type p_z orbital on each site, i.e. $k_j = l_j = 0$, and $m_j = 1$, with $\alpha = 1$.

In a perturbative approach it is well known that the final state, as well as the results, is sensitive to the choice of gauge [24]. The length and velocity gauges, where the interaction terms are given by $\mathbf{E} \cdot \mathbf{r}$ and $\mathbf{A} \cdot \mathbf{p}$, respectively, are both widely used in the literature. For extended systems, we note here that the length gauge results in a nonphysical origin dependence of the spectra with no upper limit of the cutoff frequency as the maximum distance between two site atoms becomes increasingly large [26,27]. We therefore describe the ionization in the velocity gauge, which, in contrast, gives a cutoff behavior for two atoms with increasing internuclear distance $\mathbf{R}$, in agreement with exact calculations. The ionized electron states are then described by Volkov waves,

$$\Psi_{\mathrm{c}}(\mathbf{r},t) = \left(\frac{1}{2\pi}\right)^{3/2} e^{i\mathbf{k}\cdot\mathbf{r} - iS(k,t,t_0)}, \qquad (3)$$

where $S(k,t,t_0) = \frac{1}{2}\int_{t_0}^{t} dt'[\mathbf{k} + \mathbf{A}(t')]^2$ can be interpreted as the classical action of the field on the ejected electron. The expectation value of the momentum operator is readily expressed as

$$\langle \Psi(t)|\mathbf{p}|\Psi(t)\rangle^{\mathrm{SFA}} \approx -\mathrm{Re}\left\{\left(\frac{1}{2\pi}\right)^{3} \int_0^t dt' e^{i\varepsilon_0(t-t')} \int d^3k e^{-iS(k,t,t')} \left[\int d^3r e^{-i\mathbf{k}\cdot\mathbf{r}} \mathbf{A}(t')\cdot\mathbf{p}\Psi_{\mathrm{b}}(\mathbf{r})\right]\left[\int d^3r \Psi_{\mathrm{b}}^{*}(\mathbf{r}) \nabla e^{i\mathbf{k}\cdot\mathbf{r}}\right]\right\}, \qquad (4)$$

where Ψ is the total wave function. The first and the second expression enclosed by square brackets is the amplitude for ionization to the Volkov state $|\mathbf{k}\rangle$ at time t', and the amplitude for recombination at a later time t, respectively. The k integral is evaluated by the stationary phase method. Test calculations have also been performed to ensure that this method gives, in general, comparable results to exact integral calculations. The driving laser pulse is modeled by a six-cycle plane wave with central frequency $\omega_0 = 0.057$ a.u. ($\lambda = 800$ nm) and amplitude $E_0 = 0.114$ a.u. ($I_{\mathrm{peak}} = 4.6 \times 10^{14}$ W/cm^2) modulated by a trapezoidal envelope. In the following we discuss results originating from interaction with a linearly polarized field, where the polarization vector of the pulse is tiled at angle θ with respect to the z axis. Subsequently, the case of a circularly polarized field in the plane of the honeycomb lattice modeling graphene is presented.

In Fig. 2 we compare the cutoff of the harmonic spectrum for one- and two-dimensional structures interacting with a linearly polarized field with $\theta = 45^\circ$ as a function of their diameter in the x direction. The figure compares results for a diatomic system, a multiatomic string, and a graphene sheet. The results of Moreno *et al.* and Bandrauk *et al.* [14,28] implied a maximum cutoff law for diatomic systems, $N_{\max} = (I_p + 8U_p)/\omega_0$, where I_p is the ionization potential and U_p is the ponderomotive energy. The field parameters applied in our work give a maximum harmonic order of $N_{\max} = 149$, which is in fairly good agreement with the maxima in Fig. 2.

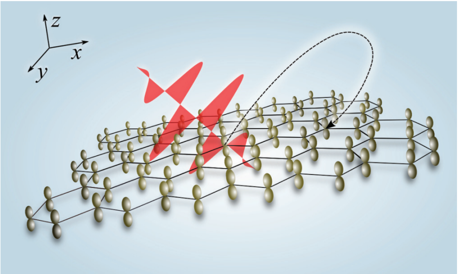

FIG. 1. (Color online) Artist's impression of graphene exposed to a linearly polarized laser pulse. The graphene layer is modeled by hydrogenic p_z orbitals distributed on a honeycomb lattice in the xy plane, and the polarization vector of the laser pulse is tilted with respect to the z axis. The trajectory illustrates the situation in which the ionized electron recombines with another atom in the lattice.

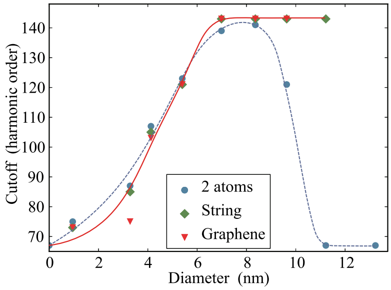

FIG. 2. (Color online) The harmonic spectrum cutoff as a function of the diameter of the focus area for a linearly polarized laser with polarization angle $\theta = 45^\circ$ for graphene [(red) triangles], a multiatom string along the x axis [(green) diamonds], and a two-atom string along the x axis [(blue) circles]. See the text for a more detailed description. Solid and dashed lines are plotted simply to guide the eye.

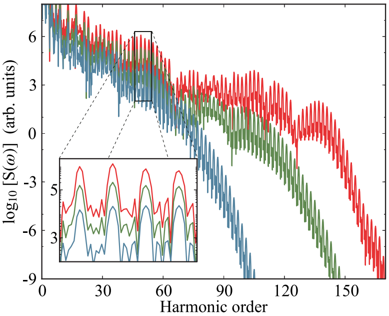

FIG. 3. (Color online) HHG power spectrum as a function of the harmonic order for a circular graphene sheet of 348 atoms [bottom (blue) line], 954 atoms [middle (green) line], and 2918 atoms [top (red) line] exposed to a linearly polarized laser. Inset: Closeup of the spectra. The polarization angle of the laser field is $\theta = 45^\circ$.

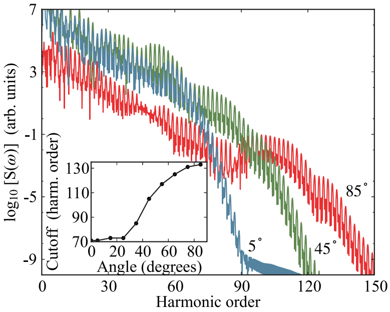

FIG. 4. (Color online) HHG power spectrum as a function of the harmonic order for a circularly shaped graphene layer composed of 552 atoms, with a diameter of 4.1 nm. The spectrum is plotted for three polarization angles of the linearly polarized field: 5° (blue line), 45° (green line), and 85° (red line). Inset: Cutoff as a function of the polarization angle.

Thus, atoms situated at the ideal interatomic distance in the x direction for classical ionization and recombination give rise to the same cutoff level for all three systems. For system diameters exceeding this ideal limit, the cutoff level for the diatomic system decreases until the spectrum is identical to the spectrum from two isolated atoms. In contrast, the cutoff frequency of the molecular string and the graphene sheet remain constant for increasing diameter. These systems support intermediate sites corresponding to optimal classical excursion.

In Fig. 3 we plot and compare the harmonic spectra from a graphene sheet with 348, 954, and 2918 atoms, which display the sensitivity of cutoff frequency on system size. The inset highlights the spectrum of odd harmonics around order ∼55. Most important is the observation that the intensity increases with the number of atoms. Thus, a stronger signal strength at cutoff is obtained from graphene sheets when the system size exposed to the laser pulse increases. In particular, this effect would yield a substantial enhancement of the signal power from an extended atomic structure compared to diatomic systems.

The sensitivity of the cutoff region to the polar angle θ between the z axis and the plane set up by the electric field deserves closer attention. In Fig. 4 we show harmonic power spectra for three choices of this angle for a fixed number of atoms. We observe an increasing cutoff with increasing angle. The dependence of the cutoff on the angle is depicted in the inset. Initially and up to 20° the dependence is very weak, which can be attributed to the dominant process of ionization and recollision at the same atom. At larger angles, a greater number of classical recombination sites opens up, and consequently the harmonic order grows. We note, however, that the stationary phase approximation breaks down at $\theta = 90^\circ$ for p_z orbitals. The apparently weaker harmonic spectrum at 85° is simply a result of this malfunction in the approximation, and it must be emphasized that exact calculations do not show such a deviation.

An important feature with our graphene model is the ability to generate strong high-order harmonics from circularly polarized laser pulses. To remain at a model level, here we replace p_z with s states and consider circularly xy polarized laser pulses propagating in the direction perpendicular to the graphene plane [29]. The upper panel in Fig. 5 displays the cutoff as a function of the number of atoms in the honeycomb lattice. A behavior of the cutoff and a strength similar to those for linearly polarized light are found (cf. Fig. 2). Again, the

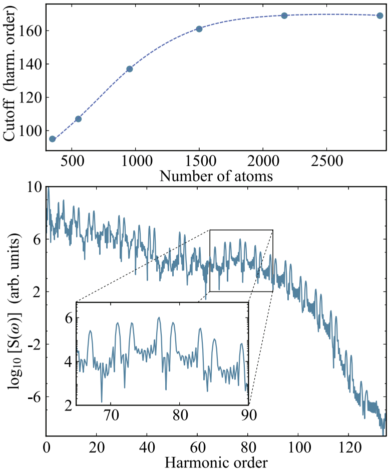

FIG. 5. (Color online) Top: Cutoff as a function of the number of atoms in a graphene sheet modeled by s orbitals exposed to a circularly polarized laser in the xy plane. Bottom: Power spectrum corresponding to 348 atoms. Inset: Closeup demonstrating the twin-peak power spectrum that characterizes the hexagonal lattice.

three-step model explains the phenomenon. For a dilute gas of molecules or atoms, the probability of recombining with the parent atom, or another atom, after an excursion in the continuum along a rotating electric field is almost 0. When the atoms are ordered in a regularly (infinite) flat molecule the recombination sites are of the same order as for the linearly polarized case. Thus, graphene as a target medium may be used to generate strong circularly polarized attosecond laser pulses.

The lower panel in Fig. 5 shows the power spectrum from 348 atoms arranged as graphene. This spectrum differs from the other spectra presented in that it exhibits a twin-peak structure. The twin peaks appear in accordance with the selection rule $6j \pm 1$ ($j = 0,1,\ldots$) first demonstrated by Alon *et al.* [30] and Baer *et al.* [18]. In these works the selection rules, for HHG spectra in general and for benzene rings aligned in the polarization plane of circular laser pulses in particular, are derived. Although the honeycomb grid structure is more involved, Fig. 5 clearly demonstrates that the selection rules in fact are those of a single hexagonal cell provided that the cells are symmetrically oriented with respect to the origin.

An experimental setup for testing the present findings will require a strong driving laser field to penetrate a large number of graphene sheets in order to produce strong high-order harmonic signals. This can be achieved in two ways: first, by using gas-phase graphene sheets kept aligned by a dynamic laser system coupled to the driving laser. Robust dynamical alignment of large gas-phase molecules has been demonstrated, e.g., in [31]. Alternatively, one can envision that a large number of graphene sheets can be stacked based on the rapidly evolving solution-phase technique with controlled stacking [32]. In both cases the HHG signal will become amplified similarly to that in HHG experiments with gas-phase atoms, with the additional benefit of higher photon frequencies and tunable polarization. A possible challenge will be to avoid heating and potentially damaging the graphene sheets, e.g., as demonstrated in [33]. We believe that shorter femtosecond pulse durations of only a few optical cycles may reduce this effect.

In summary, the present work has shown that graphene may generate more intense harmonic signals than gas-phase atoms or molecules and serve as a useful tool for selective harmonic generation when exposed to an intense driving laser field. This is established based on the Lewenstein model in combination with the simplest possible model representation of the HOMO state of graphene. Furthermore, the focal area spanned by a propagating circularly polarized laser pulse contains a large number of atoms available for recombination with ionized electrons. This mechanism generates strong HHG signals also from a circularly polarized driving laser, which may generate strong attosecond pulses with circular polarization.

The authors thank Morten Førre, Adam Etches, and Lars Boyer Madsen for thorough and illuminating discussions. This research was supported by the Research Council of Norway (RCN), the Bergen Research Foundation (Norway), and the Norwegian Metacenter for Computational Science (NOTUR).

---

[1] A. L'Huillier, K. J. Schafer, and K. C. Kulander, J. Phys. B **24**, 3315 (1991).

[2] J. L. Krause, K. J. Schafer, and K. C. Kulander, Phys. Rev. Lett. **68**, 3535 (1992).

[3] K. Miyazaki and H. Sakai, J. Phys. B **25**, L83 (1992).

[4] J. J. Macklin, J. D. Kmetec, and C. L. Gordon, Phys. Rev. Lett. **70**, 766 (1993).

[5] A. L'Huillier and P. Balcou, Phys. Rev. Lett. **70**, 774 (1993).

[6] P. B. Corkum, Phys. Rev. Lett. **71**, 1994 (1993).

[7] J. Itatani, J. Levesque, D. Zeidler, H. Niikura, H. Pepin, J. C. Kieffer, P. B. Corkum, and D. M. Villeneuve, Nature **432**, 867 (2004).

[8] A. Fohlisch, P. Feulner, F. Hennies, A. Fink, D. Menzel, D. Sanchez-Portal, P. M. Echenique, and W. Wurth, Nature **436**, 373 (2005).

[9] F. Krausz and M. Ivanov, Rev. Mod. Phys. **81**, 163 (2009).

[10] M. Lein, J. Phys. **40**, R135 (2007).

[11] S. Haessler, J. Caillat, W. Boutu, C. Giovanetti-Teixeira, T. Ruchon, T. Auguste, Z. Diveki, P. Breger, A. Maquet, B. Carre *et al.*, Nat. Phys. **6**, 200 (2010).

[12] E. V. van der Zwan and M. Lein, Phys. Rev. Lett. **108**, 043004 (2012).

[13] T. D. Donnelly, T. Ditmire, K. Neuman, M. D. Perry, and R. W. Falcone, Phys. Rev. Lett. **76**, 2472 (1996).

[14] A. D. Bandrauk, S. Chelkowski, H. Yu, and E. Constant, Phys. Rev. A **56**, R2537 (1997).

[15] C. B. Madsen and L. B. Madsen, Phys. Rev. A **74**, 023403 (2006).

[16] T. Kreibich, M. Lein, V. Engel, and E. K. U. Gross, Phys. Rev. Lett. **87**, 103901 (2001).

[17] M. Førre, E. Mével, and E. Constant, Phys. Rev. A **83**, 021402(R) (2011).

[18] R. Baer, D. Neuhauser, P. R. Ždánská, and N. Moiseyev, Phys. Rev. A **68**, 043406 (2003).

[19] G. P. Zhang, Phys. Rev. Lett. **95**, 047401 (2005).

[20] O. E. Alon, V. Averbukh, and N. Moiseyev, Phys. Rev. Lett. **85**, 5218 (2000).

[21] K. S. Novoselov, A. K. Geim, S. V. Morozov, D. Jiang, Y. Zhang, S. V. Dubonos, I. V. Grigorieva, and A. A. Firsov, Science **306**, 666 (2004).

[22] A. K. Geim and K. S. Novoselov, Nat. Mat. **6**, 183 (2007).

[23] L. V. Keldysh, Sov. Phys. JETP **20**, 1307 (1964).

[24] H. R. Reiss, Phys. Rev. A **22**, 1786 (1980).

[25] J. C. Baggesen and L. B. Madsen, J. Phys. B **44**, 115601 (2011).

[26] C. C. Chirilă and M. Lein, Phys. Rev. A **73**, 023410 (2006).

[27] J. Chen and S. G. Chen, Phys. Rev. A **75**, 041402(R) (2007).

[28] P. Moreno, L. Plaja, and L. Roso, J. Opt. Soc. Am. B **13**, 430 (1996).

[29] The Gaussian-type s and p_z orbitals representing the site functions in the graphene molecule are expected to yield qualitatively the same results. Within the stationary phase method the p_z orbital gives vanishing HHG spetra for circular polarized light in the xy plane.

[30] O. E. Alon, V. Averbukh, and N. Moiseyev, Phys. Rev. Lett. **80**, 3743 (1998).
[31] S. S. Viftrup, V. Kumarappan, S. Trippel, H. Stapelfeldt, E. Hamilton, and T. Seideman, Phys. Rev. Lett. **99**, 143602 (2007).
[32] K. Yu, P. Wang, G. Lu, K.-H. Chen, Z. Bo, and J. Chen, J. Phys. Chem. Lett. **2**, 537 (2011).
[33] A. Roberts, D. Cormode, C. Reynolds, T. Newhouse-Illige, B. J. LeRoy, and A. S. Sandhu, Appl. Phys. Lett. **99**, 051912 (2011).

APPENDIX A

ATOMIC UNITS

Throughout the thesis Hartree atomic units (a.u.) have been used unless stated otherwise. In this set of units the electronic mass, the elementary charge, the angular momentum and the electrostatic constant are all scaled to unity.

Table A.1: Fundamental and derived quantities in the Hartree atomic unit system

Quantity	Unit	Physical significance	Value in SI-units
Mass	m_e	Electron mass	$9.109\,38\ \times 10^{-31}$ kg
Charge	e	Absolute value of electron charge	$1.602\,18\ \times 10^{-19}$ C
Angular momentum	$\hbar = \frac{h}{2\pi}$	Planck's constant divided by 2π	$1.054\,57 \times 10^{-34}$ Js
Electrostatic constant	$4\pi\varepsilon_0$	4π times the permittivity of free space	$1.112\,65 \times 10^{-10}$ Fm^{-1}
Length	$a_0 = \frac{\hbar}{m_e c\alpha}$	Bohr radius of atomic hydrogen	$5.291\,77\ \times 10^{-11}$ m
Velocity	$v_0 = \alpha c$	Magnitude of electron velocity in first Bohr orbit	$2.187\,69 \times 10^{6}$ ms^{-1}
Time	$\tau_0 = \frac{a_0}{v_0}$	Time required for electron in first Bohr orbit to travel one Bohr radius	$2.418\,88\ \times 10^{-17}$ s
Energy	$E_h = \alpha^2 m_e c^2$	Twice the binding energy of atomic hydrogen	$4.35975 \times 10^{-18}\,\mathrm{J} = 27.2114\,\mathrm{eV}$
Frequency	$f = \frac{v_0}{2\pi a_0}$	Angular frequency of electron in first Bohr orbit divided by 2π	$6.579\,69\ \times 10^{15}$ s^{-1}
Electric field strength	$F_0 = \frac{e}{(4\pi\varepsilon_0)a_0^2}$	Strength of the Coulomb field experienced by an electron in the first Bohr orbit of atomic hydrogen	$5.142\,21\ \times 10^{11}$ Vm^{-1}

Hartree atomic units should not be confused with Rydberg atomic units, which are based on a slightly different scaling assumption $4\pi\varepsilon_0 = 1$, $m_e = 1/2$, $\hbar = 1$ and $e = 1/\sqrt{2}$. Consequently the unit of energy in the two systems differs by a factor of two, i.e., $E_{\mathrm{H}} = 2E_{\mathrm{Ry}}$.

APPENDIX B

THE VELOCITY GAUGE MATRIX ELEMENTS

The matrix elements of a field along the *x*- and *y*-axis

In what follows we derive the dipole matrix elements as implemented in Pyprop. In the velocity gauge formulation the Hamiltonian of the laser-matter interaction, when using the reduced wavefunction $u(r) = r\psi(r)$, reads,

$$H = -\mathrm{i}\mathbf{A}(t) \cdot \left(\nabla - \frac{\mathbf{r}}{r^2} \right), \tag{B.1}$$

with the x- and y-components,

$$H_x = -\mathrm{i}A_x(t) \left(\frac{\partial}{\partial x} - \frac{\sin\theta\cos\phi}{r} \right) \tag{B.2}$$

and

$$H_y = -\mathrm{i}A_y(t) \left(\frac{\partial}{\partial y} - \frac{\sin\theta\sin\phi}{r} \right), \tag{B.3}$$

where

$$\frac{\partial}{\partial x} = \cos\phi\sin\theta\frac{\partial}{\partial r} - \frac{\sin\phi}{r\sin\theta}\frac{\partial}{\partial\phi} + \frac{\cos\phi\cos\theta}{r}\frac{\partial}{\partial\theta} \tag{B.4}$$

and

$$\frac{\partial}{\partial y} = \sin\phi\sin\theta\frac{\partial}{\partial r} + \frac{\cos\phi}{r\sin\theta}\frac{\partial}{\partial\phi} + \frac{\sin\phi\cos\theta}{r}\frac{\partial}{\partial\theta}. \tag{B.5}$$

Some additional formulas are needed in the derivation. The first one is the definition of the spherical harmonics

$$Y_{lm}(\theta,\phi) = (-1)^{\frac{1}{2}(m+|m|)} \left[\frac{2l+1}{4\pi} \frac{(l-|m|)!}{(l+|m|)!} \right]^{1/2} P_l^{|m|}(\cos\theta)\mathrm{e}^{im\phi}. \tag{B.6}$$

The second is its partial derivative with respect to the polar angle

$$\frac{\partial}{\partial\theta}Y_{lm}(\theta,\phi) = |m|\cot\theta Y_{lm}(\theta,\phi) + \delta_m A_{l,m} e^{-\mathrm{i}\delta_m\phi} Y_{l,m+\delta_m}(\theta,\phi), \tag{B.7}$$

where

$$\delta_m = \begin{cases} 1, & m \geq 0 \\ -1, & m < 0 \end{cases}, \tag{B.8}$$

and

$$A_{l,m} = [(l - |m|)(l + |m| + 1)]^{1/2}. \tag{B.9}$$

When utilizing the Hamiltonian of Eq. (B.2) the matrix elements becomes

$$\begin{aligned}
\langle Y_{l'm'}|H_x|Y_{lm}\rangle = {} & \frac{\partial}{\partial r}\iint Y^*_{l'm'}(\theta,\phi)\cos\phi\sin\theta Y_{lm}(\theta,\phi)\mathrm{d}\Omega \\
& - \frac{1}{r}\iint Y^*_{l'm'}(\theta,\phi)\frac{\sin\phi}{\sin\theta}\frac{\partial}{\partial\phi}Y_{lm}(\theta,\phi)\mathrm{d}\Omega \\
& + \frac{1}{r}\iint Y^*_{l'm'}(\theta,\phi)\cos\phi\cos\theta\frac{\partial}{\partial\theta}Y_{lm}(\theta,\phi)\mathrm{d}\Omega \\
& - \frac{1}{r}\iint Y^*_{l'm'}(\theta,\phi)\sin\theta\cos\phi Y_{lm}(\theta,\phi)\mathrm{d}\Omega \\
\equiv {} & \frac{\partial}{\partial r}\mathcal{I}_1(l',m',l,m) - \frac{1}{r}\mathcal{I}_2(l',m',l,m) + \frac{1}{r}\mathcal{I}_3(l',m',l,m) - \frac{1}{r}\mathcal{I}_1(l',m',l,m),
\end{aligned} \tag{B.10}$$

where $\mathrm{d}\Omega = \sin\theta\mathrm{d}\theta\mathrm{d}\phi$. The three integrals in Eq. (B.10) can all be solved analytically following along the lines of [84] though applied to a different problem. The first one, is straight forward,

$$\begin{aligned}
\mathcal{I}_1(l',m',l,m) = {} & \iint Y^*_{l'm'}(\theta,\phi)\sin\theta\cos\phi Y_{lm}(\theta,\phi)\mathrm{d}\Omega \\
= {} & \frac{1}{2}\iint Y^*_{l'm'}(\theta,\phi)\sin\theta\mathrm{e}^{\mathrm{i}\phi}Y_{lm}(\theta,\phi)\mathrm{d}\Omega \\
& + \frac{1}{2}\iint Y^*_{l'm'}(\theta,\phi)\sin\theta\mathrm{e}^{-\mathrm{i}\phi}Y_{lm}(\theta,\phi)\mathrm{d}\Omega.
\end{aligned} \tag{B.11}$$

The expression may be reformulated using the spherical harmonics

$$Y_{1,\pm1} = \mp\left(\frac{3}{8\pi}\right)^{1/2}\sin\theta\mathrm{e}^{\pm\mathrm{i}\phi}, \tag{B.12}$$

yielding

$$\begin{aligned}
\mathcal{I}_1(l',m',l,m) = {} & -\frac{1}{2}\left(\frac{8\pi}{3}\right)^{1/2}\iint Y^*_{l'm'}(\theta,\phi)Y_{1,1}(\theta,\phi)Y_{lm}(\theta,\phi)\mathrm{d}\Omega \\
& + \frac{1}{2}\left(\frac{8\pi}{3}\right)^{1/2}\iint Y^*_{l'm'}(\theta,\phi)Y_{1,-1}(\theta,\phi)Y_{lm}(\theta,\phi)\mathrm{d}\Omega.
\end{aligned} \tag{B.13}$$

The integrals comprising three spherical harmonics are conveniently expressed in terms of Clebsch-Gordan coefficients [21],

$$\mathcal{I}_1(l',m',l,m) = \left(\frac{1}{2}\frac{2l+1}{2l'+1}\right)^{1/2}\langle l100|l'0\rangle\left[\langle l1m(-1)|l'm'\rangle - \langle l1m1|l'm'\rangle\right]. \tag{B.14}$$

The second integral is solved in a similar manner,

$$\begin{aligned}\mathcal{I}_2(l',m',l,m) &= \iint Y^*_{l'm'}(\theta,\phi)\frac{\sin\phi}{\sin\theta}\frac{\partial}{\partial\phi}Y_{lm}(\theta,\phi)\mathrm{d}\Omega \\ &= \frac{1}{2\mathrm{i}}\int_0^{2\pi}\int_0^{\pi}Y^*_{l'm'}(\theta,\phi)e^{\mathrm{i}\phi}\frac{\partial}{\partial\phi}Y_{lm}(\theta,\phi)\mathrm{d}\theta\mathrm{d}\phi \\ &\quad -\frac{1}{2\mathrm{i}}\int_0^{2\pi}\int_0^{\pi}Y^*_{l'm'}(\theta,\phi)e^{-\mathrm{i}\phi}\frac{\partial}{\partial\phi}Y_{lm}(\theta,\phi)\mathrm{d}\theta\mathrm{d}\phi.\end{aligned} \tag{B.15}$$

The spherical harmonics are related to the associated Legendre polynomials via Eq. (B.6), which upon substitution in Eq. (B.15) yields,

$$\begin{aligned}\mathcal{I}_2(l',m',l,m) = &\frac{m\nu^{m'}_{l'}\nu^m_l}{2}\int_0^{\pi}P^{|m'|}_{l'}(\cos\theta)P^{|m|}_l(\cos\theta)\mathrm{d}\theta\int_0^{2\pi}e^{\mathrm{i}(m-m'+1)\phi}\mathrm{d}\phi \\ -&\frac{m\nu^{m'}_{l'}\nu^m_l}{2}\int_0^{\pi}P^{|m'|}_{l'}(\cos\theta)P^{|m|}_l(\cos\theta)\mathrm{d}\theta\int_0^{2\pi}e^{\mathrm{i}(m-m'-1)\phi}\mathrm{d}\phi,\end{aligned} \tag{B.16}$$

where a abbreviation is introduced,

$$\nu^m_l = (-1)^{\frac{1}{2}(m+|m|)}\left[\frac{2l+1}{4\pi}\frac{(l-|m|)!}{(l+|m|)!}\right]^{1/2}. \tag{B.17}$$

After the integral in the azimuthal coordinate is evaluated in addition to a coordinate transformation in the polar angle, one arrives at,

$$\mathcal{I}_2(l',m',l,m) = \pi m\nu^{m'}_{l'}\nu^m_l(\delta_{m'-1,m}-\delta_{m'+1,m})\int_{-1}^{1}\frac{P^{|m'|}_{l'}(x)P^{|m|}_l(x)}{\sqrt{1-x^2}}\mathrm{d}x. \tag{B.18}$$

The integral over the product of Legendre polynomials

$$\mathcal{K}_1(l,m,p,q) \equiv \int_{-1}^{1}\frac{P^m_l(x)P^q_p(x)}{\sqrt{1-x^2}}\mathrm{d}x \tag{B.19}$$

is to be computed for $m = q\pm 1$. As the associated Legendre polynomial $P^m_l(x)$ is odd when $l-m$ is odd and even otherwise, and since the denominator of Eq. (B.19) is an even function, the integral turns out to be zero by symmetry when $\Delta_{lmpq} \equiv (l-m)+(p-q)$ is odd. This corresponds to one odd and one even associated Legendre polynomial. Given $q-m=\pm 1$, it is required that $p-l = 2j+1$ for Δ_{lmpq} to be even and the integral to be nonzero. In this special case the integral has the solutions

$$\int_{-1}^{1}\frac{P^{\mu}_{\nu}(x)P^{\mu+1}_{\nu+2j+1}(x)}{\sqrt{1-x^2}}\mathrm{d}x = \begin{cases} 0, & j<0 \\ \frac{2(\nu+\mu)!}{(\nu-\mu)!}, & j\geq 0 \end{cases}. \tag{B.20}$$

As for the last integral it can be rewritten using Eq. B.7,

$$\begin{aligned}
\mathcal{I}_3(l',m',l,m) &= \iint Y^*_{l'm'}(\theta,\phi)\cos\phi\cos\theta\frac{\partial}{\partial\theta}Y_{lm}(\theta,\phi)\mathrm{d}\Omega \\
&= \iint Y^*_{l'm'}(\theta,\phi)\cos\phi\cos\theta|m|\cot\theta Y_{lm}(\theta,\phi)\mathrm{d}\Omega \\
&\quad - \delta_m A_{l,m}\iint Y^*_{l'm'}(\theta,\phi)\cos\phi\cos\theta\mathrm{e}^{-\mathrm{i}\delta_m\phi}Y_{l,m+\delta_m}(\theta,\phi)\mathrm{d}\Omega \\
&= |m|\int_0^{2\pi}\int_0^{\pi} Y^*_{l'm'}(\theta,\phi)\cos\phi\cos^2\theta Y_{lm}(\theta,\phi)\mathrm{d}\theta\mathrm{d}\phi \\
&\quad - \delta_m A_{l,m}\int_0^{2\pi}\int_0^{\pi} Y^*_{l'm'}(\theta,\phi)\cos\phi\cos\theta\mathrm{e}^{-\mathrm{i}\delta_m\phi}Y_{l,m+\delta_m}(\theta,\phi)\sin\theta\mathrm{d}\theta\mathrm{d}\phi \\
&\equiv |m|\mathfrak{J}_1(l',m',l,m) - \delta_m A_{l,m}\mathfrak{J}_2(l',m',l,m)
\end{aligned} \tag{B.21}$$

The full derivations of the subintegrals $\mathfrak{J}_1$ and $\mathfrak{J}_2$ are found in [84]. Here, we only present the result. The first one is,

$$\begin{aligned}
\mathfrak{J}_1(l',m',l,m) &= \int_0^{2\pi}\int_0^{\pi} Y^*_{l'm'}(\theta,\phi)\cos\phi\cos^2\theta Y_{lm}(\theta,\phi)\mathrm{d}\theta\mathrm{d}\phi \\
&= \ldots \\
&= \pi(\delta_{m'-1,m}+\delta_{m'+1,m})\nu^{m'}_{l'}\big[\nu^m_{l-2}F_{l,m}\mathcal{K}_1(l',|m'|,l-2,|m|) \\
&\quad + \nu^m_l(G_{l,m}+H_{l,m})\mathcal{K}_1(l',|m'|,l,|m|) + \nu^m_{l+2}I_{l,m}\mathcal{K}_1(l',|m'|,l+2,|m|)\big],
\end{aligned} \tag{B.22}$$

where

$$\begin{aligned}
F_{l,m} &= \left[\frac{(l+m)(l-m)(l+m-1)(l-m-1)}{(2l+1)(2l-1)^2(2l-3)}\right]^{1/2} \\
G_{l,m} &= \left[\frac{(l+m)(l-m)}{(2l+1)(2l-1)}\right] \\
H_{l,m} &= \left[\frac{(l+m+1)(l-m+1)}{(2l+1)(2l+3)}\right] \\
I_{l,m} &= \left[\frac{(l+m+1)(l-m+1)(l+m+2)(l-m+2)}{(2l+1)(2l+3)^2(2l+5)}\right]^{1/2}.
\end{aligned} \tag{B.23}$$

The second is,

$$\begin{aligned}
\mathfrak{J}_2(l',m',l,m) &= \iint Y^*_{l'm'}(\theta,\phi)\cos\phi\cos\theta e^{-\mathrm{i}\delta_m\phi}Y_{l,m+\delta_m}(\theta,\phi)\mathrm{d}\Omega \\
&= \ldots \\
&= \pi\nu^{m'}_{l'}(\delta_{m'-1,m}+\delta_{m'+1,m})\big[\nu^{m+\delta_m}_{l-1}J_{l,m}\mathcal{K}_2(l-1,|m+\delta_m|,l',|m'|) \\
&\quad + \nu^{m+\delta_m}_{l+1}K_{l,m}\mathcal{K}_2(l+1,|m+\delta_m|,l',|m'|)\big],
\end{aligned} \tag{B.24}$$

where

$$\mathcal{K}_2(l,m,p,q) = \int_{-1}^{1} P_l^{|m|}(x) P_p^{|q|}(x) \mathrm{d}x \tag{B.25}$$

and

$$\begin{aligned} J_{l,m} &= \left[\frac{(l+m+\delta_m)(l-m-\delta_m)}{(2l+1)(2l-1)}\right]^{1/2} \\ K_{l,m} &= \left[\frac{(l+m+\delta_m+1)(l-m-\delta_m+1)}{(2l+1)(2l+3)}\right]^{1/2}. \end{aligned} \tag{B.26}$$

The solution of the integral in Eq. (B.25) is obtained through a series of gammafunctions,

$$\mathcal{K}_2(l,m,p,q) = \\ \begin{cases} \sum_{i=0}^{\lfloor (l-m)/2 \rfloor} \sum_{j=0}^{\lfloor (p-q)/2 \rfloor} C_{l,m}^{i} C_{p,q}^{j} \frac{\Gamma\left(\frac{l+p-m-q-2i-2j+1}{2}\right)\Gamma\left(\frac{m+q+2i+2j+2}{2}\right)}{\Gamma\left(\frac{l+p+3}{2}\right)}, & l+p-m-q \text{ is even} \\ 0, & l+p-m-q \text{ is odd} \end{cases} \tag{B.27}$$

and

$$C_{\alpha,\beta}^{\gamma} = \frac{(-1)^{\gamma}(\alpha+\beta)!}{2^{\beta+2\gamma}(\beta+\gamma)!\gamma!(\alpha-\beta-2\gamma)!}. \tag{B.28}$$

Regarding the matrix element of the y-direction, it bears close resemblance to that of the x-direction with only minor differences. The total matrix element reads,

$$\langle Y_{l'm'}|H_y|Y_{lm}\rangle = \frac{\partial}{\partial r}\mathcal{I}_1(l',m',l,m) + \frac{1}{r}\mathcal{I}_2(l',m',l,m) + \frac{1}{r}\mathcal{I}_3(l',m',l,m) - \frac{1}{r}\mathcal{I}_1(l',m',l,m) \tag{B.29}$$

where

$$\mathcal{I}_1(l',m',l,m) = \mathrm{i}\left(\frac{1}{2}\frac{2l+1}{2l'+1}\right)^{1/2} \langle l100|l'0\rangle [\langle l1m1|l'm'\rangle + \langle l1m(-1)|l'm'\rangle], \tag{B.30}$$

$$\mathcal{I}_2(l',m',l,m) = \mathrm{i}\pi m \nu_{l'}^{m'} \nu_l^m (\delta_{m'-1,m} + \delta_{m'+1,m}) \mathcal{K}_1(l',|m'|,l,|m|) \tag{B.31}$$

and

$$\mathcal{I}_3(l',m',l,m) = |m|\mathcal{J}_1(l',m',l,m) - \delta_m E_{l,m}\mathcal{J}_2(l',m',l,m), \tag{B.32}$$

with

$$\begin{aligned} \mathcal{J}_1(l',m',l,m) = \mathrm{i}\pi(\delta_{m'+1,m} - \delta_{m'-1,m})\nu_{l'}^{m'} \big[&\nu_{l-2}^{m} F_{l,m}\mathcal{K}_1(l',|m'|,l-2,|m|) \\ &+ \nu_l^m (G_{l,m}+H_{l,m})\mathcal{K}_1(l',|m'|,l,|m|) + \nu_{l+2}^{m} I_{l,m}\mathcal{K}_1(l',|m'|,l+2,|m|)\big] \end{aligned} \tag{B.33}$$

and

$$\begin{aligned} \mathcal{J}_2(l',m',l,m) = \mathrm{i}\pi\nu_{l'}^{m'}(\delta_{m'+1,m} - \delta_{m'-1,m})\big[&\nu_{l-1}^{m+\delta_m} J_{l,m}\mathcal{K}_2(l-1,|m+\delta_m|,l',|m'|) \\ &+ \nu_{l+1}^{m+\delta_m} K_{l,m}\mathcal{K}_2(l+1,|m+\delta_m|,l',|m'|)\big]. \end{aligned} \tag{B.34}$$

BIBLIOGRAPHY

[1] M. Planck, Ann. Phys. **4**, 553 (1901). 1

[2] A. Einstein, Ann. Phys. **322**, 132–148 (1905). 1

[3] H. Hertz, Ann. Phys. **267**, 983 (1887). 1

[4] N. Bohr, Philos. Mag. **26**, 1 (1913). 1

[5] N. Bohr, Philos. Mag. **26**, 476 (1913). 1

[6] N. Bohr, Philos. Mag. **26**, 857 (1913). 1

[7] W. Heisenberg, Z. Phys. **33**, 879 (1925). 1

[8] M. Born and P. Jordan, Z. Phys. **34**, 858 (1925). 1

[9] E. Schrödinger, Ann. Phys. **79**, 361; 489 (1926). 1

[10] E. Schrödinger, Ann. Phys. **80**, 437 (1926). 1

[11] E. Schrödinger, Ann. Phys. **81**, 109 (1926). 1

[12] W. Heisenberg, Z. Phys **43**, 172 (1927). 1

[13] N. Bohr, Z. Phys. **2**, 423 (1920). 1, 4.1.4

[14] J. Gribbin, *In Search of Schrödinger's Cat: Quantum Physics and Reality* (Bantam Books, New York, 1984). 1

[15] R. Feynman, *The Character of Physical Law* (The MIT Press, Cambridge, Massachusetts, 1965). 1

[16] R. G. Gould, in *The Ann Arbor Conference on Optical Pumping*, edited by P. A. Franken and R. H. Sands (1959), p. 128. 2

[17] A. Einstein, Deutsche Physikalische Gesellschaft **18**, 318 (1916). 1

[18] T. H. Maiman, Nature **187**, 493 (1960). 1

[19] F. H. M. Faisal, *Lectures on Ultrafast Intense Laser Science 1* (Springer-Verlag, Berlin, 2010). 1

[20] M. Göppert, Naturwissenschaften **17**, 932 (1929). 1

[21] B. H. Bransden and C. J. Joachain, *Physics of Atoms and Molecules* (Pearson Education, Harlow, 2003). 1, 2.2.3, B

[22] F. W. Byron and C. J. Joachain, Phys. Rev. **164**, 1 (1967). 1

[23] M. A. Kornberg and P. Lambropoulos, J. Phys. B **32**, L603 (1999). 1

[24] J. Colgan and M. S. Pindzola, Phys. Rev. Lett. **88**, 173002 (2002). 1

[25] L. Feng and H. W. van der Hart, J. Phys. B **36**, L1 (2003). 1

[26] S. Laulan and H. Bachau, Phys. Rev. A **68**, 013409 (2003). 1

[27] D. A. Horner, F. Morales, T. N. Rescigno, F. Martín, and C. W. McCurdy, Phys. Rev. A **76**, 030701 (2007). 1

[28] J. Feist, S. Nagele, R. Pazourek, E. Persson, B. I. Schneider, L. A. Collins, and J. Burgdörfer, Phys. Rev. A **77**, 043420 (2008). 1, 4.2

[29] E. Foumouo, P. Antoine, B. Piraux, L. Malegat, H. Bachau, and R. Shakeshaft, J. Phys. B **41**, 051001 (2008). 1

[30] X. Guan, K. Bartschat, and B. I. Schneider, Phys. Rev. A **77**, 043421 (2008). 1

[31] M. Førre, S. Selstø, and R. Nepstad, Phys. Rev. Lett. **105**, 163001 (2010). 1

[32] R. Nepstad, T. Birkeland, and M. Førre, Phys. Rev. A **81**, 063402 (2010). 1, 4.1.3

[33] J. Colgan, M. S. Pindzola, and F. Robicheaux, J. Phys. B **41**, 121002 (2008). 1, 4.7

[34] F. Morales, F. Martín, D. A. Horner, T. N. Rescigno, and C. W. McCurdy, J. Phys. B **42**, 134013 (2009). 1, 4.7

[35] X. Guan, K. Bartschat, and B. I. Schneider, Phys. Rev. A **82**, 041404 (2010). 1

[36] X. Guan, K. Bartschat, and B. I. Schneider, Phys. Rev. A **84**, 033403 (2011). 1, 4.7

[37] G. W. F. Drake, ed., *Springer Handbooks of Atomic, Molecular, and Optical Physics* (Springer Science+Business Media, New York, 2006). 1

[38] L. V. Keldysh, J. Exp. Theor. Phys. **47**, 1945 (1964). 1

[39] F. H. M. Faisal, J. Phys. B **6**, L89 (1973). 1

[40] H. R. Reiss, Phys. Rev. A **22**, 1786 (1980). 1

[41] G. H. C. New and J. F. Ward, Phys. Rev. Lett. **19**, 556 (1967). 1

[42] A. McPherson, G. Gibson, H. Jara, U. Johann, T. S. Luk, I. A. McIntyre, K. Boyer, and C. K. Rhodes, J. Opt. Soc. Am. B **4**, 595 (1987). 1

[43] M. Ferray, A. L'Huillier, X. F. Li, L. A. Lompre, G. Mainfray, and C. Manus, J. Phys **21**, L31 (1988). 1

[44] G. Farkas and C. Tóth, Phys. Lett. A **168**, 447 (1992). 1

[45] S. Harris, J. Macklin, and T. Hänsch, Opt. Commun. **100**, 487 (1993). 1

[46] P. M. Paul, E. S. Toma, P. Breger, G. Mullot, F. Augé, P. Balcou, H. G. Muller, and P. Agostini, Science **292**, 1689 (2001). 1

[47] M. V. Fedorov and A. M. Movsesian, J. Phys. B. **21**, L155 (1988). 1

[48] M. Pont, N. R. Walet, M. Gavrila, and C. W. McCurdy, Phys. Rev. Lett. **61**, 939 (1988). 1

[49] M. Pont and M. Gavrila, Phys. Rev. Lett. **65**, 2362 (1990). 1, 1

[50] Q. Su, J. H. Eberly, and J. Javanainen, Phys. Rev. Lett. **64**, 862 (1990). 1

[51] K. Burnett, P. L. Knight, B. R. M. Piraux, and V. C. Reed, Phys. Rev. Lett. **66**, 301 (1991). 1

[52] K. C. Kulander, K. J. Schafer, and J. L. Krause, Phys. Rev. Lett. **66**, 2601 (1991). 1

[53] J. H. Eberly and K. C. Kulander, Science **262**, 1229 (1993). 1

[54] S. Geltman, J. Phys. B. **27**, 257 (1994). 1

[55] M. P. de Boer, J. H. Hoogenraad, R. B. Vrijen, L. D. Noordam, and H. G. Muller, Phys. Rev. Lett. **71**, 3263 (1993). 1

[56] J. H. Hoogenraad, R. B. Vrijen, and L. D. Noordam, Phys. Rev. A **50**, 4133 (1994). 1

[57] N. J. van Druten, R. C. Constantinescu, J. M. Schins, H. Nieuwenhuize, and H. G. Muller, Phys. Rev. A **55**, 622 (1997). 1

[58] H. A. Kramers, *Collected Scientific Papers* (North-Holland, Amsterdam, 1956). 2.1

[59] W. C. Henneberger, Phys. Rev. Lett. **21**, 838 (1968). 2.1

[60] L. B. Madsen, Phys. Rev. A **65**, 053417 (2002). 2.1

[61] H. A. Bethe and E. E. Salpeter, *Quantum mechanics of one- and two-electron atoms* (Springer-verlag, Berlin, 1957). 2.2.1

[62] W. Pauli, Z. Phys **36**, 336 (1926). 2.2.2

[63] A. K. Kazansky and V. N. Ostrovsky, J. Phys. B **29**, L855 (1996). 2.2.2

[64] T. F. Gallagher, *Rydberg atoms* (Cambridge University Press, Cambridge, 1994). 2.2.2

[65] P. B. Corkum, Phys. Rev. Lett. **71**, 1994 (1993). 3.2.1, 3.2.2

[66] P. Moreno, L. Plaja, and L. Roso, J. Opt. Soc. Am. B **13**, 430 (1996). 3.2.2

[67] C. C. Chirilă and M. Lein, Phys. Rev. A **73**, 023410 (2006). 3.2.3

[68] J. Chen and S. G. Chen, Phys. Rev. A **75**, 041402 (2007). 3.2.3

[69] K. S. Novoselov, A. K. Geim, S. V. Morozov, D. Jiang, Y. Zhang, S. V. Dubonos, I. V. Grigorieva, and A. A. Firsov, Science **306**, 666 (2004). 3.3.1

[70] I. S. Gradshteyn and I. M. Ryzhik, *Table of Integrals, Series, and Products* (Academic Press, Burlington, 2007), 7th ed. 3.3.1

[71] M. Lewenstein, P. Balcou, M. Y. Ivanov, A. L'Huillier, and P. B. Corkum, Phys. Rev. A **49**, 2117 (1994). 3.3.2

[72] M. Gavrila, J. Phys. B **35**, R147 (2002). 4.1.1, 4.1.5

[73] T. Birkeland, Ph.D. thesis, University of Bergen (2009). 4.1.3

[74] H. Bachau, E. Cormier, P. Decleva, J. E. Hansen, and F. Martín, Reports on Progress in Physics **64**, 1815 (2001). 4.1.3

[75] R. Grobe and C. K. Law, Phys. Rev. A **44**, R4114 (1991). 4.1.4

[76] J. Grochmalicki, M. Lewenstein, and K. Rzążewski, Phys. Rev. Lett. **66**, 1038 (1991). 4.1.4

[77] X. M. Tong and C. D. Lin, J. Phy. B **38**, 2593 (2005). 4.1.5

[78] M. Gavrila and J. Z. Kamiński, Phys. Rev. Lett. **52**, 613 (1984). 4.1.5

[79] M. Gavrila, *Atoms in Intense Laser Fields* (Academic, New York, 1992). 4.1.5

[80] M. Gavrila, I. Simbotin, and M. Stroe, Phys. Rev. A **78**, 033404 (2008). 4.1.5

[81] M. Førre, S. Selstø, J. P. Hansen, and L. B. Madsen, Phys. Rev. Lett. **95**, 043601 (2005). 4.1.5

[82] T.-G. Lee, M. S. Pindzola, and F. Robicheaux, J. Phys. B **43**, 165601 (2010). 4.2

[83] F. Martín, J. Fernández, T. Havermeier, L. Foucar, T. Weber, K. Kreidi, M. Schöffler, L. Schmidt, T. Jahnke, O. Jagutzki, et al., Science **315**, 629 (2007). 6

[84] T. Khan and A. Thomas, Tech. Rep. TR-2004-12-KT, Department of Mathematical Sciences, Clemson University, Clemson (2004). B, B